TWINNING AND MORPHOLOGY OF III-V NANOWIRES

Een wetenschappelijke proeve op het gebied van de
Natuurwetenschappen, Wiskunde en Informatica

Proefschrift

ter verkrijging van de graad van doctor
aan de Radboud Universiteit Nijmegen,
op gezag van de rector magnificus
prof. mr. S.C.J.J. Kortmann,
volgens besluit van het College van Decanen
in het openbaar te verdedigen
op 17 november 2010
om 15:30 uur precies

door

Rienk Ewoud Algra

geboren op 5 maart 1981
te Amsterdam.

Dit proefschrift is goedgekeurd door de promotors:
Prof. dr. E. Vlieg
Prof. dr. E.P.A.M. Bakkers (Technische Universiteit Delft)

en co-promotors:
Dr. W.J.P. van Enckevort
Dr. M.A. Verheijen (Philips Research Eindhoven)

Manuscriptcommissie:
Prof. dr. S.E. Speller
Prof. dr. P.M. Koenraad (Eindhoven University of Technology)
Dr. M.T. Borgström (Lund University, Lund, Sweden)

This research was carried out under project number MC3.05243 in the framework of the Strategic Research Program of the Materials innovation institute (M2i) in the Netherlands (www.M2i.nl).

Cover image: Image of dew on a grass-field resembling the nanowires and the importance of the liquid droplet during nanowire growth (front cover). Nano-imprinted arrays of nanowires depicting the logo's of the three collaborating groups (back cover)

Cover design by: Rienk Algra

Printed by: Ridderprint BV

ISBN: 978-90-77172-62-9

Contents

Chapter 1

Introduction

1.1 Nanowires

Nanotechnology refers to the understanding and controlling of materials on the nano (10^{-9} m) scale. According to Moore's law every two years the number of transistors that can be placed on an integrated circuit doubles. To accomplish this the features constantly need to be scaled down in size. There are two main routes which can be followed in order to fabricate nano-structures. First there is the '*top-down*' approach, where standard lithography and etching techniques are used to fabricate nanometer sized structures. This technique is widely used in the Si-technology. On the other hand, structures which are initiated by growth are created via the so called '*bottom-up*' approach. In 1964 Wagner and Ellis first discovered the bottom-up Vapor-Liquid-Solid (VLS) growth mechanism [1], which resulted in Si whiskers with a diameter on the micrometer scale. Nowadays, this growth mechanism is the most commonly used to synthesize wires with nanometer scale diameters, *i.e.* nanowires.

Nanowires are a beautiful example of nanotechnology, with dimensions of ∼5-100 nm in diameter and up to several microns in length. They have a large aspect ratio of 1000 or more and therefore nanowires are referred to as 1-D structures. Due to the dimensions of the nanowires interesting properties are found that are not seen in bulk (3-D) materials. An example is quantum confinement, where optical properties are different compared to bulk structures. In addition, nanowire materials have been grown with sometimes different crystal structures, and other properties, than found in the bulk. Importantly, the scale of the wires implies that the effect of the surface is very important. The large surface to bulk ratio makes the nanowires very sensitive to charges surrounding the wire surface, thereby affecting the opto-electrical properties. This high sensitivity may be useful in sensor applications, but can have a negative effect on nanowire devices. It is

important to note that nanowires do not address CMOS (Complementary Metal-Organic-Semiconductor) scaling, but may add functionality.
The success of the semiconductor industry is based on bandgap engineering. By tuning the chemical composition spatially, the electronic properties of a layer stack are fine tuned. However, lattice matching requirements limit the possibilities of combining materials with different crystal lattice parameters. Nanowires show an unprecedented ability to combine different semiconductor materials due to their small dimensions. Different materials can be stacked in the length (axial) direction as well as in the radial direction and even different classes of materials can be combined.
These interesting properties make nanowires attractive building blocks in future devices. They have a large potential in new electronic devices [2, 3], like sensors [4] and quantum devices [5]. LED's [6] and lasers [7] are examples of optical devices. Moreover in the field of energy nanowires could be used for photovoltaics [8] or thermo/piezo-electrics.
In the following paragraphs the VLS growth mechanism of nanowires will be explained. First, the role of the metal particle is discussed. Next, the phase diagrams are discussed, which determine the particle composition followed by the interaction of the metal particle with the substrate, which leads to epitaxial growth. The different growth techniques that can be used for nanowire growth are discussed next and a more detailed description is given for the growth technique used in this thesis. Subsequently, the different nanowire materials are introduced with several examples from literature. After that the growth kinetics are discussed which play a role during VLS growth. This leads to a variety of nanowire designs such as hetero structures, doping profiles and twin structures, which opens the route to complex device fabrication. Finally, as an introduction to the scope of this thesis three important aspects, namely the crystal structure, morphology and defects, will be discussed in more detail.

1.2 VLS growth

Semiconducting nanowires can be grown by the VLS growth mechanism. All nanowires discussed in this thesis are grown by using this method. As the name 'Vapor-Liquid-Solid' suggests, three phases are involved in nanowire growth. As shown in figure 1.1, upon heating the metal particles on the substrate form an alloy with the substrate material and specific (group III) precursors from the gas phase. This turns the seed particle from solid into liquid, following the binary phase diagrams of the different materials systems. Subsequently, by continu-

ous supply of precursor material from the gas phase, the particle saturates and eventually reaches supersaturation. If the supersaturation is sufficient, crystal nucleation starts at the droplet-substrate interface. The wire grows layer by layer, lifting the catalyst particle. During growth there is a dynamic equilibrium between materials supply from the gas phase, transport through the droplet, and crystal growth at the droplet- nanowire crystal interface. With this mechanism group IV, III-V and II-VI semiconductors have been synthesized.

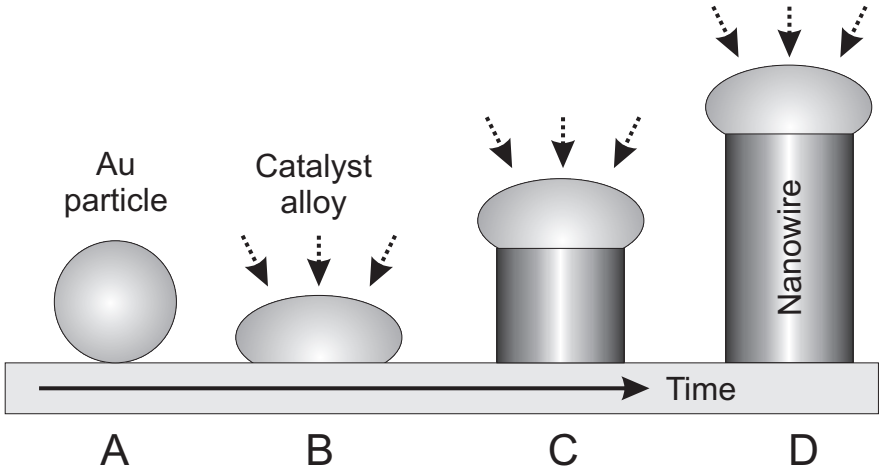

Figure 1.1: Different stages in the VLS growth process. In **(A)** metal particles are deposited on the substrate. By heating the metal particle forms an alloy **(B)** with the substrate and gas phase. When the particle is supersaturated, growth of the wire starts as shown in **(C)**, where the wire diameter is determined by the size of the particle. By continued supply of precursor material from the gas phase the nanowire evolves, with the particle remaining on top of the wire, shown in **(D)**.

1.3 Role of the metal particle

Typical for the VLS growth mechanism is the metal particle on top from which the wire grows. The metal particle acts a catalyst. The precursors from the gas phase are effectively decomposed at the surface of the metal particle [9] at relatively low temperatures. This results in a lowering of the activation energy and thus nanowire growth below the normal bulk growth temperatures can take place. Other aspects related to the growth of nanowires can be attributed to the metal particle, and will be discussed here. First the position and diameter control will be discussed, followed by the influence of the metal particle on growth related aspects such as diffusion, supersaturation and composition. As will be shown in detail in chapter 4, the particle dynamics affect also the formation of

twin planes. Finally the particle composition, especially at the growth interface, can influence the nucleation probabilities and thereby affect the crystal structure of the nanowire, as will be shown in chapter 2.

Size and position: The position of the metal particle dictates where nanowire growth will take place, since the wires grow by the VLS mechanism. On the other hand, the size of the particle determines the diameter of the wire. Here, the initial size of the particle is important as well as the alloy composition during growth, which affects the volume, and thus the diameter, of the particle [10]. For the fabrication of future devices both parameters are essential. The metal particle can be deposited in several ways on the substrate. First of all, a thin film of metal, up to several nm in thickness, can be deposited on the substrate [11]. By annealing the substrate before growth the thin layer will break up in differently sized spheres at random positions on the surface. As shown in figure 1.2a this results in a large variety of nanowire diameters. In order to control the diameter of the wires colloids are used. These are metal particles of a specific diameter suspended in an aqueous solution. Via spin-coating [12] the colloids are homogeneously distributed over the substrate surface in a random fashion (see figure 1.2b). Similar to colloids, aerosol particles can be used, which also have a specific diameter. These are deposited on the substrate from the gas phase [13]. To achieve position and diameter control of the nanowires, which are necessary in future device fabrication, e-beam lithography [9, 14–16] or Substrate Conformal Imprint Lithography (SCIL) [17, 18] can be used, as shown in figure 1.2c. With e-beam lithography a pre-defined pattern can be 'written' in a polymethylmethacrylate (PMMA) layer. This step is followed by deposition of a thin metal layer and a lift-off process to remove the organic material together with the excess metal. This method results in a pattern of metal dots on a substrate. The SCIL method makes use of the same metal deposition and lift-off process, however a flexible patterned stamp made from ploy-di-methylsiloxane (PDMS) is used to define a pattern in the PMMA. The flexible stamp is molded from a silicon master stamp, which is prepared by e-beam lithography. A great advantage of SCIL is that similar feature sizes as for e-beam lithography can be patterned at a fraction of the cost because the stamp can be reused numerous times. The SCIL process is described in detail in chapter 7.

Diffusion and supersaturation: During nanowire growth volume and surface diffusion lengths, diffusion rates and supersaturation are important parameters which affect the growth process. The diffusion length of the growth units determines how much material is available for growth. This affects the supersatura-

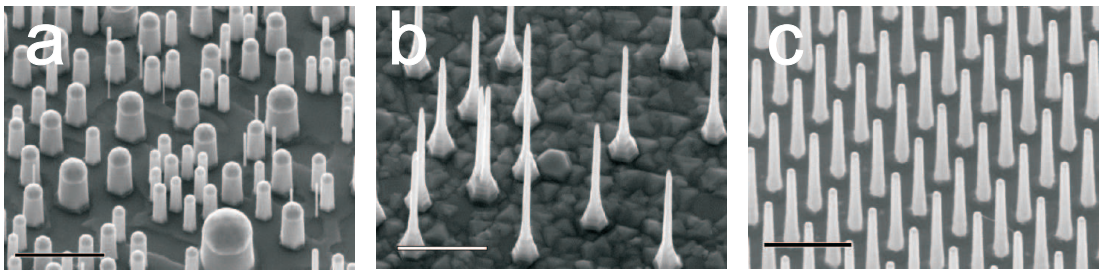

Figure 1.2: Nanowires grown from different metal deposition methods. (a) Growth via thin film **(b)** growth via colloids **(c)** growth via Substrate Conformal Imprint Lithography (SCIL). All scale bars represent 1 μm.

tion, which is given by the difference in thermodynamic potential per molecule between, for example, the gas phase and the liquid phase. The diffusion rate determines how fast the material is transported though a specific phase. Due to the small size of the metal particles they have a relatively large surface to volume ratio. At these conditions the Gibbs-Thomson effect starts to play a role, which implies that the droplet curvature increases the effective pressure in the metal particle. This could lead to changes in the solidification temperatures of the metal particle. The diffusion rates of the growth units inside the metal particle are affected by the phase of the particle, that can be either liquid or solid. In turn the growth rates are affected by the diffusion rate. The supersaturation in the particle is determined by the pressure as well as the alloy composition in the particle. This complex interplay between diffusion, supersaturation and surface kinetics makes the determination of the actual supersaturation at the solid-liquid interface a highly difficult task.

Another effect that plays a crucial role on the supersaturation is the density of nanowires on the substrate, making the situation even more complex. As shown in figure 1.3 the distance between nanowires determines whether competitive growth, synergetic growth or independent growth takes place [19]. The parameters which determine the different growth regimes are the diffusion lengths over the surface (λ_s) and through the gas phase (λ_g). If both regimes overlap, competitive growth of the available growth units occurs between nanowires. If, on the other hand, there is no overlap in the diffusion regimes, independent growth takes places. In between these growth regimes, synergetic growth takes place. The diffusion length through the gas phase is larger compared to the surface diffusion. Therefore, at a certain distance between the nanowires only interaction via the gas phase is possible (synergetic regime). Only material that is decomposed at the metal particle contributes to the gas diffusion. Since the metal particle acts

as a catalyst, it effectively decomposes the group III precursors. As a result larger particles decompose more material and contribute more to diffusion through the gas phase, affecting locally the supersaturations. This results, as shown in figure 1.3, in higher growth rates in areas where more catalyst material is present (synergetic effect).

Dynamics: The metal particle being in liquid or solid phase has a significant effect on the growth. The droplet dynamics such as the droplet contact angles and surface tensions are different compared to a static solid particle. As will be discussed in chapters 4 and 5 in detail, the contact angle of the droplet with respect to the growth interface plays a crucial role in the formation of twin planes and their position along the nanowires resulting in random, paired or superlattice twins.

Composition: The metal particle can consist of various materials. The most commonly used material is Au [1, 20–22], since Au is inert to the reactions which take place on the substrate surface. Furthermore, the Au alloys with the precursors from the gas phase and acts as a local sink for growth units, thereby providing a supersaturation in the metal particle. Besides Au, also materials like Ni [23], Al [24] and Cu [25] are reported to result in nanowire growth. The different materials of the metal particle as well as the different precursors used during growth result in many alloy compositions. Each alloy has its own specific phase diagram and consequently different compositions and eutectic temperatures. This is the temperature at which a specific compound composition solidifies, which typically occurs at temperatures well below the solidification temperature of the pure compounds. As a result, the conditions for growth can be different for the material systems. At the growth interface of a liquid droplet (solid-liquid interface) the composition of the alloy is particularly important. As will be shown in chapter 6 the composition of the alloy can affect the nucleation probabilities at the growth interface of the nanowire. The atoms are distributed in an ordered fashion at the interface and thereby favor the growth of a specific crystal structure.

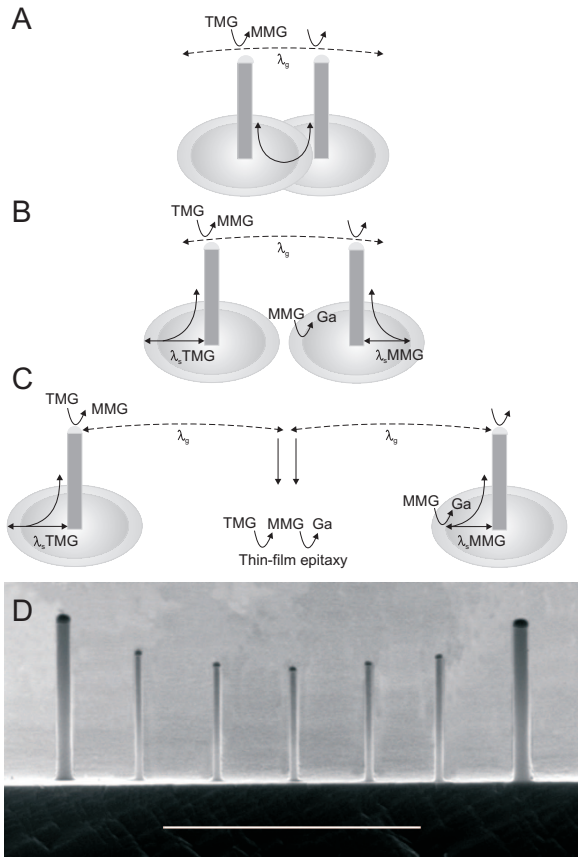

Figure 1.3: Diffusion regimes [19] **(A)** competitive growth **(B)** synergetic growth and **(C)** independent growth regimes. The group V material, trimehylgallium (TMG), is decomposed in monomethylgallium (MMG) at the catalyst particle, feeding the gas diffusion or at the substrate surface, feeding the surface diffusion. Depending on the distance between the nanowires the diffusion on the surface and gas phase either overlap (competitive growth), are completely separated (independent growth) or the surface diffusion is separated and the gas diffusion regimes still overlap (synergetic growth). In **(D)** synergetic growth is shown. The decomposition of precursors scales with the droplet area, proving a higher supersaturation. For larger nanowire diameters effectively more catalyst material is available, compared to thinner wires. This locally results in an increase in the supersaturation, and therefore increased growth rates. The thin wires close to the larger diameter wires benefit from the locally increased supersaturation due to the diffusion through the gas phase. This results in an increased length for thin wires close to the larger diameters compared to thin wires that stand further away. The scale bar represents 1 μm.

1.4 Phase diagrams

Phase diagrams show the different compositions at which alloys are formed, depending on temperature, pressure and various atomic ratios. The phase diagram

gives relevant information about the solidification temperatures of the particle as well as the stable compositions. The difference between VLS and VSS (Vapor Solid Solid) growth can be distinguished in this way. Furthermore, the composition of the alloy affects the supersaturation, and thus the nanowire growth kinetics. For these reasons it is essential to know the properties of the different alloys. A wide variety of binary phase diagrams can be found in literature [26] giving some degree of knowledge about the alloy composition. As an example binary phase diagrams are shown for Au-In and Au-P in figure 1.4. These graphs indicate where one could expect the metal particle to be solid or liquid. Furthermore, the phase diagrams indicate whether stable alloy compositions, such as the ϕ phase in Au-In, can be formed or whether complete phase separation occurs, as shown for Au-P. However, data are almost exclusively available for two component systems. In most growth systems three or even more types of atoms are present in the alloy particle. Therefore ternary phase diagrams are needed, which are available only to some extent. As a result, the exact composition during growth remains unclear in most cases.

1.5 VLS, VSS & Catalyst free growth

Depending on the growth temperature the nanowire growth mechanism can either be VLS or VSS [27–29]. The eutectic temperature for the catalyst (alloy) particle is given by the relevant phase diagram, as discussed in the previous paragraph. This results in a liquid or solid phase of the particle. Nanowire growth is mainly reported in the VLS mode [20, 30], since generally the growth temperatures are above the eutectic temperatures of the materials. On the other hand, below the eutectic point the VSS mode is observed, for example, for Ge [29] and III-V compounds [31]. Interestingly, the VLS mode is also observed below the eutectic temperature of the known binary phase diagrams. The VSS growth mode should occur at these temperatures, however growth rates similar to VLS growth can be found. These growth rates are roughly one order of magnitude larger than values found for the VSS growth mode. The question is why VLS growth can still occur at temperatures where the alloy is supposed to be solid. To exactly understand this phenomenon the ternary phase diagrams are needed, which give the exact eutectic temperatures and distinguish between VLS and VSS. In addition, there are several other possible explanations for VLS growth below the eutectic temperature. The small dimensions, and therefore relatively high pressures inside the catalyst particle, the Gibbs Thomson effect, can lead to a lowering of the eutectic temperature. Furthermore, undercooling is a well known phenomenon

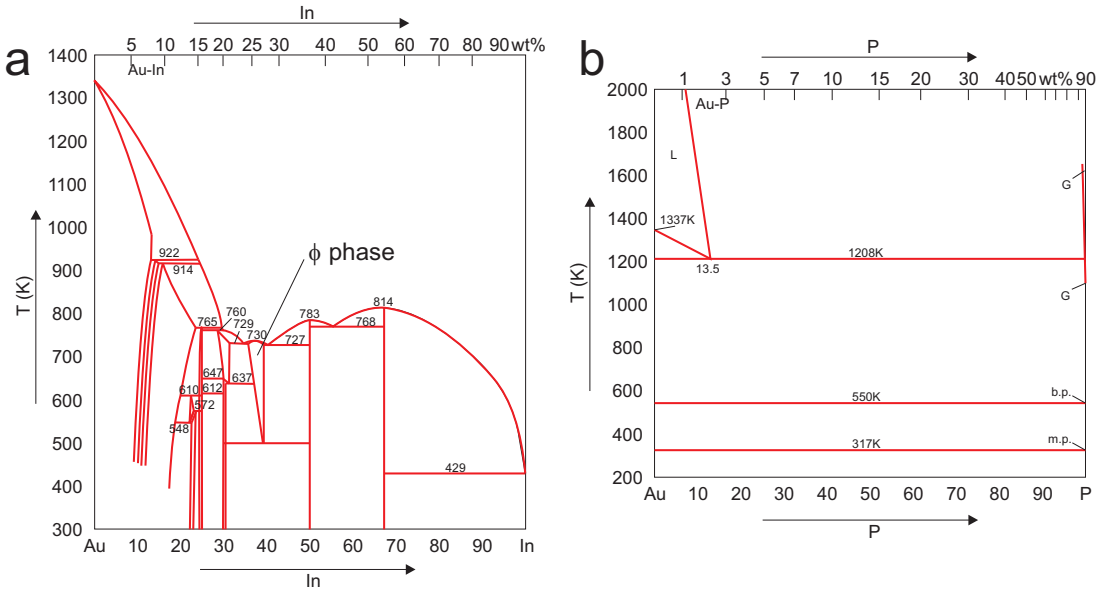

Figure 1.4: Binary phase diagrams (a) Au-In and **(b)** Au-P. At operating temperatures between 400 (673K) and 550 (823K) degrees Celcius the Au-In can be liquid or in the ϕ-phase. **(b)** Shows that there is complete phase separation of Au-P up to 1208K. For a realistic presentation of an AuInP alloy, a ternary phase diagram is needed.

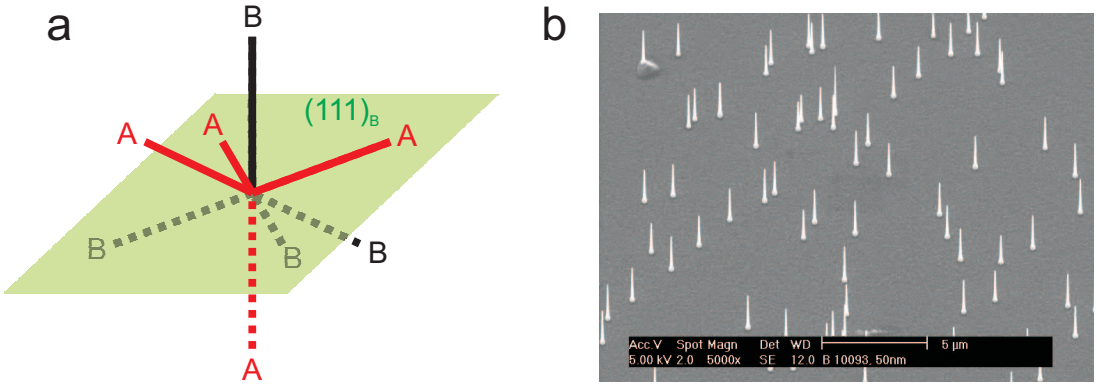

Figure 1.5: Epitaxial growth (a) Difference in A- and B- oriented nanowire growth from a $(111)_B$ substrate of a zinc-blende crystal structure (green). Wires only grow in the $[111]_B$ direction, which results in vertical growth. **(b)** Typical example of GaP nanowires with a diameter of 50 nm grown at 550 °C. The Au was deposited by spin-coating of a colloidal solution on a GaP $(111)_B$ substrate. The sample in the image is tilted 30 degrees from the surface normal to display the vertically grown nanowires.

in crystal growth, which allows for a liquid behavior of the metal particle below the eutectic temperature.
Several groups also report catalyst free nanowire growth. Different mechanisms are reported, such as self catalyzed VLS [32], dislocation driven growth [33, 34], Vapor Solid (VS) growth [27, 28] and oxide assisted nanowire growth [35, 36]. Up to now no evident mechanism is found for the catalyst free growth. Most probably, VLS growth still occurs, however via a catalyst particle consisting of the group III material, such as indium or gallium. During cooling down after growth, under a group V precursor pressure, the remaining catalyst material is consumed and disappears. After growth no particle is present on the top and this has been called "*catalyst free*" nanowire growth. It may, however, also be that VS growth takes place and that the anisotropy of the nanowire crystal lattice induces vertical growth.

1.6 Substrates

The choice of the substrate material and its crystallographic orientation determines several important aspects related to VLS growth. First of all, the substrate and nanowire materials should have roughly the same lattice constants in order to achieve growth. Ideally the lattice mismatch is zero, which is the case for identical nanowire and substrate materials. However, even a mismatch of several percent can result in nanowire growth. The crystallographic orientation as well as the surface atom termination determine the growth direction of the wires. For a III-V wurtzite or zinc-blende (see section 1.12) substrate, the termination of the surface can either be group III-terminated (denoted as "A") or group V-terminated (denoted as "B"). A typical example of vertically grown nanowires is shown in figure 1.5, this is called epitaxial growth. The term epitaxy is derived from the Greek, where "*epi*" means "*above*", and "*taxis*" means "*in ordered manner*". This implies that the epitaxially grown nanowires have a crystallographic relation with the substrate. Since on a $(111)_B$ substrate of the zinc-blende structure growth of the nanowires only occurs in the $[111]_B$ direction this leaves only vertically oriented nanowires with respect to the substrate. As depicted in figure 1.5 there are three $[111]_A$ (in red) and only one $[111]_B$ (in black) directions pointing out of the $(111)_B$ substrate (green layer). If substrates other than $(111)_B$ terminated are used, the preferential growth directions are different.
Important for epitaxial growth is a good interaction between the metal particle and the bare substrate. Typically, a thin (amorphous) oxide layer covers the surface of the substrate, which prevents good contact between the alloy and

the substrate. Therefore it is important to remove the oxide layer. The most commonly used method is by a thermal anneal step performed prior to growth, which removes the oxide layer and ensures a good contact of the metal particle with the substrate. Alternatively, a wet chemical etch step can be performed before metal deposition to remove the oxide. Furthermore, the substrate material influences the surface diffusion and reaction kinetics. Depending on the type of substrate the precursors can be decomposed more efficiently. For example, the precursor tri-methylgallium (TMGa) is decomposed more effectively on a GaP substrate compared to a SiO_2 substrate, resulting in a higher growth rate. Even an oxidized surface will result in other kinetics. Besides decomposition, also the surface diffusion lengths of the precursors are affected by the substrate choice.

1.7 Techniques

Different growth techniques are used by several groups to fabricate nanowires, which all make use of the VLS growth mechanism. The growth techniques mainly differ in the way the source material is brought into the gas phase. Some examples are thermal evaporation, Laser Ablation (LA) [37], Molecular Beam Epitaxy (MBE) [38], Chemical Beam Epixtay (CBE) [39], Vapor Phase Epitaxy (VPE) [40] and Metal Organic Vapor Phase Epitaxy (MOVPE) [41]. The first two offer a very limited control over the partial pressures and uniformity. MBE, MOVPE, and CBE are established techniques to make high quality layered structures. The main advantage of MBE is the high purity of the grown materials. Therefore the highest electron mobility in transport and the smallest optical line widths in quantum wells are obtained with this technique. Typically, the growth rates are very low for MBE making it a suitable technique only for academics. MOVPE, on the other hand, offers high deposition rates and is used in the commercial production of LEDs and lasers.
In this thesis we use a Metal-Organic Vapor Phase Epitaxy [41] reactor, as shown in figure 1.6, to fabricate the nanowires. In MOVPE, precursor molecules are used for the group III and group V atoms. Typical partial pressures are 10^{-2} mbar up to several mbar for the group V and 10^{-5} mbar to 10^{-3} mbar for the group III. A laminar flow, through a quartz liner, of the precursors over the substrate feeds the growth. Hydrogen is used as a carrier gas for the precursors. The substrates are placed on a graphite susceptor which is heated via radio frequency (RF) heating. This allows for an irreversible thermal decomposition reaction of the precursors at the substrate surface. It is important to prevent these reactions to occur in the gas phase since this causes pollution of the reactor walls and cause material memory effects in future experiments. The total reactor pressure is 50 mbar.

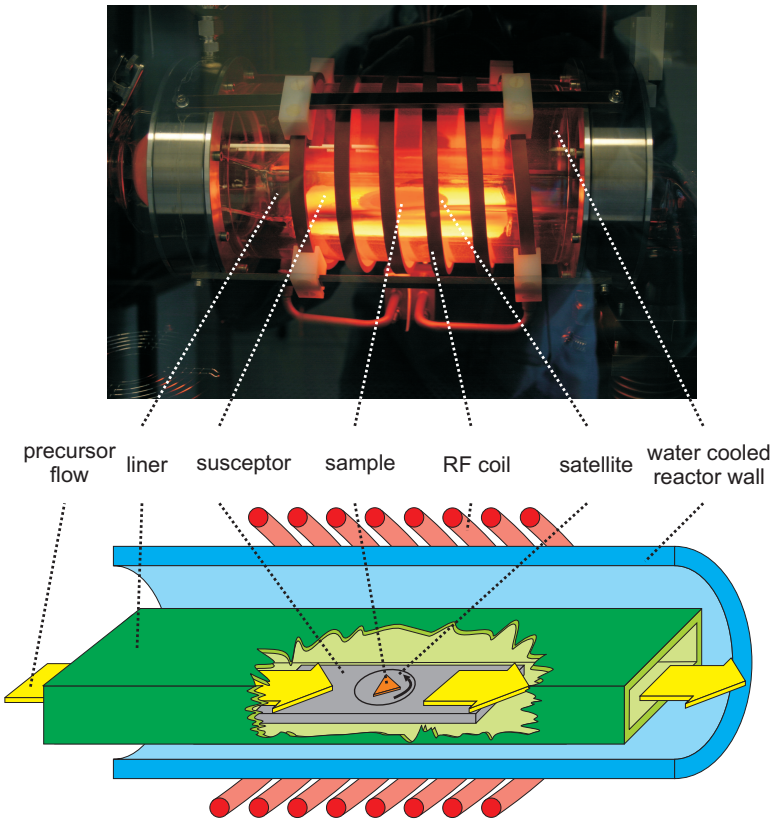

Figure 1.6: MOPVE reactor geometry. Top: the actual reactor during operation. Bottom: a schematic representation of the reactor geometry. The precursor gasses (yellow arrows) flow through a liner (green), over the graphite susceptor (gray). The susceptor is heated via an RF-coil (red). The quartz reactor wall (blue) is water cooled. The sample (orange) is situated on a circular satellite which spins round to give a homogeneous exposure to the precursor gasses.

1.8 Growth parameters

The growth of nanowires is a complex process that involves many parameters. Amongst these parameters are the nature of the substrate (surface), substrate temperature, total pressure, precursor partial pressures, III-V ratios, and impurity concentration, such as dopants. As will be shown throughout this thesis these parameters can affect the crystal structure, morphology and defect density of the nanowires. Some important growth parameters are discussed below. First of all,

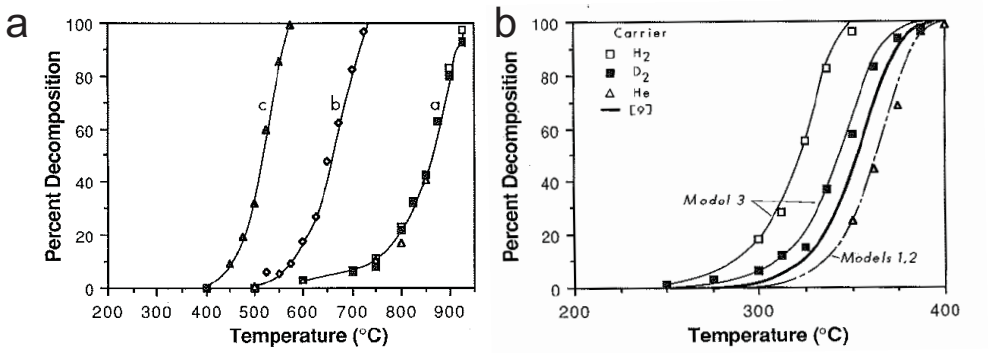

Figure 1.7: Precursor decomposition [42]. Decomposition versus temperature for **(a)** phosphine (PH_3) and **(b)** tri-methyl-Indium (TMIn). The different curves represent process conditions that apply for different reactor dimensions and background pressures, such as H_2, N_2 or D_2.

an anneal step prior to growth can be applied. Here, the substrate is brought to a relatively high temperature compared to the growth temperature. During the anneal a high group V pressure is used to avoid decomposition of the substrate, if III-V substrates are used. The anneal results in alloying of the catalyst particle with the substrate and ensures a good interaction. Furthermore, the chemistry of the substrate surface can be affected by the thermal anneal. For instance, a surface oxide or organic residues from a photoresist can be evaporated and this can affect the surface diffusion kinetics of the precursor molecules. Different precursors can be used during growth. For the group III elements precursors such as tri-methyl-indium (TMIn) or tri-methyl-gallium (TMGa) are used, whereas phosphine (PH_3) and arsine (AsH_3) are used as group V precursors. As a group IV precursor silane (SiH_4) can be used. In all cases hydrogen (H_2) is used as a carrier gas. Important to note is that the bulk decomposition of the precursors is temperature dependent, as shown in figure 1.7 [42]. Therefore the effective III-V ratio is also temperature dependent and is determined by the precursor materials used. As shown in the decomposition graph, figure 1.7, starting from a certain temperature the decomposition becomes effective, followed by a steep increase.

This implies that the supersaturation in the gas phase is critically determined by the decomposition temperature and growth can only occur beyond this point. The metal particle acts as a catalyst and thus catalyse the decomposition of the precursors from the gas phase [9]. Thereby controlled nanowire growth is also possible below the bulk decomposition temperatures.

1.9 Nanowire Materials

The use of different precursors during growth leads to the growth of nanowires composed of different materials. A wide variety of materials is reported in literature which can be, mono, binary and even ternary phase compounds. Mainly group III-V, IV and II-VI nanowires are reported. The first materials system described in literature were Si-whiskers, by Wagner and Ellis in 1964 [1]. From then on nanowires have been grown from many different materials. Group IV materials such as Si [22, 43, 44] and Ge [43] and hetero-structured Si-Ge [45] nanowires are extensively studied. For the group III-V nanowires many examples are reported. Binary materials such as GaP [9, 21, 46–48], GaAs [47–50], InP [46, 47, 51, 52], InAs [53, 54] , GaN [38, 55] and AlAs [47] are only a few examples. Also ternary compounds can be grown, such as InAsP [5]. For device optimization often hetero-structures are required. A hetero-structure is a combination of two different materials in the axial or radial direction. It is not straightforward to make hetero-structured nanowires, since the interface between the different compounds often results in a kinked structure in the axial direction. Here the lattice mismatch could play a role. However, even more important might be the composition of the catalyst particle. By changing materials during growth, also the alloy composition shifts, which can lead to a different catalyst particle volume, droplet contact angles and surface energies. In many cases this results in kinked nanowires [47]. However for GaP-GaAs [20, 56] and InAs-InP [39] axial as well as radial hetero-structures are reported. Finally, group II-VI nanowires such as ZnO [57, 58] are studied intensively because of their interesting optical properties.

1.10 VLS vs Lateral growth

The VLS growth facilitates the growth of the nanowires in the length direction. As shown in figure 1.8 [20] the most direct way of growth is via route 1-4. The precursors travel through the gas phase (1) and are delivered at the catalyst surface where they are decomposed (2). The growth units form an alloy with the

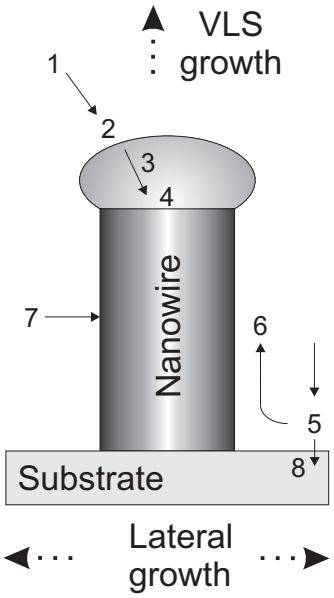

Figure 1.8: Schematic representation of the important processes [20] during growth of the nanowires. Two different types of growth can be distinguished. First, the VLS growth (1-4) which allows for vertical growth of the nanowire. Secondly, lateral growth occurs, which results in tapered nanowires. Processes described in the figure are (1) mass transport through the gas phase, (2) dissociation reaction at the catalyst interface, (3) diffusion through the catalyst, (4) incorporation of growth units at the solid-liquid interface, (5) adsorption of precursors on the substrate, (6) surface diffusion, (7) incorporation of growth units at the side walls of the nanowire and (8) thin film growth on the substrate.

particle and diffuse (3) towards the nanowire-catalyst interface. At the growth interface the growth units are built in into the crystal lattice permitting nanowire growth. Alternatively, precursors from the gas phase can land on the substrate (5) and (partially) decompose. Via surface diffusion over the substrate and the nanowire sidewall (6) the growth units arrive at the catalyst surface from where they are built in (2-4). Before reaching the catalyst particle a competitive growth mechanism can take place. Growth units either can be built in at the substrate resulting in thin film bulk growth (8), or growth units can attach to the sidewall (7) of the nanowire. The sidewall growth results in tapered nanowires, where the base diameter of the wire is larger than the diameter directly below the catalyst particle. This is explained by the longer exposure time for lateral growth of the bottom part of the wires compared to the top part. VLS and lateral growth are competitive growth processes which use the same growth units. Given that the VLS growth is a catalytic process [9] this type of growth will be more pronounced

at low temperatures, whereas the lateral growth will be suppressed. This results in nearly straight and only slightly tapered nanowires. At higher temperatures the contrary takes place and the catalytic VLS growth no longer has an advantage. Lateral growth and consequently tapered wires are the result [20].

1.11 Nanowire Geometries

Numerous nanowire geometries are required to fabricate a wide variety in devices for applications mentioned is section 1.1. Therefore it is essential to control the shape and composition of the nanowires. Uniform structures as well as axial and lateral hetero-structures composed of different materials or dopant profiles are important. Several examples of nanowire geometries are shown in figure 1.9. To achieve this the crystal structure, morphology, and defects in the nanowires are the basic parameters which need to be controlled, since they can affect the optical and electrical properties of the wires.

Up to now no industrial applications are known for nanowires. However a lot of effort is put into the fabrication of electrical devices such as electrical switches or quantum dots inside nanowires [59–61]. The main problem is making good ohmic contacts for the different nanowire materials. Furthermore, the control in the size and composition of the quantum dots is the key to obtain small line widths in the photoluminescence emission. Optical devices are made, such as photon emitters, photodetectors [62] and waveguides which make use of the high nanowire aspect ratio. By intentionally doping semiconducting nanowires radially [63], as well as axially [41, 64] p-n junctions can be fabricated, which can result in single photon emitters/detectors, logic gates and LED's. Also solar cells [8, 65, 66] and lasers [7, 57, 67, 68] are very promising nanowire applications. Antireflection coatings are necessary to effectively couple light into solar cells. Tapered nanowires result in a gradual increase of the refractive index towards the surface and a broad-band omni-directional antireflection coating can be made [69]. Furthermore, the possibilities to create sensors from nanowires are explored. Here a nanowire is chemically functionalized, aimed to capture specific molecules. When the target molecule(s) are captured the electronic resistance of the wire is affected and this is used as a quantitative measure for the concentration. In this way highly sensitive biological and chemical sensors can be fabricated, and even concentrations as low as femto-molars can be detected [4]. Here the electrical contacts and electrical behavior of the wire is very important and not yet completely understood. The selectivity of the sensor is also an important issue, which needs to be solved in order to make commercially interesting sensors.

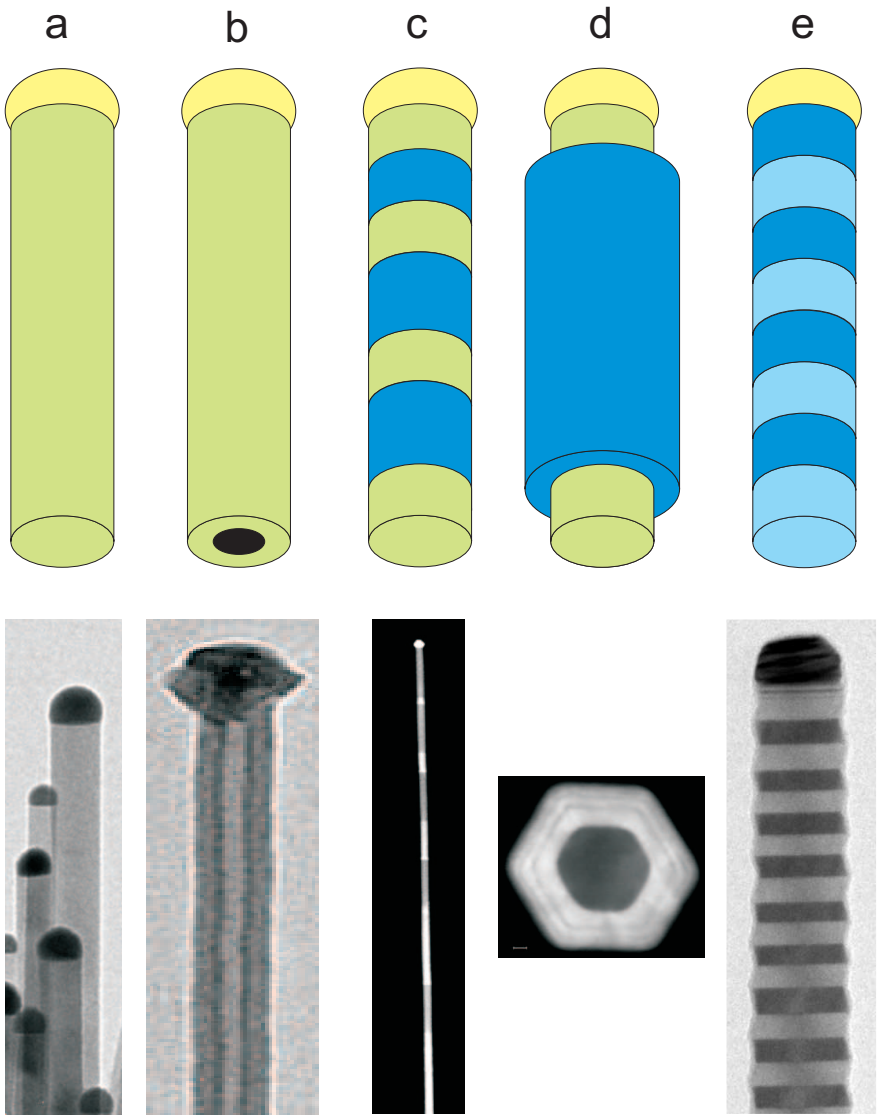

Figure 1.9: Schematic drawing of different nanowire geometries accompanied by TEM images of real examples. The different colors (blue-green) represent different materials, whereas the different color intensities (dark and light blue) symbolize rotations of the crystal lattice (twin planes) in homogeneous material wires. Examples: (**a**) Homogeneous S-doped InP nanowire (**b**) Hollow InP nanotube [51] (**c**) Axial hetero-structured nanowire consisting of alternating GaP-GaAs segments in the length direction of the wire [20] (**d**) Lateral hetero-structured nanowire starting with a GaP core [20] (dark) followed by a GaAs shell (light) (**e**) Twinning superlattice InP nanowire where the dark and light correspond to differently oriented segments with the same crystal structure (twin plane)[52].

1.12 Crystal structure

Different crystalline phases are observed in nanowires. The zinc-blende and wurtzite crystal structures are observed most frequently for III-V nanowires. The zinc-blende crystal structure has a face centered cubic lattice, whereas the wurtzite crystal structure has a hexagonal lattice. As shown in figure 1.10 the two crystal structures consist of a stacking of bi-layers in the [111] zinc-blende and [0001] wurtzite crystallographic direction. These cubic and hexagonal bi-layers are from a crystallographic point of view equivalent. Each bi-layer (A, B and C) consists of both group III and group V atoms. For the two crystal structures a different stacking sequence is found. The zinc-blende crystal structure has an ABCABC layering. The wurtzite crystal structure, however, has an ABAB layering. Different crystal structures have their own specific optical properties, such as bandgap [70, 71], and emit at different wavelengths. Furthermore, the morphology of the wires is related to the crystal structure. In turn the crystal structure affects the formation of side-facets. Therefore it is important to understand and control the occurrence of different crystal structures in nanowires.

1.13 Morphology

Besides different crystal structures the nanowires can also have different morphologies. The morphology is determined by the side facets of the wire. The nature of the side facets is determined by the crystal structures, or vice versa [50] and depends strongly on the growth parameters (as shown in chapter 2). The most common and stable side facets for the zinc-blende crystal structure are non-parallel {111} side facets with respect to the $<111>_B$ growth direction. Here the three fold symmetry cross-sectional shape of the wire consists of three $\{111\}_B$ and three $\{111\}_A$ facets. The terminology "A" and "B" stands for a group III or group V terminated facet, respectively. These different surface terminations result in different surface energies of the side facets [50]. As a result, differently terminated facets can have different growth rates. The cross-sectional shape of the nanowire is affected by the non-uniform growth rates and becomes triangularly shaped by continued growth. Besides stable {111} facets other commonly found facets in the zinc-blende structure are $\{11\bar{2}\}$. These facets are composed of adjacent {111} and {100} nano-facets in a ratio of 2:1. This results in $\{11\bar{2}\}$ facets which run parallel to the length axis of the nanowire. For the wurtzite structure mainly $\{1\bar{1}00\}$ side facets are found which, similarly to the $\{11\bar{2}\}$ zinc-blende facets, run parallel to the wire length axis, for a [0001] growth direction. During growth of the nanowire the side facets evolve and, depending on the type

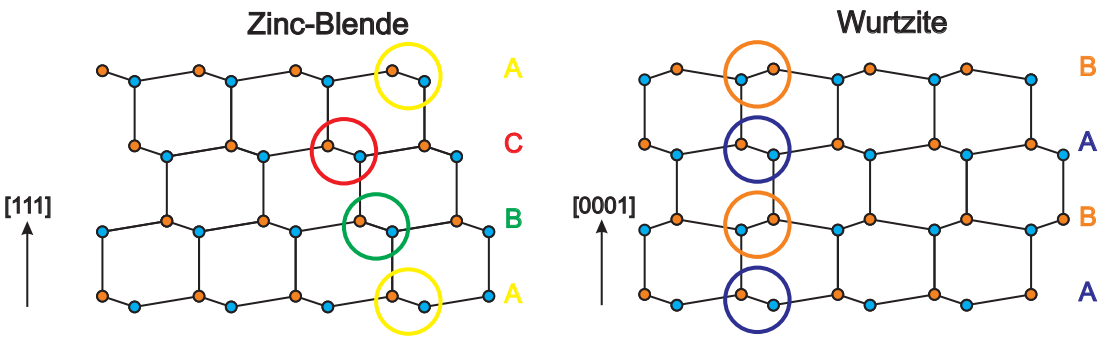

Figure 1.10: The two most frequently observed crystal structures for III-V nanowires. Blue circles in the lattices stand for group III atoms, and orange circles represent group V atoms. In **(a)** the cubic zinc-blende crystal structure is shown with an ABCABC layering along the [111] direction. Each layer consists of group III and group V atoms. In **(b)** the hexagonal wurtzite crystal structure is shown with ABAB layering along the [0001] direction. The [111] and [0001] directions are complementary and both crystal structures fit on each other along this direction. The top faces of both structures displayed are terminated by group V atoms (B-terminated); the bottom faces by group III atoms (A-terminated)

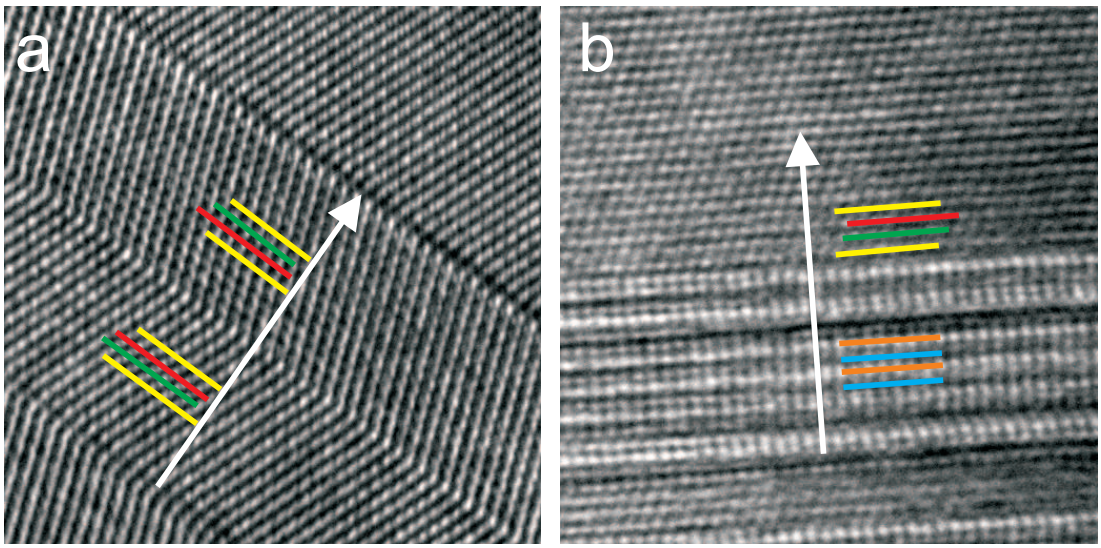

Figure 1.11: Crystal structures. Example of a rotational twin plane in zinc-blende **(a)** and a structure switch from wurtzite into zinc-blende **(b)**. The white arrow indicates the length axis, *i.e.* growth direction, of the nanowire. The color coding shows the layering of the different crystal structures.

of facet, this can change the cross-sectional shape of the growth interface. This modifies the contact angles of the catalyst particle on top of the wire. As shown in chapters 4 and 5 this results in formation of twins in a regular fashion.

1.14 Defects

Crystal structures often show imperfections, called defects [72]. These defects come in many different varieties, such as point defects (vacancies, interstitials) and line defects (screw and edge dislocations). Furthermore, planar defects such as grain boundaries, anti-phase boundaries, stacking faults and twins are well known in crystal structures. In nanowires stacking faults are a widespread phenomenon. In terms of layering a 'fault' layer is introduced and thereby interrupts the perfect crystalline phase. These defects can affect the optical, electrical and material properties of the nanowires and therefore need to be controlled. A stacking fault (twin plane [73, 74]) reverses the ABCABC zinc-blende layering in the following way: ABCA**BCB**ACBAC. This fault leaves a rotation of the original crystal structure of 180 degrees along [111], which is called a twin plane [72]. Alternatively this layer can be described as a monolayer [74, 75] of the wurtzite structure (shown bold). For the wurtzite crystal structure the normal ABABAB layering is interrupted by a different layer resulting in a ABAB**ABC**BCBC layering. This effectively results in one monolayer [74, 75] of the zinc-blende structure (shown bold), called a stacking fault. The layering of the nanowire can be observed by high resolution TEM when viewing along a zone axis $<1\bar{1}0>$, as shown in figure 1.11. The stacking faults (twin planes) occur mainly perpendicular to the [111] or [0001] growth directions of the nanowire zinc-blende and wurtzite crystal structures, respectively (or parallel to the $[11\bar{2}]$ growth direction of zinc-blende). As will be shown in this thesis twin planes can occur in different fashions along the nanowire. They can be randomly dispersed along the length axis, come in pairs or even form a twin superlattice structure.

1.15 Scope of this thesis

In this thesis several aspects of nanowire growth, such as temperature, III-V ratio, impurities, and particle size and shape are investigated for their influence on the morphology and crystalline structure of the nanowire. In chapter 2 the morphology of GaP nanowires will be discussed. Different stable morphologies, bounded by {111} and $\{11\bar{2}\}$ facets of the zinc-blende crystal structure, are shown as a function of the temperature and III-V ratios. At high temperatures an other crystal structure, wurtzite, is observed. By TEM tomography it is shown that the morphology of the nanowires result in hexagonally or more triangularly shaped nanowires depending on the growth conditions. In chapter 3 we show that the triangular morphology of the nanowire is a key element in the formation of a special case of defects: 'Paired twins'. These twin pairs occur in overall $\{11\bar{2}\}$ facetted GaP nanowires. In such pairs the first twin plane is formed at a random position, rapidly followed by the formation of a second twin plane of which the position is directly related to that of the first one.

In chapter 4 the formation of twin planes with constant interspacing is studied in great detail in InP nanowires. We have found that upon addition of Zn during growth (to induce p-doping), the zinc blende crystal structure is formed, rather than the normally observed wurtzite crystal structure for undoped wires. At high Zn-concentrations a twin superlattice is created. In this case the twin planes are spaced at an equal distance along the length axis of the InP nanowire. The regular twin structure can be called a superlattice. A model for twin formation based on the development of the nanowire morphology and its effect on the droplet shape is presented. Based on the same principles the twin superlattice is extended to another materials system: GaP nanowires. This material is optically more interesting because of its indirect bandgap. Twin superlattices are predicted to give rise to minibands in the band structure of a material and thereby inducing a direct transition in normally indirect materials [76]. This could lead, in the case of GaP, to an efficient green light emitter [77]. To create such a direct transition the segment length between two successive twin planes and the period distribution of the twin superlattice are key parameters which need to be controlled. In chapter 5 it is shown that by influencing the partial pressure of the gallium precursor during growth these parameters can be controlled. Moreover, the supersaturation and the surface energies are affected by this pressure, which we can describe by the same model as described for InP superlattices. To understand the effect of Zn addition on zinc-blende and twin superlattice formation, surface X-ray diffraction experiments were performed on bulk AuIn and AuInZn layers on InP substrates. The data is shown in chapter 6, where we report ordering of 3-4 layers in the

z-direction of the liquid alloy phase. On top of the solid substrate an In rich first layer is found, followed by 2-3 layers of the pure eutectic phase Au_3In_2. No effect of Zn was observed. The first layer is slightly ordered in the lateral direction in such a way that the In atoms are positioned on the wurtzite sites. This probably is the reason why we find a wurtzite crystal structure in the undoped InP nanowires.
Finally, chapter 7 elaborates on a different topic, which opens the way to future experiments and applications. By using nano-imprint lithography the metal particles, needed for nanowire growth, can be positioned on a full 2-inch wafer in a predesigned pattern. Positioning of the wires is crucial in order to understand and control fundamental aspects such as competition between the wires. Additionally, positioning is essential for nanowire uniformity and future device fabrication. Nano-imprint allows for cheap positioning of metal particles. In chapter 7 two steps, a wet chemical treatment and a thermal anneal, necessary to achieve perfect nanowire growth in an ordered way are discussed.

References

[1] R. Wagner and W. Ellis, "Vapor-Liquid-Solid mechanism of single crystal growth," *Applied Physics Letters*, vol. 4, pp. 89–90, 1964.

[2] Y. Li, J. Xiang, F. Qian, S. Gradeak, Y. Wu, H. Yan, D. A. Blom, and C. M. Lieber, "Dopant-Free GaN/AlN/AlGaN Radial Nanowire Heterostructures as High Electron Mobility Transistors," *Nano Lett.*, vol. 6, pp. 1468–1473, 2006.

[3] A. Lui and M. Paniccia, "Advances in silicon photonic devices for silicon based optoelectronic applications," *Physica E*, vol. 35, pp. 223–228, 2006.

[4] G. Zheng, F. Patolsky, Y. Cui, W. Wang, and C. Lieber, "Multiplexed electrical detection of cancer markers with nanowire sensor arrays," *Nat. Bio.*, vol. 23, pp. 1294–1301, 2005.

[5] M. van Weert, N. Akopian, U. Perinetti, M. van Kouwen, R. Algra, M. Verheijen, E. Bakkers, L. Kouwenhoven, and V. Zwiller, "Selective Excitation and Detection of Spin States in a Single Nanowire Quantum Dot," *Nano Letters*, vol. 4, pp. 1989–1993, 2009.

[6] M. Krames, O. Shchekin, R. Mueller-Mach, G. Mueller, L. Zhou, G. Harbers, and M. Craford, "Status and future of high-power- light-emitting diodes for solid-state lighting.," *J. Display Tech.*, vol. 3, pp. 160–175, 2007.

[7] X. Duan, Y. Huang, R. Agarwal, and C. Lieber, "Single nanowire electriclally driven lasers," *Nature*, vol. 421, p. 241, 2003.

[8] M. Law, L. Greene, J.C.Johnson, R. Saykally, and P. Yang, "Nanowire dye sensitized solar cells," *Nature Mat.*, vol. 4, p. 455, 2005.

[9] M. Borgström, G. Immink, B. Ketelaars, R. Algra, and E. Bakkers, "Synergetic nanowire growth," *Nature Nanotechnology*, vol. 2, p. 541, 2007.

[10] M. Gudikses and C. Lieber, "Diameter selective synthesis of semiconducting nanowires," *J. Am. Chem. Soc.*, vol. 122, pp. 8801–8802, 2000.

[11] I. Doron-Mor, Z. Barkay, N. Filip-Granit, A.Vaskevich, and I. Rubinstein, "Ultrathin Gold Island Films on Silanized Glass. Morphology and Optical Properties," *Chem.Mater.*, vol. 16, p. 3476, 2004.

[12] A. I. Hochbaum, R. Fan, R. He, and P. Yang, "Controlled Growth of Si Nanowire Arrays for Device Integration," *Nano Lett.*, vol. 5, p. 457, 2005.

[13] M. Magnusson, K. Deppert, J.-O. Malm, and L. Samuelson, "Gold nanoparticles: production, reshaping and thermal charging," *Journal of Nanoparticle Research*, vol. 1, pp. 243–251, 1999.

[14] T. Mårtensson, C. Patrik, T. Svensson, B. A. Wacaser, M. W. Larsson, W. Seifert, K. Deppert, A. Gustafsson, R. L. Wallenberg, and L. Samuelson, "Epitaxial III-V nanowires on silicon," *Nano Lett.*, vol. 4, pp. 1987–1990, 2004.

[15] P. Mohan, J. Motohisa, and T. Fukui, "Controlled growth of highly uniform, axial/radial direction-defined, individually addressable InP nanowire arrays," *Nanotechnology*, vol. 16, pp. 2903–2907, 2005.

[16] L. Jensen, M. Bjork, S. Jeppesen, A. Persson, B. Ohlsson, and L. Samuelson, "Role of Surface Diffusion in Chemical Beam Epitaxy of InAs Nanowires," *Nano Letters*, vol. 4, pp. 1961–1964, 2004.

[17] M. Verschuuren and S. Wuister, "Imprint lithography," *US patent*, US 2008/0011934, 17/01/08.

[18] A. Pierret, M. Hocevar, S. Diedenhofen, R. Algra, E. Vlieg, E. Timmering, M. Verschuuren, G. Immink, M. Verheijen, and E. Bakkers, "Generic nanoimprint process for fabrication of nanowire arrays," *Nanotechnology*, vol. 21, p. 065305, 2010.

[19] M. Borgström, G. Immink, B. Ketelaars, R. Algra, and E. Bakkers, "Synergetic nanowire growth," *Nature Nanotechnology*, vol. 2, pp. 541–544, 2007.

[20] M. A. Verheijen, G. Immink, T. de Smet, M. T. Borgstrom, and E. P. A. M. Bakkers, "Growth Kinetics of Heterostructured GaP-GaAs Nanowires.," *J. Am. Chem. Soc.*, vol. 128, pp. 1353–1359, 2006.

[21] J. Johansson, L. S. Karlsson, C. Patrik, T. Svensson, T. Mårtensson, B. A. Wacaser, K. Deppert, L. Samuelson, and W. Seifert, "Structural properties of $(111)_B$-oriented III-V nanowires.," *Nat. Materials*, vol. 5, pp. 574–580, 2006.

[22] J. B. Hannon, S. Kodambaka, F. M. Ross, and R. M. Tromp, "The influence of the surface migration of gold on the growth of silicon nanowires," *Nature*, vol. 440, p. 69, 2006.

[23] Q. Li and G. Wang, "Improvement in aligned GaN nanowire growth using submonolayer Ni catalyst films," *Appl. Phys. Lett.*, vol. 93, p. 043119, 2008.

[24] J. Baea, N. Kulkarnib, J. Zhouc, J. Ekerdtd, and C. Shih, "VLS growth of Si nanocones using Ga and Al catalysts," *J. Cryst. Growth*, vol. 310, pp. 4407–4411, 2008.

[25] B. Kayes, M. Filler, M. Putnam, M. Kelzenberg, N. Lewis, and H. Atwater, "Growth of vertically aligned Si wire arrays over large areas (>1 cm^2) with Au and Cu catalysts," *Appl. Phys. Lett.*, vol. 91, p. 103110, 2007.

[26] Landolt-Bornstein, *New Series IV/5a*.

[27] K. Ikejiri, J. Noborisaka, S. Hara, J. Motohisa, and T. Fukui, "Mechanism of catalyst-free growth of GaAs nanowires by selective area MOVPE," *J.Cryst. Growth Thirteenth International Conference on Metal Organic Vapor Phase Epitaxy (ICMOVPE XIII)*, vol. 298, p. 616, 2007.

[28] R. K. Debnath, R. Meijers, T. Richter, T. Stoica, R. Calarco, and H. Lüth, "Mechanism of molecular beam epitaxy growth of GaN nanowires on Si(111)," *APL*, vol. 90, p. 123117, 2007.

[29] S. Kodambaka, J. Tersoff, M. C. Reuter, and F. M. Ross, "Germanium Nanowire Growth Below the Eutectic Temperature," *Science*, vol. 316, pp. 720–732, 2007.

[30] K. Dick, S. Kodambaka, M. Reuter, K. Deppert, L. Samuelson, W. Seifert, L. Wallenberg, and F. Ross, "The Morphology of Axial and Branched Nanowire Heterostructures," *Nano lett.*, vol. 7, pp. 1817–1822, 2007.

[31] B. S. Sorensen, M. Aagesen, C. B. Sorensen, P. E. Lindelof, K. L. Martinez, and J. Nygård, "Ambipolar transistor behavior in p-doped InAs nanowires grown by molecular beam epitaxy," *Appl. Phys. Lett.*, vol. 92, p. 012119, 2008.

[32] S. N. Mohammad, "Self-catalytic solution for single-crystal nanowire and nanotube growth," *J. Chem. Phys.*, vol. 127, p. 244702, 2007.

[33] M. J. Bierman, Y. K. A. Lau, A. V. Kvit, A. L. Schmitt, and S. Jin, "Dislocation- Driven Nanowire Growth and Eshelby Twist," *Science*, vol. 320, p. 1060, 2008.

[34] J. Zhu, H. Peng, A. F. Marshall, D. M. Barnett, W. Nix, and Y. Cui, "Formation of chiral branched nanowires by the Eshelby Twist," *Nature Nanotechnolgy*, vol. 3, p. 477, 2008.

[35] W. S. Shi, Y. F. Zheng, N. Wang, C. S. Lee, and S. T. Lee, "Oxide-assisted growth and optical characterization of gallium-arsenide nanowires," *APL*, vol. 78, p. 3304, 2001.

[36] R.-Q. Zhang, Y. Lifshitz, and S.-T. Lee, "Oxide-assisted Growth of semiconducting Nanowires," *Adv. Mat.*, vol. 15, p. 635, 2003.

[37] A. M. Morales and C. M. Lieber, "A Laser Ablation Method for the Synthesis of Crystalline Semiconductor Nanowires," *Science*, vol. 279, p. 208, 1998.

[38] A. Cavallini, L. Polenta, M. Rossi, T. Richter, M. Marso, R. Meijers, R. Calarco, and H. Lüth, "Defect Distribution along Single GaN Nanowhiskers," *Nano Lett.*, vol. 6, p. 1548, 2006.

[39] M. T. Björk, B. J. Ohlsson, T. Sass, A. I. Persson, C. Thelander, M. H. Magnusson, K. Deppert, L. R. Wallenberg, and L. Samuelson, "," *Nano Lett.*, vol. 2, p. 87, 2002.

[40] T. Shin, H. Lee, W. Song, H. Kim, S. Kim, and D. Yoon, "High quality GaN nanowires synthesized from Ga_2O_3 with graphite powder using VPE method," *Colloids and Surfaces A: Physicochemical and Engineering Aspects*, vol. 313, p. 52, 2008.

[41] K. Haraguchi, T. Katsuyama, K. Hiruma, and K. Ogawa, "GaAs p-n junction formed in quantumwire crystals," *APL*, vol. 60, p. 745, 1992.

[42] G. Stringfellow, *Growth mechanism of truncated triangular III-V nanowires.* Academic press, 1999.

[43] E. I. Givargizov, "Fundamental Aspects of VLS Growth," *J. Cryst. Growth*, vol. 31, p. 20, 1975.

[44] F. M. Ross, J. Tersoff, and M. C. Reuter, "Sawtooth faceting in silicon nanowires.," *Phys. Rev. Lett.*, vol. 95, p. 146104, 2005.

[45] L. J. Lauhon, M. S. Gudiksen, C. L. Wang, and C. M. Lieber, "Epitaxial core-shell and core-multishell nanowire heterostructures.," *Nature*, vol. 420, pp. 57–61, 2002.

[46] X. Duan and C. M. Lieber, "General Sythesis of Compound Semiconductor Nanowires," *Adv.Mat*, vol. 12, p. 298, 2000.

[47] K. Dick, S. Kodambaka, M. Reuter, K. Deppert, L. Samuelson, W. Seifert, L. Wallenberg, and F. Ross, "The morphology of axial and branched nanowires hetereostructures," *Nano Lett.*, vol. 7, p. 1817, 2007.

[48] M. Verheijen, R. Algra, M. Borgström, G. Immink, E. Sourty, W. van Enckevort, E. Vlieg, and E. Bakkers, "Three dimensional morphology of GaP-GaAs nanowires revealed by transmission electron microscopy tomography.," *Nano Lett.*, vol. 7, pp. 3051–3055, 2007.

[49] K. Hiruma, M. Yazawa, T. Katsuyama, K. Ogawa, K. Haraguchi, M. Koguchi, and H. Kakibayashi, "Growth and optical properties of nanometer-scale GaAs and InAs whiskers," *Applied Physics Reviews*, vol. 77, p. 447, 1995.

[50] F. Glas, J. Harmand, and G. Patriarche, "Why does Wurtzite form in nanowires of III-V Zinc Blende semiconductors? ," *Phys. Rev. Lett.*, vol. 99, p. 146101, 2007.

[51] E. Bakkers and M. A. Verheijen, "Synthesis of InP nanotubes," *J. Am. Chem. Soc.*, p. 3440, 2003.

[52] R. Algra, M. Verheijen, M. Borgström, L. Feiner, G. Immink, W. van Enckevort, E.Vlieg, and E. Bakkers, "Twinning superlattices in indium phosphide nanowires," *Nature*, vol. 456, pp. 369–372, 2008.

[53] J. Johansson, B. Wacaser, K. Dick, and W. Seifert, "Growth related aspects of epitaxial nanowires," *Nanotechnology*, vol. 17, pp. S355–61, 2006.

[54] K. Dick, K. Deppert, L. Karlsson, L. Wallenberg, L. Samuelson, and W. Seifert, "A new understanding of Au-assisted growth of III-V semiconductor nanowires," *Adv. Func. Mater.*, vol. 15, pp. 1603–10, 2005.

[55] X. Duan and C. M. Lieber, "Laser-Assisted Catalytic Growth of Single Crystal GaN Nanowires," *J. Am. Chem. Soc.*, vol. 122, p. 188, 2000.

[56] M. Gudiksen, L. Lauhon, J. Wang, D. Smith, and C. Lieber, "Growth of nanowire superlattice structures for nanoscale photonics and electronics.," *Nature*, vol. 415, pp. 617–620, 2002.

[57] M. H. Huang, S. Mao, H. Feick, H. Yan, Y. Wu, H. Kind, E. Weber, R. Russo, and P. Yang, "Room-temperature ultraviolet nanowire nanolasers," *Science*, vol. 292, pp. 1897–1899, 2001.

[58] L. K. van Vugt, S. Rühle, and D. Vanmaekelbergh, "Phase-Correlated Nondirectional Laser Emission from the End Facets of a ZnO Nanowire.," *Nano Lett.*, vol. 6, p. 2707, 2006.

[59] M. van Weert, A. Helman, W. van den Einden, R. Algra, M. Verheijen, M. Borgström, G. Immink, J. Kelly, L. Kouwenhoven, and E. Bakkers, "Zinc Incorporation via the Vapor-Liquid-Solid Mechanism into InP Nanowires," *Journal of the American Chemical Society*, vol. 131, pp. 4578–4579, 2009.

[60] M. van Weert, N. Akopian, F. Kelkensberg, U. Perinetti, M. van Kouwen, J. Gomez-Rivas, M. Borgström, R. Algra, M. Verheijen, E. A. M. Bakkers, L. Kouwenhoven, and V. Zwiller, "Orientation-Dependent Optical-Polarization Properties of Single Quantum Dots in Nanowires," *Small*, vol. 5, pp. 2134–2138, 2009.

[61] M. van Kouwen, A. Hidma, M. Reimer, M. van Weert, R. Algra, E. Bakkers, L. Kouwenhoven, and V. Zwiller, "Single Electron Charging in Optically-Active Nanowire Quantum Dots," *Nano Lett.*, vol. 10, pp. 1817–1822, 2010.

[62] J. Wang, M. Gudiksen, X. Duan, Y. Cui, and C. Lieber, "Highly polarized photoluminescence and photodetection from single indium phosphide nanowires," *Science*, vol. 293, p. 1455, 2001.

[63] B. Tian, X. Zheng, T. J. Kempa, Y. Fang, N. Yu, G. Yu, J. Huang, and C. M. Lieber, "Coaxial silicon nanowires as solar cells and nanoelectronic power sources," *Nature*, vol. 449, p. 885, 2007.

[64] E. Minot, F. Kelkensberg, M. V. Kouwen, J. V. Dam, and L. Kouwenhoven, "Single Quantum dot nanowire LEDs ," *Nano Letters*, vol. 7, pp. 367–371, 2007.

[65] E. Garnett and P. Yang, "Silicon nanowire radial p-n junction solar cells," *J. Am. Chem. Soc.*, vol. 130, p. 9224, 2008.

[66] J. Czaban, D. Thompson, and R. LaPierre, "GaAs core shell nanowires for photovoltaic applications," *Nano Lett.*, vol. 9, p. 148, 2009.

[67] A. Chin, S. Vaddiraju, A. Maslov, C. Ning, M. Sunkara, and M. Meyyappan, "Near-Infrared semiconductor subwavelength-wire lasers," *APL*, vol. 88, p. 163115, 2006.

[68] B. Hua, J. Motohisa, Y. Kobayashi, S. Hara, and T. Fukui, "Single GaAs/GaAsP coaxial core shell nanowire lasers," *Nano Lett.*, vol. 9, p. 112, 2009.

[69] S. Diedenhofen, G. Vecchi, R. Algra, A. Lagendijk, A. Hartsuiker, O. Muskens, G. Immink, E. Bakkers, W. Vos, and J. G. Rivas, "Broadband and omnidirectional antireflection coating based on semiconductor nanorods," *Advanced Materials*, vol. 21, pp. 973–978, 2009.

[70] K. Pemasiri, M. Montazeri, R. Gass, L. Smith, H. Jackson, J. Yarrison-Rice, S. Paiman, Q. Gao, H. Tan, C. Jagadish, X. Zhang, and J. Zou, "Carrier dynamics and quantum confinement in type II ZB-WZ InP nanowire homostructures," *Nano Lett.*, vol. 9, pp. 648–654, 2009.

[71] M. Mattila, T. Hakkarainen, M. Mulot, and H. Lipsanen, "Crystal-structure-dependent photoluminescence from InP nanowires.," *Nanotechnology*, vol. 17, pp. 1580–1583, 2006.

[72] H. Rosenberg, *The Solid State*, vol. 3^{rd} edition. Oxford Science Publications, 2000.

[73] S. Bhunia, T. Kawamuraa, S. Fujikawab, H. Nakashimaa, K. Furukawaa, K. Torimitsua, and Y. Watanabea, "Vapor-liquid-solid growth of vertically aligned InP nanowires by metalorganic vapor phase epitaxy," *Thin solid film*, vol. 464, pp. 244–247, 2004.

[74] K. Hiruma, M. Yazawa, T. Katsuyama, K. Ogawa, K. Haraguchi, M. Koguchi, and H. Kakibayashi, "Growth and optical properties of nanometer scale GaAs and InAs whiskers.," *J. Appl. Phys.*, vol. 77, pp. 447–462, 1995.

[75] P. Mohseni, C. Maunders, G. Botton, and R. LaPierre, "GaP/GaAsP/GaP core- multishell nanowire heterostructures on (111) silicon," *Nanotechnology*, vol. 18, p. 445302, 2007.

[76] Z. Ikonic, G. P. Srivastava, and J. C. Inkson, "Optical properties of twinning superlattices in diamond-type and zinc-blende-type semiconductors.," *Phys. Rev. B*, vol. 52, pp. 14078–14085, 1995.

[77] S. Nakamura, "Current status of GaN based solid state lighting," *MRS Bulletin*, vol. 34, pp. 101–107, 2009.

Chapter 2

Three dimensional morphology of GaP-GaAs nanowires revealed by transmission electron microscopy tomography

Marcel A. Verheijen, Rienk E. Algra, Magnus T. Borgström, George Immink, Erwan Sourty, Willem J.P. v. Enckevort, Elias Vlieg, Erik P. A. M. Bakkers

We have investigated the morphology of heterostructured GaP-GaAs nanowires grown by metal-organic vapor-phase epitaxy as a function of growth temperature and V/III precursor ratio. The study of heterostructured nanowires with transmission electron microscopy tomography allowed the three-dimensional morphology to be resolved, and discrimination between the effect of axial (core) and radial (shell) growth on the morphology. A temperature- and precursor-dependent structure diagram for the GaP nanowire core morphology and the evolution of the different types of side facets during GaAs and GaP shell growth were constituted.

This chapter has been published in *Nano Letters, vol 7, no. 10 p. 3051-3055* 2007.

2.1 Introduction

Semiconductor nanowires are promising candidates for enabling integration of new functionalities [1–4] based on the advantageous properties of III-V semiconductors, such as high carrier mobility and optical activity into existing silicon technology [5–8]. Because of the small dimensions and the consequently large ratio of surface to bulk atoms, the nanowire surface morphology and resulting chemistry can considerably affect the nanowire (opto-) electronic properties, such as carrier mobility [9] and luminescence quantum yield [10, 11]. An elegant way to suppress such surface related effects is to cap the wires with a wide band gap material to form core/ shell [12–15] nanowire structures. So far, only the vapor-liquid-solid (VLS), *i.e.*, the axial growth mechanism and the zinc blende crystal structure, has been considered in relation to the III-V nanowire side faceting [16–19]. In order to design and optimize nanowire properties for optical, electrical, or mechanical performance, it is essential to take control over the nanowire surface morphology by fully understanding the parameters affecting radial growth. In this paper we demonstrate the versatility of three-dimensional (3D) transmission electron microscopy (TEM) tomography, allowing the study of facet formation during radial overgrowth and the complex behavior of nanowire morphology as a function of precursor molar fractions and growth temperature. Furthermore, we make a distinction between the morphology determined by the axial VLS growth and the morphology introduced by additional radial (non-VLS) side-wall growth.

2.2 Experimental

Axial multisegment GaP-GaAs heterostructure nanowires were synthesized on oxidized Si substrates in an Aixtron 200 MOVPE reactor, as previously described in reports on growth kinetics [15] and heterostructure interfaces [20] of these nanowires. By means of switching of the precursor gases, alternating segments of GaP and GaAs were grown as a single crystalline structure [21]. It is essential to realize that during vertical (VLS) growth of the nanowire, radial epitaxial sidewall growth also occurs [21]. Therefore, the alteration of precursor gases introduces a series of shells of alternating composition. All samples were studied with a FEI Tecnai 300 kV TEM in bright field, high resolution TEM (HRTEM) as well as in high-angle annular dark field (HAADF) mode. Scanning TEM (STEM) tomography was performed using the automated tilt-series acquisition software Xplore3D on a FEI Tecnai F20 X-Twin operated at 200 kV. HAADF images were acquired at 2 ° tilt intervals in a tilt range of -68 ° to +68 ° using a Fischione single tilt tomography holder. Data processing and visualization were performed using

Inspect3D and Amira, respectively (Xplore3D software suite). We address the morphology of ⟨111⟩ grown wires with twin boundaries oriented perpendicular to the VLS growth direction only but note that about 5% of the characterized wires exhibited a $\langle 11\bar{2}\rangle$ growth direction. The latter growth direction only appeared in restricted sections of the wires bounded by kinked transitions to ⟨111⟩ grown sections.

2.3 Nanowire morphologies

Nanowire core morphologies were determined from the orientation of the side facets just below (<100 nm) the gold particle and precisely at a GaP/GaAs heterojunction in tomography studies. Here, the effects of sidewall growth are minor because of the short exposure time of the facets to the supply of growth units and the low radial growth rates in the temperature range 460 °C < T < 530 °C [15]. Assuming a semidome shape of the liquid gold droplet (due to the surface tension), one would expect a circular cross section of the wire close to the interface with the gold droplet, as depicted at the left portion of 2.1.

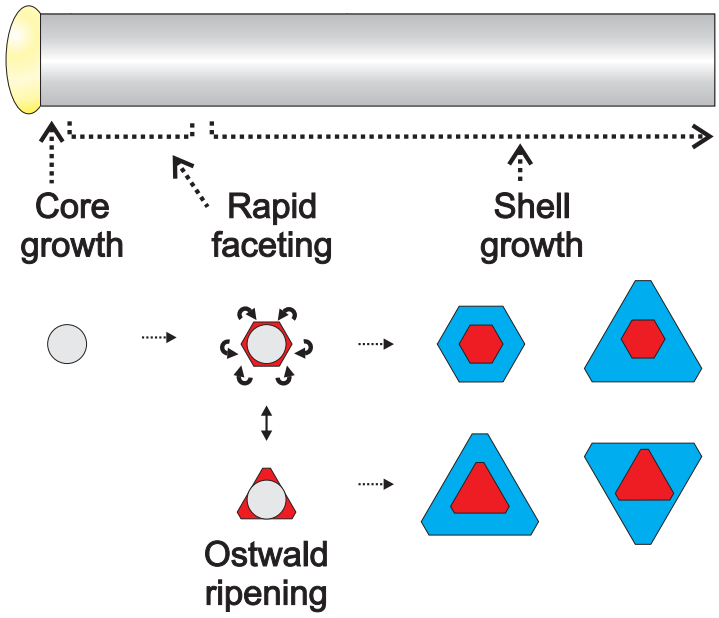

Figure 2.1: Schematic model for facet development on nanowires. A core with a spherical cross section is precipitated directly from the catalyst particle. Within a few seconds after the formation of the core, facets develop by fast lateral growth of the kinked surface. Subsequent shell growth will determine the resulting overall morphology. Alternatively, Ostwald ripening (due to fast surface diffusion) may alter the surface areas of the facets before shell growth initiates. **

However, side view HAADF and tomography studies revealed symmetrically nonequivalent facets at the heterojunction interfaces and at the first 10 nm below the top of the wire, respectively. We explain the formation of a noncircular cross section by rapid faceting of high index sidewall orientations**. This faceting occurs within a few seconds after nanowire precipitation from the catalyst particle (see figure 2.1). After the facet formation, shell growth will determine the overall morphology. Alternatively, Ostwald ripening (specifically observed when using high or low V/III ratios) may alter the surface areas of the facets close to the top of the nanowire before shell growth has initiated. Less stable facets disappear in favor of the more stable facets, since surface diffusion is fast at these length scales and at these temperatures (figure 2.1). In the rest of this paper we refer to the morphology obtained after rapid faceting and possible Ostwald ripening as the core morphology. In the following we discuss the GaP core morphology. GaAs core morphology results are found in reference [21]. In the last section shell growth on the different core morphologies will be investigated. In order to understand the mechanism behind the different nanowire core morphologies, wires grown at different temperatures and precursor flows were characterized. All wires were studied in TEM by tilting it around its long axis. When the wire was viewed along the $[11\bar{2}]$ direction, straight sidewalls running parallel to the long axis of the wire were observed for all growth conditions, in agreement with previous studies [16]. However, when the wire was viewed along the $\langle\bar{1}10\rangle$ direction, a growth parameter dependent morphology was observed. The obtained morphologies are summarized in the structure diagram in figure 2.2a.

At temperatures below 500 °C, the GaP segments show the zinc blende crystal structure, whereas at higher temperatures a mixture of domains with zinc blende and wurtzite are observed. In total, five different types of nanowire morphologies could be discriminated, which are all represented in figure 2.2b and will be discussed separately below: (Type 1). For wires grown at low growth temperatures ($400\,°C < T < 460\,°C$) and low V/III precursor flow ratios (≤ 9), a zigzag pattern of nonparallel facets bounded at the twin boundaries is visible upon viewing along the $\langle\bar{1}10\rangle$ direction [21].

The wire is terminated by $\{111\}$ facets, in accordance with literature [16]. (Type 2). At higher growth temperatures ($460\,°C < T < 530\,°C$) wires with straight edges were observed for both the $\langle\bar{1}10\rangle$ and $\langle11\bar{2}\rangle$ viewing directions (as represented by the high-resolution TEM image [21]). In this case, additional HRTEM imaging of cross-sectional samples showed that the GaP nanowire core has six

** New insights show that the rapid faceting does not take place. As shown for the InP superlattices, in chapter 4, the growth interface directly affects the catalyst particle. This includes that no circular growth interface is formed followed by rapid faceting.

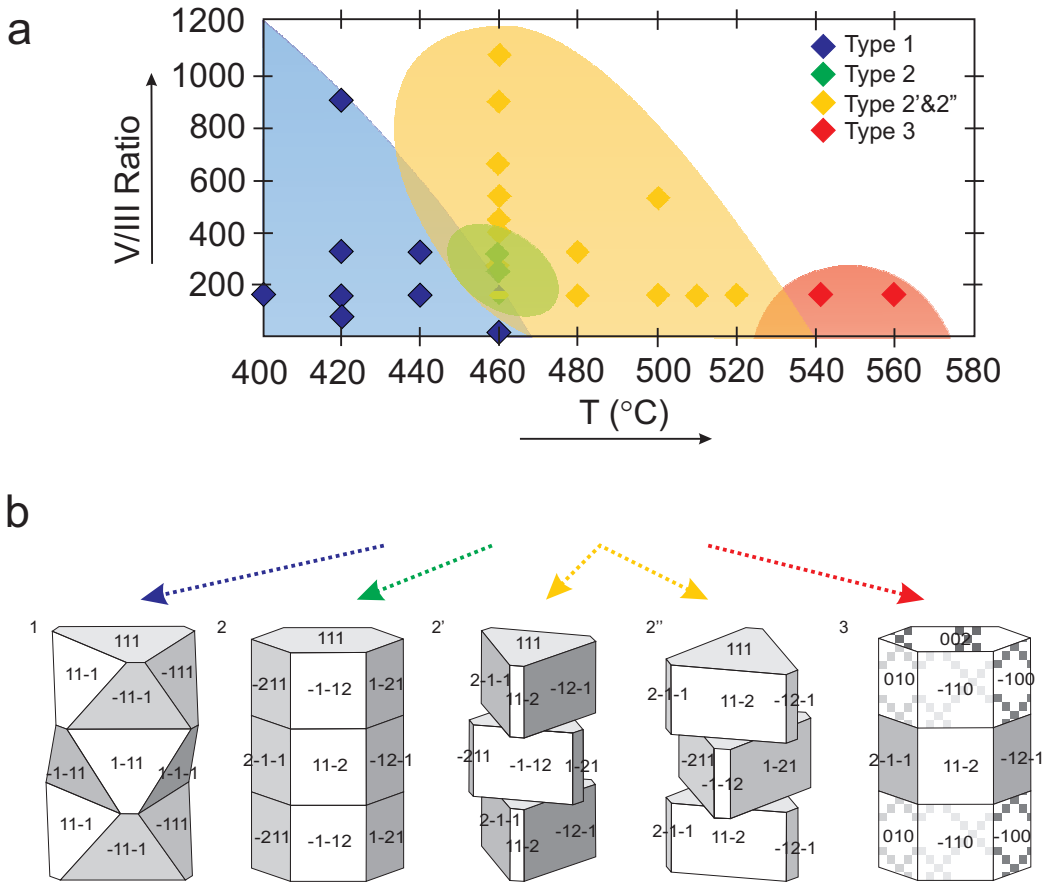

Figure 2.2: GaP core morphologies as a function of temperature and V/III precursor flow ratio. **(a)** For each data point 3-12 wires have been investigated using side view bright field TEM and HAADF imaging along the $\langle 1\bar{1}0 \rangle$ zone axis. The colored areas suggest parameter spaces of the various morphologies. Type 1 represents wires with $\{111\}_A$ and $\{111\}_B$ facets yielding a 3-fold symmetry cross section. Type 2 wires have $\{11\bar{2}\}_A$ and $\{11\bar{2}\}_B$ facets of roughly equal size providing a hexagonal cross section. Type 2' and 2" wires have $\{11\bar{2}\}_A$ and $\{11\bar{2}\}_B$ facets with unequal surface area yielding a 3-fold symmetry cross section. Note that at 460 °C and V/III ratio 163, three different morphologies were observed. Here $\{111\}$ and $\{11\bar{2}\}$ side faceting was observed for low and high PH_3 flows, respectively, indicating that the absolute gas flows determined the morphology. **(b)** Schematic 3D representation of the various VLS GaP core morphologies. Morphology types 1, 2", 2, and 2' represent zinc blende crystal structures, while type 3 shows the morphology of alternating zinc blende and wurtzite segments in high-temperature grown wires (the shaded parts represent the Wurtzite structure). Note that for type 2 and 3 rotational stacking faults do not affect the outer morphology.

$\{11\bar{2}\}$ side facets [15]. This 6-fold symmetry cross section is predominant (see figures 2.2a and 2.2b) only at 460 and 480 °C, and intermediate V/III ratios. (Types 2' and 2"). Interestingly, for higher V/III ratios at 460 °C and at higher growth temperatures (460 °C < T < 530 °C) one of the two types of $\{11\bar{2}\}$ facets becomes more stable, leading to a 3-fold symmetry with three larger and three smaller $\{11\bar{2}\}$ facets. This morphology was confirmed by HAADF imaging upon viewing along the $\langle\bar{1}10\rangle$ direction close to the top. The intensity profiles across the wire were consistent with a 3-fold symmetry shape [21]. The variation in stability of the two types of $\{11\bar{2}\}$ side facets as a function of group V overpressure can be explained by the polar nature of these facets. An increased concentration of active P, induced by the temperature and/or PH_3 flow, will stabilize the P-terminated $\{11\bar{2}\}_B$ facets, resulting in a cross-sectional shape with larger $\{11\bar{2}\}_B$ than $\{11\bar{2}\}_A$ planes. This is consistent with the 6-fold to 3-fold morphology change as a function of temperature. In the temperature regime used for our experiments, the PH_3 pyrolysis in presence of III-V material (in this case the nanowire) increases superlinearly with temperature, [22] which indicates that the V/III ratio is the only parameter that shows a systematic correlation to the morphology changes. This is indicated in figure 2.2b by the two alternatives 2' and 2". (Type 3) In the temperatures range 530 °C < T < 560 °C, the GaP segments contain a mixture of zinc blende and wurtzite domains. Both have 6-fold symmetry and they are bounded by six $\{11\bar{2}\}$ facets (figure 2.2b) and six $\{100\}$ facets, respectively. The facet orientation of the wurtzite segments was deduced from the equivalent orientation in the zinc blende domains.

2.4 Side facets

The morphology determining parameter for the formation of type 1, 2, or 3 is temperature. This can be understood from the temperature dependence of the dominant mechanism for thin film growth: In the temperature range 400-460 °C, sidewall growth is limited by a thermally activated process [15], most likely being the incorporation of growth units at step edges, leading to the formation of flat facets. In this case the most stable facets, being the $\{111\}$ facets, will dominate the growth form. In the temperature range 460-520 °C sidewall growth becomes a diffusion-limited process [15]. Facets parallel to the growth direction are now more likely to develop.

3D TEM tomography images of the bottom part of a nanowire are shown in figure 2.3. The complete dataset of images is available as a movie [21]. The structure encloses a GaP core (first segment grown on the substrate) and a GaAs core

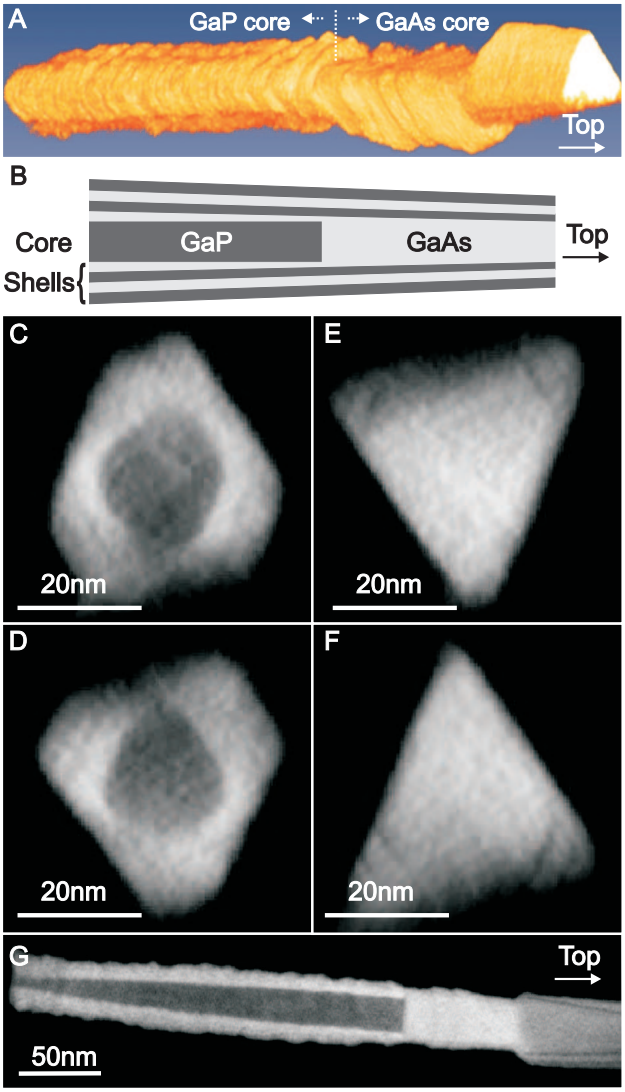

Figure 2.3: Tomography images (a) 3D reconstruction of the morphology of the bottom part of a GaP-GaAs heterostructured nanowire (grown at 480 °C, molar fractions of TMG, PH_3, and AsH_3: 7.3 *10^{-5}, 1.5 *10^{-2}, and 1.5*10^{-2}, respectively). **(b)** Schematic drawing of the part of the heterostructured nanowire shown in **(a)**. Arrows indicate the growth direction. Figures **(c,d)** and **(e,f)** show cross-sectional slices of the two differently oriented twin domains in the GaP-core segment and GaAs segment, respectively. **(g)** Cross-sectional view sliced along the length direction of the wire, displaying the sharp interface between the GaP (dark) and GaAs (light) core segments and the core/shell structure. The GaP core has facets parallel to the long axis while the outer surface of the shell has nonparallel facets. (This sliced view was made with a small inclination with respect to the length direction, yielding the nonrectangular shape of the GaP core on the left.)

(second segment). Two nanometer thick slices through the 3D data set from the GaP core segment are shown in parts c and d of figure 2.3 and from the GaAs core segment in parts e and f of figure 2.3. Examination of successive slices showed that the GaP core is defined by two sets of symmetrically nonequivalent facets differing slightly in surface area, which was confirmed by additional cross-sectional studies on other wires from the same sample. The contrast change as a function of wire diameter shows the presence of a sequence of GaAs and GaP shells, similar to previously observed nanowire cross sections [15, 21]. Thus, the heterostructured nature of the wires enables us to discriminate between morphology induced by axial (core) and radial (shell) growth. While the overall morphology could be obtained from high-resolution scanning electron microscopy (SEM) images [21], this technique does not reveal the inside of the wires as powerfully demonstrated with TEM tomography.

Although the radial growth rate is typically 2 orders of magnitude lower than the axial growth rate, sidewall growth can substantially affect the nanowire outer morphology. Therefore, in addition to tomography characterization both side view and cross-sectional studies were performed for the two most important regimes (types 1 and 2). In side view TEM studies of the wires, the nanowire faceting was studied at different positions along the wire. For the type 1 GaP segments, grown in the kinetically limited regime, no change in morphology as a function of radial overgrowth was observed. Radial growth is continued on the {111} facets formed during axial growth, which is in line with kinetically controlled growth in this temperature regime.

The GaP type 2 core segments terminated by $\{11\bar{2}\}$ facets, grown in the diffusion-limited regime, showed a more complex behavior and developed nonparallel side facets upon additional sidewall growth. This is illustrated by the tomography image in figure 2.3g showing the evolution from a straight GaP core with $\{11\bar{2}\}$ facets to a shell with many nanofacets. The axial outer morphology, as defined by newly emerging facets resulting from mainly GaAs radial overgrowth is strongly dependent on the density of twin boundaries in the wires. For low twin densities and large twin domains, the evolution of parallel $\{11\bar{2}\}$ facets into nonparallel facets implies the appearance of at least two types of subfacets with opposing tilts with respect to the parallel orientation. One of the two sets of $\{11\bar{2}\}$ facets breaks up into {111} and {200} facets, whereas the $\{11\bar{2}\}$ facets of opposite polarity remain flat, introducing the asymmetry in the morphology [21], and previously observed for Si [23] and GaAs [24]. For high twin densities and small twin domains, in the order of a few nanometers in length, 200 facets do not form, and {111} nanofacets bound by twin planes determine the morphology of the former $\{11\bar{2}\}$ facets. The ability to create thin slices from the tomography data (parts

c-f of figure 2.3) allows the visualization of the morphology of individual twin domains, which reveals further complexity in the detailed radial growth behavior. The symmetry of the ⟨111⟩ long axis of the wire and its outer morphology is 3-fold rather than 6-fold, in accordance with the polarity-dependent facet evolution of the polar $\{11\bar{2}\}$ facets.
Strikingly, close inspection of parts c and d of figure 2.3 shows that the nanowire morphology is inversed by radial overgrowth, i.e., the less stable set of $\{11\bar{2}\}$ facets of the GaP core (the facets with smallest surface area) are the more stable ones on the GaAs shell, and vice versa. The observation of growth parameter dependent stability reversal of the two polar $\{11\bar{2}\}$ facets prior to thickening of the nanowires implies an originally cylindrical core shape, since only then both polarities can be formed. On the other hand, for the segment with a GaAs core, no reversal in polarity stability is observed. The explanation can be found in the more efficient pyrolysis of AsH_3 [25] than that of PH_3 [22] at the growth temperatures used. The effectively higher As pressures enable faster incorporation of As growth units on the (Ga-terminated) $\{11\bar{2}\}_A$ facets which decrease in size in favor of the (As-terminated) $\{11\bar{2}\}_B$ facets for core as well as shell growth, similar to reports on mesa growth [26]. For thick enough shells, consisting of mainly GaAs, the $\{11\bar{2}\}_A$ facets grow out completely. Finally, regarding the morphology reversal between GaP core and (mainly GaAs) shell, we have shown that a $\{11\bar{2}\}_A$ faceted GaP core can be obtained using low active P pressures leading to less stable $\{11\bar{2}\}_B$ facets. In contrast, we anticipate that the $\{11\bar{2}\}_B$ facets will become dominant on the GaP core at higher temperatures and high PH_3 overpressures.

2.5 Conclusions

In summary, we have used a powerful TEM tomography technique to reveal the three-dimensional morphology of heterostructured GaP-GaAs nanowires. Importantly, we showed that the faceting of the GaAs and GaP segments is determined by differences in growth kinetics of different crystallographic faces and can be tuned by the temperature and precursor V/III ratio. We demonstrated that low growth temperatures yield nonparallel {111} side facets and high growth temperatures create parallel $\{11\bar{2}\}$ facets. The precursor ratio determines the cross sectional shape of these wires to have either pseudohexagonal or 3-fold symmetry. For GaP nanowires, the relative size of $\{11\bar{2}\}_A$ and $\{11\bar{2}\}_B$ facets appears to be temperature dependent. These results present a fundamental advance in the general understanding of nanowire facet formation and will allow optimizing fabrication conditions for nanowires with smooth surfaces.

2.6 Acknowledgements

This research was carried out under project number MC3.05243 in the framework of the Strategic Research programme of The Netherlands Institute for Metals Research in The Netherlands (www.nimr.nl), the European Marie Curie program, the European FP6 NODE (015783) project, and the ministry of economic affairs of The Netherlands (NanoNed).

References

[1] M. H. Huang, S. Mao, H. Feick, H. Yan, Y. Wu, H. Kind, E. Weber, R. Russo, and P. Yang, "Room-temperature ultraviolet nanowire nanolasers," *Science*, vol. 292, pp. 1897–1899, 2001.

[2] G. F. Zheng, F. Patolsky, Y. Cui, W. U. Wang, and C. M. Lieber, "Multiplexed electrical detection of cancer markers with nanowire sensor arrays," *Nat. Biotechnol.*, vol. 23, pp. 1291–1301, 2005.

[3] M. T. Borgström, V. Zwiller, E. Muller, and A. Imamoglu, "Optically bright quantum dots in single nanowires," *Nano Lett.*, vol. 5, pp. 1439–1443, 2005.

[4] J. A. van Dam, Y. Nazarov, E. P. A. M. Bakkers, S. De Franceschi, and L. P. Kouwenhoven, "Supercurrent reversal in quantum dots," *Nature*, vol. 442, pp. 667–670, 2006.

[5] J. A. van Dam, S. De Franceschi, L. Kouwenhoven, M. Kaiser, M. Verheijen, H. Wondergem, P. van der Sluis, and E. P. A. M. Bakkers, "Epitaxial growth of InP nanowires on germanium," *Nat. Mater.*, vol. 3, pp. 769–773, 2004.

[6] T. I. Kamins, X. Li, and R. S. Williams, "Growth and structure of chemically vapor deposited Ge nanowires on Si substrates.," *Nano Lett.*, vol. 4, pp. 503–506, 2004.

[7] T. Mårtensson, C. Patrik, T. Svensson, B. A. Wacaser, M. W. Larsson, W. Seifert, K. Deppert, A. Gustafsson, R. L. Wallenberg, and L. Samuelson, "Epitaxial III-V nanowires on silicon," *Nano Lett.*, vol. 4, pp. 1987–1990, 2004.

[8] E. P. A. M. Bakkers, M. T. Borgström, and M. A. Verheijen, "Epitaxial growth of III-V nanowires on group IV substrates," *MRS Bull.*, vol. 32, pp. 117–122, 2007.

[9] Y. Li, J. Xiang, F. Qian, S. Gradeak, Y. Wu, H. Yan, D. A. Blom, and C. M. Lieber, "Dopant-Free GaN/AlN/AlGaN Radial Nanowire Heterostructures as High Electron Mobility Transistors," *Nano Lett.*, vol. 6, pp. 1468–1473, 2006.

[10] M. H. M. van Weert, O. Wunnicke, A. L. Roest, T. J. Eijkemans, A. Y. Silov, J. E. M. Haverkort, G. W. 't Hooft, and E. P. A. M. Bakkers, "Large redshift in photoluminescence of p-doped InP nanowires induced by Fermi-level pinning ," *Appl. Phys. Lett.*, vol. 88, p. 043109, 2006.

[11] L. K. van Vugt, S. J. Veen, E. P. A. M. Bakkers, A. L. Roest, and D. Vanmaekelbergh, "Increase of the photoluminescence intensity of InP nanowires by photoassisted surface passivation.," *J. Am. Chem. Soc.*, vol. 127, pp. 12357–12362, 2005.

[12] L. J. Lauhon, M. S. Gudiksen, C. L. Wang, and C. M. Lieber, "Epitaxial core-shell and core-multishell nanowire heterostructures.," *Nature*, vol. 420, pp. 57–61, 2002.

[13] N. Sköld, L. S. Karlsson, M. W. Larsson, M. E. Pistol, W. Seifert, J. Trägårdh, and S. L., "Growth and Optical Properties of Strained GaAs-GaxIn1-xP Core-Shell Nanowires," *Nano Lett.*, vol. 5, pp. 1943–1947, 2005.

[14] H.-Y. Li, O. Wunnicke, M. T. Borgström, W. G., G. Immink, M. W. H. van Weert, M. A. Verheijen, and E. P. A. M. Bakkers, "Remote p-Doping of InAs Nanowires," *Nano Lett.*, vol. 7, pp. 1144–1148, 2007.

[15] M. A. Verheijen, G. Immink, T. de Smet, M. T. Borgstrom, and E. P. A. M. Bakkers, "Growth Kinetics of Heterostructured GaP-GaAs Nanowires.," *J. Am. Chem. Soc.*, vol. 128, pp. 1353–1359, 2006.

[16] J. Johansson, L. S. Karlsson, C. Patrik, T. Svensson, T. Mårtensson, B. A. Wacaser, K. Deppert, L. Samuelson, and W. Seifert, "Structural properties of $(111)_B$-oriented III-V nanowires.," *Nat. Materials*, vol. 5, pp. 574–580, 2006.

[17] B. A. Wacaser, K. Deppert, L. S. Karlsson, L. Samuelson, and W. Seifert, "Growth and characterization of defect free GaAs nanowires.," *J. Cryst. Growth*, vol. 287, pp. 504–508, 2006.

[18] M. C. Plante and R. R. LaPierre, "Growth mechanisms of GaAs nanowires by gas source molecular beam epitaxy.," *J. Crys. Growth*, vol. 286, pp. 394–399, 2006.

[19] A. I. Persson, B. J. Ohlsson, S. Jeppesen, and L. Samuelson, "Growth mechanisms for GaAs nanowires grown in CBE.," *J. Cryst. Growth*, vol. 272, pp. 167–174, 2004.

[20] M. T. Borgström, M. A. Verheijen, G. Immink, T. de Smet, and E. P. A. M. Bakkers, "Interface study on heterostructured GaP-GaAs nanowires.," *Nanotechnology*, vol. 17, pp. 4041–4013, 2006.

[21] M. Verheijen, R. Algra, M. Borgström, G. Immink, E. Sourty, W. van Enckevort, E. Vlieg, and E. Bakkers, "Three dimensional morphology of GaP-GaAs nanowires revealed by transmission electron microscopy tomography.," *Nano Lett.*, vol. 7, pp. 3051–3055, 2007.

[22] C. A. Larsen, N. I. Buchan, and G. B. Stringfellow, "Mass-Spectrometric Studies of Phosphine Pyrolysis and Omvpe Growth of InP.," *J. Cryst. Growth*, vol. 85, pp. 148–153, 1987.

[23] F. M. Ross, J. Tersoff, and M. C. Reuter, "Sawtooth faceting in silicon nanowires.," *Phys. Rev. Lett.*, vol. 95, p. 146104, 2005.

[24] J. Zou, M. Paladugu, H. Wang, G. J. Auchterlonie, Y.-N. Guo, Y. Kim, Q. Gao, H. J. Joyce, H. H. Tan, and C. Jagadish, "Growth mechanism of truncated triangular III-V nanowires.," *Small*, vol. 3, pp. 389–393, 2007.

[25] S. H. Li, C. A. Larsen, and G. B. Stringfellow, "Decomposition Mechanisms of Trimethylarsine.," *J. Cryst. Growth*, vol. 102, pp. 117–125, 1990.

[26] H. Asai, "Anisotropic Lateral Growth in GaAs MOCVD Layers on (001) Substrates.," *J.Cryst. Growth*, vol. 80, pp. 425–433, 1987.

Chapter 3

Paired twins and $\{11\bar{2}\}$ Morphology in GaP nanowires

Rienk E. Algra, Marcel A. Verheijen, Lou-Fé Feiner, George Immink, Ralf Theissmann, Willem J.P. van Enckevort, Elias Vlieg, Erik P.A.M. Bakkers

Formation of random as well as of periodic planar defects can occur during vapor-liquid-solid growth of nanowires with the zinc-blende crystal structure. Here we investigate the formation of pairs of twin planes in GaP nanowires. In such pairs the first twin plane is formed at a random position, rapidly followed by the formation of a second twin plane of which the position is directly related to that of the first one. We show that the triangular $\{11\bar{2}\}$ morphology of the nanowire is a key element in the formation of these twin pairs. We have extended our previous kinetic nucleation model, and show that this describes the development of the nanowire morphology and its relation with the formation of single and paired twin planes.

This chapter has been published in *Nano Letters, vol 10, p. 2349-2356* 2010

3.1 Introduction

Semiconducting nanowires are promising materials for optical and electrical applications. Having control over defects, such as twins, is one of the challenges in nanowire growth. Twins are known to affect the optical and electrical properties of nanowires [1] and can lead to electron scattering at the defect interfaces [2]. Ultimate control over the formation of twins can lead to new designs, such as twin superlattices, which may find applications in (opto-)electronic nanowire devices such as LEDs, lasers, or thermoelectrics [3, 4]. A related aspect is the crystal structure of nanowires, which can be zinc-blende (ZB) or wurtzite (WZ) for III-V semiconducting materials, leading to differences in electrical and optical properties since the band structures of ZB and WZ are different [5, 6]. A twin plane in a ZB wire can be considered as a monolayer of WZ and a stacking fault in WZ as a monolayer of ZB [7, 8]. The presence and distribution of such defect planes can potentially be employed to tailor the band structure of a nanowire consisting of a single material and possibly fabricate homo-junctions. This implies that it is of substantial value to explore and control the mechanism behind the formation of twin planes.

Many parameters affect the development of the planar defects. The formation energies of 'normal' and 'twinned' two-dimensional nuclei at the liquid-solid interface play an important role [9–12], but also the crystal structure and morphology along with the catalyst droplet composition and shape [13]. By controlling the growth conditions, the crystal structure, *i.e.* ZB or WZ, can be influenced as has been shown for InP [13], GaP [14], GaAs [7, 8, 15], and InAs [16, 17], while different side facets and cross-sectional shapes of the nanowire can be obtained [18].

Twin planes have been found to occur *randomly* [19] as well as *periodically* [13, 20] in nanowires. In this paper we show that there is a third mode of occurrence, namely as *'paired'* twin planes. In this case, a first twin plane is formed at a random position (referred to as 'random twin plane'), which is followed by the formation of a second twin plane of which the position is directly related to that of the first one. Twin pairs are in fact present in reported data for GaP [21, 22] and also in other materials systems like GaAs [23–26], but they have not been recognized and analyzed as 'paired twins'. We will show that the morphology of the nanowire and the resulting catalyst droplet distortion dictate the formation of these paired twin planes.

In the following we will first discuss the crystallographic properties of the nanowires and present a detailed structural investigation of the single and paired twins and of the nanowire morphology. Next, we present a kinetic growth model which ex-

plains the relation between the overall nanowire morphology and the occurrence of the single and paired twins. The model is based upon a planar nucleation mechanism in which the shape of the catalyst droplet plays a crucial role, like we proposed before to explain the occurrence of twin superlattices [13].

3.2 Experimental

GaP nanowires were synthesized on oxidised Si substrates in an Aixtron 200 MOVPE reactor, as previously described in reports on nanowire growth kinetics [27] and morphology [18]. Nanowires with paired twin planes are formed between 460 and 500 °C at relatively high PH_3 partial pressures (between 1.5 and 4.5 mbar). Figures 3.1c-e show the three-dimensional morphology, referred to as *type 2* nanowires [18], of a nanowire grown at 460 °C and a partial PH_3 pressure of 1.5 mbar. The morphology is obtained from a tomographic reconstruction of a Scanning TEM/ High Angle Annular Dark Field mode (STEM/HAADF) tilt series acquired over a tilt range of ±76 ° using a Saxton scheme [28, 29].

3.3 Results

3.3.1 Crystal structure and morphology

The nanowire in figure 3.1, which has a diameter of 22 nm at the top, has the zinc-blende crystal structure and the side facets on average correspond to $\{11\bar{2}\}$ planes parallel to the [111] growth direction, as can be recognized from the high resolution TEM images taken along the $\langle 1\bar{1}0\rangle$ zone axis (see figures 3.1a and 3.1f). The tomography images, corresponding to three different viewing angles (figures 3.1c-3.1e), show that the cross-section of the nanowire has a truncated triangular shape [29]. The polarity along the long nanowire axis has been determined by Convergent Beam Electron Diffraction (CBED), which shows that the nanowire top facet corresponds to a $\{111\}_B$ plane [29]. Here the polarity is indexed as "B" for phosphor-terminated facets, whereas "A" stands for gallium-terminated facets. From the crystallographic structure all the other facets can now be indexed. We find that the nanowire morphology is based on opposing broad $\{11\bar{2}\}_A$ side facets and narrow $\{11\bar{2}\}_B$ side facets (see figure 3.4a). Note that on the atomic scale these $\{11\bar{2}\}$ facets are composed of $\{111\}$ and $\{100\}$ nanofacets [23].

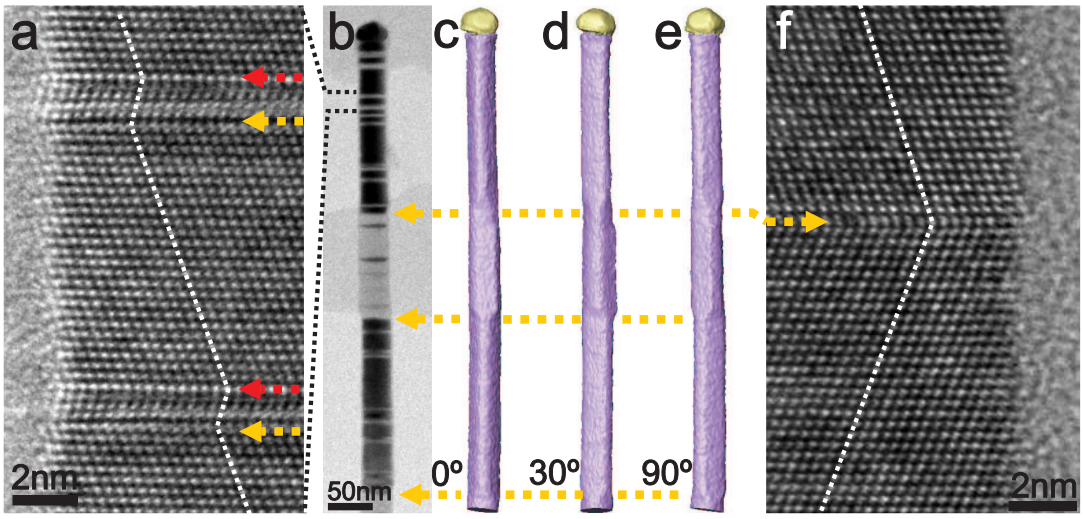

Figure 3.1: TEM images of a multiply twinned GaP nanowire. (a,f). HRTEM micrographs of two paired twin planes **(a)** and one single **(f)** twin plane imaged along the $\langle 1\bar{1}0 \rangle$ zone axis, showing the zinc-blende crystal structure. The first (random) and the second (paired) twin planes are indicated by yellow and red arrows, respectively. **(b).** Bright field TEM image of the nanowire revealing single and paired twins. The transitions in contrast indicate the positions of the twin planes. The bright and dark stripes are short segments between two twins spaced closely together, forming a 'twin pair'. **(c,d,e).** A surface rendering representation of a tomographic reconstruction of a STEM/HAADF tilt series. Three viewing directions are displayed, ranging from parallel to perpendicular to $\{11\bar{2}\}$ side facets. For 0 °, 30 ° and 90 ° this results in the $[11\bar{2}]$, $[01\bar{1}]$, and $[\bar{1}10]$ viewing directions, respectively. Clearly, the single twins induce 180 ° rotations of the truncated triangular cross-section, whereas in the regime of twin pairs the overall morphology remains unchanged.

3.3.2 Twinning

In the bright field TEM image shown in figure 3.1b, one observes a large number of twin planes in the nanowire: each change in contrast corresponds to the position of a twin plane. Such a twin plane can be formed because the formation energy of a twinned layer in GaP is only slightly higher than that of a normal, untwinned, layer (the interfacial energy associated with a twin plane, γ_T, is estimated at 20 mJ m^{-2} [30]). At a twin plane the crystal lattice is rotated by 180 ° (or equivalently 60 °) around the long [111] axis of the nanowire, as demonstrated by the HRTEM images in figures 3.1a and f.

Occasionally a twin plane occurs in an isolated position, i.e. without another one present in its immediate vicinity. These *single* twin planes (indicated by the

yellow arrows in figure 3.1b) separate relatively long nanowire sections of opposite crystal orientation, as the high resolution TEM micrograph of figure 3.1f shows, which are clearly visible as the alternating bright and dark sections in the bright-field image (figure 3.1b). This alternation in crystal orientation is in perfect correspondence with an alternation of the shape of the nanowire cross-section between two inverted truncated triangles, as comparison between figure 3.1b and figures 3.1c-e shows. It is important to note that, while the crystal orientation changes abruptly at the twin plane, the cross-sectional shape changes gradually and thus full inversion of the cross section is reached only at a certain distance from the twin plane, *i.e.* after an 'inversion length' L_{inv} which accommodates the shape change.
At many positions within such a long section a change of contrast occurs, visible as a thin stripe in figure 3.1b, which does not correspond to an inversion of the truncated triangular shape. These stripes represent short segments between two twin planes in close proximity, which we define as a twin *pair*. The high resolution TEM micrograph of figure 3.1a shows two such twin pairs in detail, demonstrating that the crystal orientation inside the segment is opposite to that outside. Along the nanowire, we find an average single twin density of approximately 1 μm^{-1}, and a twin pair density of 20 μm^{-1}. The spacing between single twins and twin pairs and between neighboring twin pairs varies widely, which indicates that the occurrence of a first twin plane (*i.e.* a single twin or the first twin plane of a twin pair) is a random event.

3.3.3 Faceting

After the formation of a first (random) twin plane, side facets develop which are not parallel to the growth direction. These side facets have been identified from the reconstructed tomogram and HRTEM (figure 3.2) images taken from a 100 nm diameter GaP nanowire, where the facets are more pronounced than on the smaller diameter nanowires. The HRTEM images (figures 3.2a and 3.2c) are acquired from the same twin pair, and show opposing nanowire side facets. We find that both facets after the first (bottom) twin plane make an angle $\theta \approx 19.5\,^\circ$ with respect to the nanowire growth direction (white arrow), showing that these are {111} facets. Note that the two sides of the nanowire evolve in a different fashion after the formation of the second twin plane [29]. A detailed schematic representation of the side facets is given in figure 3.2d. Upon passing the twin pair the narrow side facets evolve from $\{11\bar{2}\}_B$ via $\{111\}_A$ followed by $\{111\}_B$ back towards $\{11\bar{2}\}_B$, while the broad side facets show a change from $\{11\bar{2}\}_A$ via $\{111\}_B$ back towards $\{11\bar{2}\}_A$. Directly after the second twin the latter $\{11\bar{2}\}_A$

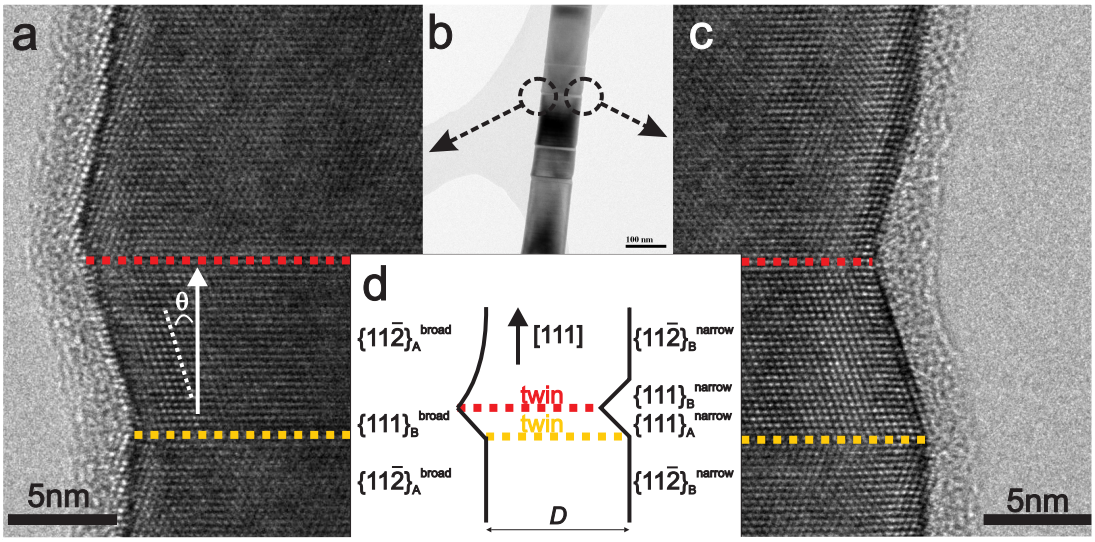

Figure 3.2: Faceting related to the paired twins. (b). Overview TEM image of a 100 nm diameter GaP nanowire. **(a,c)**. HRTEM images acquired along the $\langle 01\bar{1} \rangle$ zone axis revealing the orientation of the side facets and the evolution of different side facets by passing paired twins. **(d)**. Schematic representation of the different facets. The angles between the different facets are exaggerated in order to clearly show the differences. One side of the wire comprises broad facets, whereas the opposite facets are narrow.

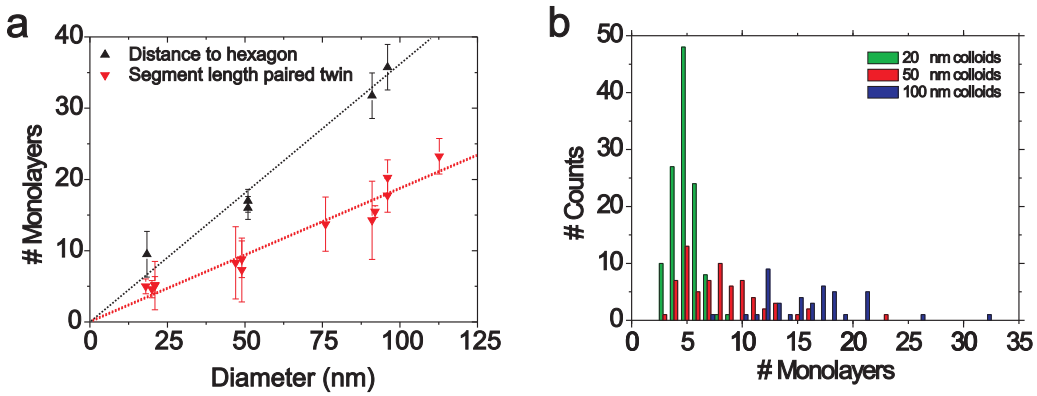

Figure 3.3: Monolayers (a). Number of monolayers, N_p, between paired twin planes (pair length; red triangles) versus nanowire diameter D. Each data point gives the average value of the pair length determined from at least 20 twin pairs within one wire. Also shown is half the number of monolayers, $N_{inv}/2$, of a {111}-side-faceted segment initiated by a single twin plane (inversion length; black triangles). **(b)**. Histograms showing the distribution of pair lengths for three different nanowire diameters.

facet is not straight, since the ratio of the $\{111\}_A$ and $\{100\}_A$ nanofacets is not exactly 2/1 here, but somewhat larger, so that the slightly increased wire diameter gets reduced again to its original value [29].

3.3.4 Length scales

From HRTEM we determined (half) the inversion length, L_{inv}, by counting the number of monolayers, N_{inv}, comprising the {111}-side-faceted segment after the formation of a single twin (strictly, $L_{inv} = N_{inv}\ h$, where h is the layer thickness), and the results are plotted versus the nanowire diameter D in figure 3.3a. One sees that the inversion length scales accurately with the nanowire diameter, which implies that the cross-sectional shape of the $\{11\bar{2}\}$ sections is independent of D. Thus, within the accuracy of the experimental analysis, this shape is identical for all nanowires investigated , a result that might have been expected but is not self-evident. The number of monolayers, N_p, between the two twin planes that make up a twin pair has been determined from HRTEM too, and the results are presented in figure 3.3a as well. This *'pair length'* (strictly, the pair length is $L_p = N_p h$) is also seen to increase linearly with increasing nanowire diameter, while the pair-length distribution becomes broader with diameter as shown in figure 3.3b. The fact that the pair length is not constant but scales with the nanowire diameter D, indicates that the occurrence of the second twin plane is not caused by some physical interaction, like a strain field, with the first twin plane, but is induced by the evolution of the wire shape initiated by the occurrence of the first twin. The identical scaling behavior of pair length and inversion length with D (the characteristic length scale of the nanowire) indicates that both morphology and occurrence of twins are governed entirely by the nanowire geometry. This suggests that the mechanism responsible for the present growth mode producing single twins and twin pairs is essentially the same as the one responsible for producing twin superlattices [13] under different growth conditions, while the different outcome (twin pairs instead of a twin superlattice) is related to the different overall nanowire morphology ($\{11\bar{2}\}$ instead of {111}).

3.4 Kinetic growth model

The above observations are summarized in the schematic of the nanowire morphology given in figure 3.4a, highlighting the single twins and twin pairs. The evolution of this morphology can be described as resulting from two growth modes which produce vertical $\{11\bar{2}\}$ and tilted {111} side facets, respectively. The dominant $\{11\bar{2}\}$ growth mode preserves the truncated triangular cross-sectional shape

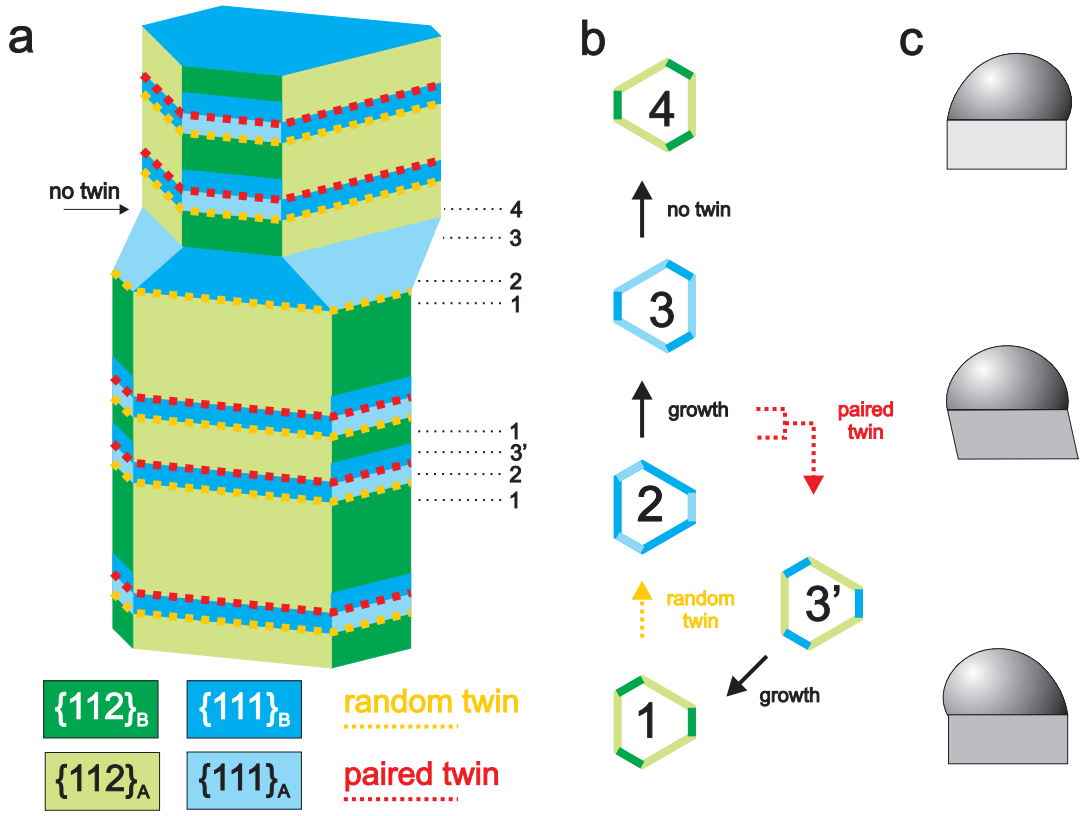

Figure 3.4: Schematic representation of the nanowire morphology (a) containing random (dashed yellow lines) and paired (dashed red lines) twins. A 'single twin' consists of only a randomly formed twin, whereas the twin pairs are a combination of a first random twin, followed by a second 'paired' twin. The polarity of the facets is given by dark- and light-green for $\{11\bar{2}\}_B$ and $\{11\bar{2}\}_A$ facets, respectively. Similarly, dark- and light-blue indicate the $\{111\}_B$ and $\{111\}_A$ facets. Note that the change from $\{111\}$ to $\{11\bar{2}\}$ after a single twin takes place *without* the formation of a second twin. **(b)**. Dynamics of twin formation in relation to the nanowire morphology. The green and blue contour lines represent $\{11\bar{2}\}$ and $\{111\}$ side facets, respectively, as in **(a)**. The route from stage 1 to stage 4 via 2 and 3 describes the formation of a random single twin followed by evolving $\{111\}$ facets towards the opposite truncated triangular morphology bounded by $\{11\bar{2}\}$ facets. The route from stage 1 via 2 and 3' returning to stage 1 describes the formation of a paired twin. Here, first $\{111\}$ facets are formed following the first twin plane. After the second twin plane the $\{111\}_A$ side facets get inverted whereas the $\{111\}_B$ side facets are turned into $\{100\}_A$ facets, and finally the original $\{11\bar{2}\}$ morphology is restored after a further stretch of growth. The different stages 1 to 4 are also indicated in **(a)**. **(c)**. Shape of the catalyst metal droplet at stage 1, halfway between 2 and 3, and at stage 4.

of the nanowire with $\{11\bar{2}\}$ side facets (stage 1). When a random twin is formed, growth switches to the $\{111\}$ mode (stage 2), and now two different routes can be followed, as illustrated in figure 3.4b: a single-twin route and a paired-twin route. In the single-twin route the growth continues in this $\{111\}$ mode until the triangular cross-sectional shape has inverted (stage 3) and growth switches back to the $\{11\bar{2}\}$ mode (stage 4). In the paired-twin route the $\{111\}$-mode growth is interrupted soon by the formation of a second twin plane, which switches growth at the narrow side facets to the $\{111\}$ growth mode with opposite crystal orientation and facet tilt angle, and at the broad side facets to the $\{11\bar{2}\}$ mode (stage 3'). This growth mode takes the cross section back to its original triangular cross-sectional shape, where growth switches to the $\{11\bar{2}\}$ mode also at the narrow side edges (stage 1). In the following we will show that the above growth scenario can be explained semiquantitatively by a kinetic growth model based upon two-dimensional edge nucleation which takes full account of the response of the shape of the catalyst droplet to the shape of the nanowire cross section. It is an extended version of the model, based upon the same mechanism, we proposed to explain the occurrence of twin superlattices [13].

3.4.1 Growth mechanism

VLS nanowire growth is characterized by the presence of a liquid droplet which is in contact with the nanowire top facet. Growth proceeds via a layer-by-layer process, starting with the formation of a two-dimensional nucleus at one of the edges of the nanowire-droplet interface, followed by rapid lateral growth of the layer [11–13]. Addition of a layer with a specific crystal orientation and specific external facets thus requires that an edge nucleus is formed with corresponding crystal orientation and corresponding outer (solid-vapour) facet. The free energy of formation, ΔG^*_{XY}, of an edge nucleus formed at nanowire side facet X, depends on the contact angle δ_{XY} of the liquid catalyst droplet with respect to the outer facet Y, with tilt angle θ_Y, of the nucleus (see figure 3.5a), according to [11–13, 31],

$$\Delta G^*_{XY} = bh\left\{\frac{[(1-\alpha)\gamma_{SL} + (\alpha/\cos\theta_Y)(\gamma_{SV} - \gamma_{LV}\cos\delta_{XY})]^2}{[\Delta\mu - \gamma_{nN}/h]}\right\} \tag{3.1}$$

where γ_{SL} , γ_{SV} , and γ_{LV} are the solid-liquid, solid-vapour, and liquid-vapour surface energies, γ_{nN} is the interface energy between nucleus and nanowire which is equal to the twinning energy γ_T for a nucleus inducing a twin plane and is zero otherwise, $\Delta\mu$ is the supersaturation (difference in chemical potential per unit

volume between liquid and solid), α is the fraction of the perimeter of the nucleus which is in contact with the vapor and b is a geometrical constant (for a hexagonal nucleus α=1/6 and b=2$\sqrt{3}$≈3.46). The crucial point is that the droplet contact angles at the various nanowire side facets depend on the shape of the (droplet-nanowire) growth interface. When the shape of the growth interface changes (see figure 3.5b) the droplet distorts, in order to minimize its surface energy. We have found [13] that the contact angles, which characterize the droplet distortion, depend linearly on the interface deformation, ϕ (for definition, see figure 3.5b) *viz.* $\delta_{XY}(\phi) = \delta_{XY}(0) \pm \phi$. In turn ϕ changes during growth (see figures 3.5a-b), viz. upon addition of each monolayer tan(ϕ) changes by $4h$ tan(θ_Y)/aD, where a is a geometrical constant, a=1.10 [32]. Specifically, the contact angle is smaller at the narrow side facet edges than at the broad side facet edges, *i.e.* the droplet leans over at the broad edges, as illustrated in figure 3.4c.

3.4.2 Nucleation probabilities

The probability of formation for each type of nucleus, p_{XY}, in general obeys

$$p_{XY}(\phi) \propto exp\left[\frac{-\Delta G^*_{XY}(\phi)}{k_B T}\right] \tag{3.2}$$

So the probability depends on the shape of the growth interface and therefore changes slowly during growth when the interface shape evolves, as occurs when the side facets are not parallel to the growth direction. Quite generally, this leads to a competition between several different nuclei. The gradual evolution of the various probabilities explains why the nanowire may switch between different types of side facets during growth. To appreciate this competitive layer-by-layer growth process one should keep in mind that each probability $p_{XY}(\phi)$ reaches its maximum value when $\delta_{XY}(\phi) = 0$ [see equation 3.1], *i.e.* when the droplet surface is tangent to the outer facet of the nucleus. In addition the formation of a nucleus which induces a twin plane costs an extra twin energy, γ_T, which increases ΔG^*_{XY} [see equation 3.1], leading to an overall reduction of the associated probability. Combining equations 3.1 and 3.2 we have calculated, after proper normalization, exactly like in ref. [13], the formation probabilities of the potentially relevant nuclei as a function of the deformation ϕ of the nanowire-droplet interface. The results for a plausible set of parameters for GaP are shown in figure 3.5c, which we will use extensively in the discussion below.

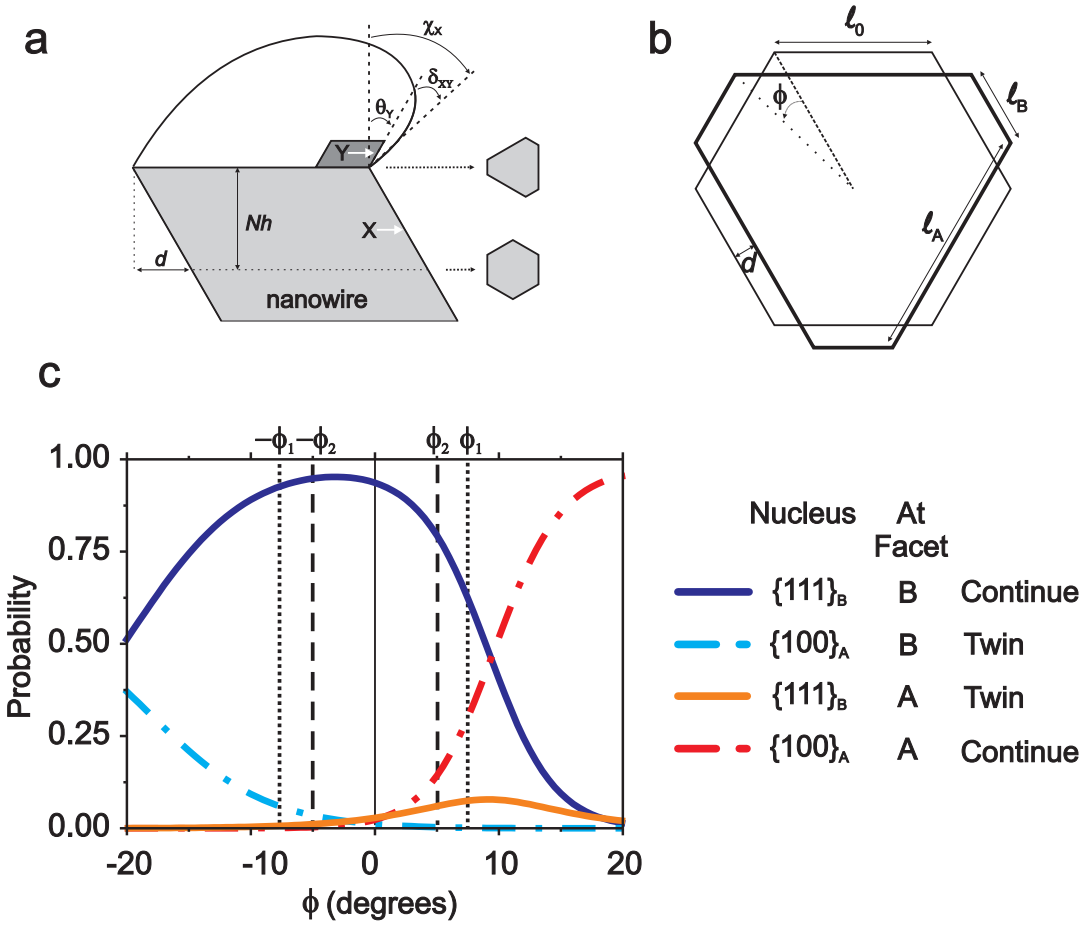

Figure 3.5: Geometries and probabilities(a). Geometry of the VLS wire growth (side view), defining the edge displacement d, the nanowire height Nh measured from the hexagonal cross-sectional shape, the droplet contact angle χ_X and the facet tilt angle θ_Y, both with respect to the growth direction. The difference between the droplet contact angle and the facet tilt angle is given by δ_{XY}, *i.e.* $\delta_{XY}(\phi\ ) = \chi_X(\phi\ )\ \theta_Y$. **(b)**. Geometry of the growth interface (top view), showing the edge length l_0 of the hexagon, the widths l_A (l_B) of the A-terminated (B-terminated) nanowire side facets, and the deformation angle ϕ defined by $\sqrt{3}\ \tan(\phi)\ 2\sqrt{3}\ d\ /\ l_0 = (l_A\ l_B)\ /\ (l_A\ l_B)$. **(c)**. Probabilities for the four dominant nucleation processes versus the deformation ϕ of the droplet-nanowire interface (for clarity the small nonzero probabilities for two more nucleation processes are not shown). Under "At facet" is indicated the termination of the nanowire side facet at which the nucleation takes place (the side-facet orientation is not mentioned, since the probabilities do not depend on it). The legend indicates explicitly which processes induce a twin plane and change the nanowire side facet ("Twin") and which do not but lead to continuation of the side facet ("Continue"). Parameter values [33]

3.4.3 $\{11\bar{2}\}$ Morphology

We start by considering that part of a long section where the nanowire has three narrow $\{11\bar{2}\}_B$ side facets (composed on average of two $\{111\}_B$ and one $\{100\}_B$ nano-facets) and three broad $\{11\bar{2}\}_A$ side facets (built from two $\{111\}_A$ and one $\{100\}_A$ nano-facets) as shown at stage 1 in figure 3.4a and b. The droplet leans over towards the broad $\{11\bar{2}\}_A$ edges (see figure 3.4c) and this distortion, which corresponds to positive ϕ , favours two nucleation processes: formation of a $\{111\}_B$-nucleus on the narrow B side of the nanowire and formation of a $\{100\}_A$-nucleus on the broad A side (see figure 3.5c). Neither of these processes involves the creation of a twin plane. (Here $\{hkl\}_Y$-nucleus denotes a nucleus with an outer (nucleus-vapour) Y-terminated $\{hkl\}$-facet.) For a certain amount of distortion (corresponding to $\phi_1 \approx 8\,^\circ$ in figure 3.5c, indicated by the thin dashed line) the ratio of the formation probabilities of these two nuclei is 2/1, which results in the formation of overall $\{11\bar{2}\}$ facets if we assume that a layer resulting from a $\{111\}_B$-nucleus ($\{100\}_A$-nucleus) is terminated on the opposite side by the complementary $\{111\}_A$ facet ($\{100\}_B$ facet). Because these $\{11\bar{2}\}$ facets are parallel to the growth direction the shape of the nanowire cross-section remains constant. Note that if the ratio deviates temporarily from 2/1 because of fluctuations, *e.g.* such that an excess of $\{111\}_B$-nuclei is formed, the interface deformation ϕ increases. This reduces the probability for further $\{111\}_B$-nucleation and enhances that for $\{100\}_A$-nucleation, and consequently the system tends to be driven back towards ϕ_1 . Similarly, a surplus of layers initiated from a $\{100\}_A$-nucleus makes ϕ decrease, thus changes the probabilities in the opposite direction, and also drives the system back towards ϕ_1 . In this way the interface deformation is *dynamically stabilized* at ϕ_1 , such that $\{11\bar{2}\}$ faceted growth continues and stage 1 is preserved.

3.5 Twinning

Such stationary nanowire growth with broad $\{11\bar{2}\}_A$ and narrow $\{11\bar{2}\}_B$ side facets is interrupted by formation of a twin plane when a $\{111\}_B$-nucleus is formed at a $\{11\bar{2}\}_A$ side facet at a random position along the nanowire. As figure 3.5c shows (orange curve), there is a small but finite probability for this process for positive ϕ , because the cost in twin energy is then partly compensated by the contact angle δ_{AB} being comparably small. Note that the probability for side facet continuation (*i.e.* for a twin plane *not* being formed) is given by the sum of the probabilities for $\{111\}_B$-nucleus formation at a B-terminated side facet (dark-blue curve) and that for $\{100\}_A$-nucleus formation at an A-terminated side

facet (dot-dashed red curve). Close to ϕ_1 the value calculated for the probability for twinning is ≈ 0.075, in good agreement with the observed twin density of 20 μm^{-1}, which amounts to a twinning probability of ≈ 0.063. Upon twinning the deformation parameter ϕ switches from $+\phi_1$ to $-\phi_1$ (the droplet shape is left unchanged, as it is tied to the shape of the nanowire cross-section, but the nanowire side facets change). After twin formation, $\{111\}$ side facets begin to develop, depicted in figure 3.4b by the blue contour (situation 2), with the $\{111\}_B$ facets initially being broad and the $\{111\}_A$ facets being narrow. From here on growth can proceed via the two different routes mentioned above, resulting in a *single* twin or a *twin pair*, respectively.

3.5.1 Single twin formation

In the first route, after formation of a twin, all layers start from a $\{111\}_B$- nucleus at a $\{111\}_B$ side facet of the nanowire, which at negative ϕ has the largest probability to be formed (see figure 3.5c). Thus continuous $\{111\}$ side facets develop, and because of their inclined orientation with respect to the growth direction, the nanowire cross-section evolves towards the opposite truncated triangular shape (situation 3 in figure 3.4b). This evolution is described by ϕ increasing gradually from $-\phi_1$ to $+\phi_1$, passing the hexagonal shape (*i.e.* $\phi = 0$) when halfway [13]. In other words, the droplet distortion first decreases, reaching its minimum at the hexagonal cross-sectional shape, and then increases again, but now with the droplet leaning over to the opposite edges, as illustrated in figure 3.4c. When ϕ approaches ϕ_1 the probability for formation of a $\{100\}_A$-nucleus at a, now broad, $\{111\}_A$ side facet begins to increase, while that for a $\{111\}_B$-nucleus at the narrowing $\{111\}_B$ side facets decreases (see figure 3.5c). At ϕ_1 the probability ratio for these two nucleation processes reaches 2/1, and overall $\{11\bar{2}\}$ side facets are again being formed instead of $\{111\}$ side facets. So the morphology changes at ϕ_1 , *without* creation of a second twin plane, towards a $\{11\bar{2}\}$ morphology (stage 4). This is the mirror image and thus symmetrically equivalent to that of stage 1. The complete process (from stages 1 to 4) represents the formation of a single twin.

3.5.2 Paired twin formation

In the second, far more frequent route, the development of the $\{111\}$ side facets is interrupted already well before the growth-interface attains a hexagonal shape, i.e. the interruption occurs at a deformation $-\phi_2$ with $-\phi_1 < -\phi_2 < 0$ (see figure 3.5c and figure 3.6). The interruption is caused by a $\{100\}_A$-nucleus being

formed at a $\{111\}_B$ side facet, inducing a (second) twin plane. This nucleation process (dot-dashed blue curve in figure 3.5c) has a sizeable probability when the droplet leans over sufficiently towards the broad $\{111\}_B$ side facets (*i.e.* when ϕ is sufficiently negative), such that the contact angle δ_{BA} is not too large. However, this probability decreases rapidly when ϕ approaches 0 (figure 3.5c) because δ_{BA} increases, as shown in figure 3.6c and d. As a result the second, paired, twin is formed within a limited number of layers after the formation of a random twin plane and always before the interface shape is hexagonal (or else the growth continues to stage 4 in figure 3.4 via the first route, as described above).

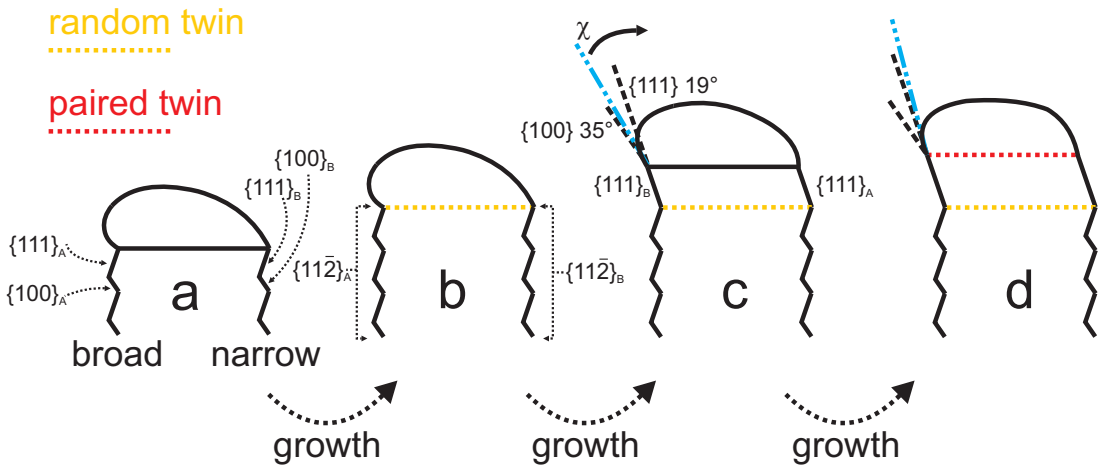

Figure 3.6: Paired twin evolution Schematic representation of the formation of paired twins in combination with the droplet shape. **(a)** Growth of $\{11\bar{2}\}$ facets, composed of $\{111\}$ and $\{100\}$ subfacets. **(b)** Formation of a random twin plane indicated by the yellow dotted line. The shape of the droplet does not change and remains distorted towards what was the broad $\{11\bar{2}\}_A$ side facet and now becomes the (broad) $\{111\}_B$ side facet. **(c)** After the formation of the random twin, $\{111\}$ facets are formed. The development of the $\{111\}$ facets reduces the distortion of the droplet, which evolves towards a more hemispherical shape. This changes the contact angles with respect to the various facet planes, *e.g.* $\{100\}_A$ at 35 ° and $\{111\}$B at 19 °, whereby the nucleation probabilities change. **(d)** Formation of the second, paired, twin plane, indicated by the red dotted line, at deformation -ϕ_2<0, *i.e.* before the growth interface has become hexagonal.

The formation of the second twin plane corresponds to a switch from $-\phi_2$ to $+\phi_2$ and initiates the development of broad $\{11\bar{2}\}_A$ and narrow $\{111\}_B$ side facets (stage 3' in figure 3.4b). This is mainly driven by the highly probable formation of $\{111\}_B$-nuclei at the narrowing $\{111\}_B$ side facets and less probable formation of $\{100\}_A$-nuclei at the broadening $\{11\bar{2}\}_A$ side facets (see figure 3.5c). As in the

first route, the ratio of the probabilities for these two nucleation processes (B/A) decreases as growth progresses and ϕ increases. When ϕ reaches ϕ_1 , the ratio again is 2/1, and the $\{111\}_B$ side facets have changed into $\{11\bar{2}\}_B$ side facets. So, without creation of a further twin plane the nanowire has returned towards a $\{11\bar{2}\}$ morphology (stage 1 in figure 3.4b).

3.5.3 Length scales

We have seen that, according to the model, overall $\{11\bar{2}\}$ side facets can only exist at the unique deformation ϕ_1 (the value of which depends of course on growth conditions) where the two relevant nucleation rates are in the ration 2 to 1. Because of the geometrical relation $\phi \propto Nh/D$ [32] this explains immediately our observation that the inversion length scales with nanowire diameter, *viz.* $N_{inv} = 2N_1 \propto 2\phi_1 D/h$. Further, formation of the second twin plane of a twin pair should take place at a deformation with well-defined average value, ϕ_2 , and standard deviation, both determined by the probability for formation of a $\{100\}_A$-nucleus at a $\{111\}_B$ side facet. It follows that $N_p = N_1 - N_2 \propto (\phi_1 - \phi_2)\ D/h$, which explains the observed linear dependence of the pair length on nanowire diameter. The actual values of the two characteristic deformation parameters, as determined from the slopes in figure 3.3a, are $\phi_1 \approx 8^\circ$ and $\phi_2 \approx 4^\circ$, in reasonable agreement with the values obtained from the growth model, *viz.* $\phi_1 \approx 8^\circ$ and $\phi_2 \approx 5^\circ$ (figure 3.5c). However, the model does not describe properly the relatively narrow distribution of pair lengths seen experimentally (figure 3.3b), as the probability involved (dot-dashed blue curve in figure 3.5c) decreases monotonously in the relevant range of ϕ instead of having a pronounced maximum.

3.6 Conclusions

We conclude that the present edge nucleation model explains (i) the occurrence of the truncated triangularly shaped $\{11\bar{2}\}$ morphology as being due to a dynamic stability resulting from competition between $\{100\}_A$- and $\{111\}_B$-nuclei, (ii) the occurrence of both single twins and twin pairs and the associated morphologies, (iii) the scaling of the inversion length and, more significantly, the pair length with nanowire diameter. We point out that all relevant nucleation processes involve either a $\{100\}_A$-nucleus or a $\{111\}_B$-nucleus. This implies that under the present growth conditions (fairly high temperature and V/III ratio) leading to *type 2* nanowires, apparently the effective solid-liquid surface energies $\gamma_{SL}/\cos\theta$ of the $\{100\}_A$ and $\{111\}_B$ surfaces are sufficiently close to make the relevant free energies of formation ΔG^*_{XY} comparable. This is to be contrasted with the

situation in *type 1* nanowires [18], which may contain a twin superlattice [13, 20] or random single twin planes [19], where only $\{111\}_B$-nuclei occur [13].

3.7 Acknowledgements

This research was carried out under project number MC3.05243 in the framework of the strategic research program of the Materials Innovation Institute (M2i) (www.M2i.nl), the former Netherlands Institute of Metals Research, the FP6 NODE (015783) project, the Ministry of Economic Affairs in the Netherlands (NanoNed) and the European Marie Curie program. The authors thank H. de Barse for SEM imaging. CBED investigations were done at the Tecnai F20 G ST of the Nanostrukturtechnik group at the University of Duisburg-Essen. Correspondence and requests for materials should be addressed to E.P.A.M. Bakkers.

References

[1] J. Bao, D. Bell, F. Capasso, J. Wagner, T. Mårtensson, J. Trägårdh, and L. Samuelson, "Optical properties of rotationally twinned InP nanowire heterostructures," *Nano Lett.*, vol. 8, pp. 836–841, 2008.

[2] Z. Ikonic, G. P. Srivastava, and J. C. Inkson, "Optical properties of twinning superlattices in diamond-type and zinc-blende-type semiconductors.," *Phys. Rev. B*, vol. 52, pp. 14078–14085, 1995.

[3] A. Hochbaum, R. Chen, R. Delgado, W. Liang, E. Garnett, M. Najarian, A. Majumdar, and P. Yang, "Enhanced thermoelectric performance of rough silicon nanowires," *Nature*, vol. 451, pp. 163–168, 2008.

[4] A. Boukai, Y. Bunimovich, J. Tahir-Kheli, J.-K. Yu, W. Goddard, and J. Heath, "Silicon nanowires as efficient thermoelectric materials," *Nature*, vol. 451, pp. 168–171, 2008.

[5] K. Pemasiri, M. Montazeri, R. Gass, L. Smith, H. Jackson, J. Yarrison-Rice, S. Paiman, Q. Gao, H. Tan, C. Jagadish, X. Zhang, and J. Zou, "Carrier dynamics and quantum confinement in type II ZB-WZ InP nanowire homostructures," *Nano Lett.*, vol. 9, pp. 648–654, 2009.

[6] M. Mattila, T. Hakkarainen, M. Mulot, and H. Lipsanen, "Crystal-structure-dependent photoluminescence from InP nanowires.," *Nanotechnology*, vol. 17, pp. 1580–1583, 2006.

[7] K. Hiruma, M. Yazawa, T. Katsuyama, K. Ogawa, K. Haraguchi, M. Koguchi, and H. Kakibayashi, "Growth and optical properties of nanometer scale GaAs and InAs whiskers.," *J. Appl. Phys.*, vol. 77, pp. 447–462, 1995.

[8] P. Mohseni, C. Maunders, G. Botton, and R. LaPierre, "GaP/GaAsP/GaP core- multishell nanowire heterostructures on (111) silicon," *Nanotechnology*, vol. 18, p. 445302, 2007.

[9] T. Akiyama, K. Sano, K. Nakamura, and T. Ito, "An Empirical Potential Approach to Wurtzite-Zinc-Blende Polytypismin Group III-V Semiconductor Nanowires," *J. Appl.Phys.*, vol. 45, pp. L275–278, 2006.

[10] D. Hurle, "A mechanism for twin formation during Czochralski and encapsulated vertical Bridgman growth of III-V compound semiconductors.," *J. Cryst. Growth*, vol. 147, pp. 239–250, 1995.

[11] F. Glas, J. Harmand, and G. Patriarche, "Why does Wurtzite form in nanowires of III-V Zinc Blende semiconductors? ," *Phys. Rev. Lett.*, vol. 99, p. 146101, 2007.

[12] V. Dubrovskii, N. Sibirev, J. Harmand, and F. Glas, "Growth kinetics and crystal structure of semiconductor nanowires," *Phys. Rev. B*, vol. 78, pp. 235301–1–10, 2008.

[13] R. Algra, M. Verheijen, M. Borgström, L. Feiner, G. Immink, W. van Enckevort, E.Vlieg, and E. Bakkers, "Twinning superlattices in indium phosphide nanowires," *Nature*, vol. 456, pp. 369–372, 2008.

[14] J. Johansson, L. Karlsson, K. Dick, J. Bolisson, B. Wacaser, K. Deppert, and L. Samuelson, "Effects of supersaturation on the crystal structure of gold seeded III-V nanowires," *Crystal Growth & Design*, vol. 9, pp. 766–773, 2009.

[15] G. Patriarche, F. Glas, M. Tchernycheva, C. Sartel, L. Largeau, J.-C. Harmand, and G. Cirlin, "Wurtzite to Zinc Blende Phase Transition in GaAs Nanowires Induced by Epitaxial Burying," *Nano Lett.*, vol. 8, pp. 1638–1643, 2008.

[16] M. T. Borgström, M. A. Verheijen, G. Immink, T. de Smet, and E. P. A. M. Bakkers, "Interface study on heterostructured GaP-GaAs nanowires.," *Nanotechnology*, vol. 17, pp. 4041–4013, 2006.

[17] S. Dayeh, E. Yu, and D. Wang, "Surface diffusion and substrate-nanowire adatom exchange in InAs nanowire growth," *Nano Letters*, vol. 9, pp. 1967–1972, 2009.

[18] M. Verheijen, R. Algra, M. Borgström, G. Immink, E. Sourty, W. van Enckevort, E. Vlieg, and E. Bakkers, "Three dimensional morphology of GaP-GaAs nanowires revealed by transmission electron microscopy tomography.," *Nano Lett.*, vol. 7, pp. 3051–3055, 2007.

[19] J. Johansson, L. S. Karlsson, C. Patrik, T. Svensson, T. Mårtensson, B. A. Wacaser, K. Deppert, L. Samuelson, and W. Seifert, "Structural properties of $(111)_B$-oriented III-V nanowires.," *Nat. Materials*, vol. 5, pp. 574–580, 2006.

[20] P. Caroff, K. Dick, J. Johansson, M. Messing, K. Deppert, and L. Samuelson, "Controlled polytypic and twin plane superlattices in III-V nanowires," *Nature Nanotechnology*, vol. 4, pp. 50–55, 2008.

[21] K. Dick, S. Kodambaka, M. Reuter, K. Deppert, L. Samuelson, W. Seifert, L. Wallenberg, and F. Ross, "The Morphology of Axial and Branched Nanowire Heterostructures," *Nano lett.*, vol. 7, pp. 1817–1822, 2007.

[22] Q. Xiong, J. Wang, and P. C. Eklund, "Coherent twinning phenomena: Towards twinning superlattices in III-V semiconducting nanowires.," *Nano Lett.*, vol. 6, pp. 2736–2742, 2006.

[23] J. Zou, M. Paladugu, H. Wang, G. J. Auchterlonie, Y.-N. Guo, Y. Kim, Q. Gao, H. J. Joyce, H. H. Tan, and C. Jagadish, "Growth mechanism of truncated triangular III-V nanowires.," *Small*, vol. 3, pp. 389–393, 2007.

[24] A. Mikkelsen, N. Skold, L. Ouattara, M. Borgström, J. Andersen, L. Samuelson, W. Seifert, and E. Lundgren, "Direct imaging of the atomic structure inside a nanowire by scanning tunnelling microscopy," *Nature Materials*, vol. 3, pp. 519–523, 2004.

[25] H. J. Joyce, Q. Gao, H. Tan, C. Jagadish, Y. Kim, M. Fickenscher, S. Perera, T. Hoang, L. Smith, H. Jackson, J. Yarrison-Rice, X. Zhang, and J. Zou, "Unexpected Benefits of Rapid Growth Rate for III-V Nanowires," *Nano Lett.*, vol. 9, pp. 695–701, 2009.

[26] K. Ikejiri, T. Sato, H. Yoshida, K. Hiruma, J. Motohisa, S. Hara, and T. Fukui, "Growth characteristics of GaAs nanowires obtained by selec-

tive area metal-organic vapour-phase epitaxy ," *Nanotechnology*, vol. 19, p. 265604, 2008.

[27] M. A. Verheijen, G. Immink, T. de Smet, M. T. Borgstrom, and E. P. A. M. Bakkers, "Growth Kinetics of Heterostructured GaP-GaAs Nanowires.," *J. Am. Chem. Soc.*, vol. 128, pp. 1353–1359, 2006.

[28] W. Saxton, W. Baumeister, and M. Hahn, "Three-dimensional reconstruction of imperfect two-dimensional crystals," *Ultramicroscopy*, vol. 13, pp. 57–70, 1984.

[29] R. Algra, M. Verheijen, L.-F. Feiner, G. Immink, R. Theissmann, W. van Enckevort, E. Vlieg, and E. Bakkers, "Paired Twins in GaP Nanowires," *Nano lett.*, vol. 10, pp. 2349–2356, 2010.

[30] H. Gottschalk, G. Patzer, and H. Alexander, "Stacking Fault Energy and Ionicity of Cubic III-V Compounds ," *Phys. Stat. Sol (a)*, vol. 45, pp. 207–217, 1978.

[31] H. Joyce, J. Wong-Leung, Q. Gao, H. Tan, and C. Jagadish, "Phase Perfection in Zinc Blende and Wurtzite III-V Nanowires Using Basic Growth Parameters," *Nano Lett.*, vol. 10, pp. 908–915, 2010.

[32] "Consequently ϕ increases linearly with nanowire height when the side facets are $\{111\}$, *viz.* $\phi \approx \tan(\phi) = 4\ Nh\ \tan(\theta_{\{111\}})\ /\ aD \propto L/D$, where $L = Nh$ is the distance between the growth interface and the position where the cross-section is hexagonal. Note that this relation between deformation and nanowire height is purely a matter of geometry, unrelated to the growth mechanism.,"

[33] "Parameter values: surface energies: solid-liquid: $\gamma_{SL}(\{111\}_B)$ 6.0 eV/ nm^2, $\gamma_{SL}(\{111\}_A)$ 7.0 eV/ nm^2, $\gamma_{SL}(\{100\}_B)$ 5.3 eV/ nm^2, $\gamma_{SL}(\{100\}_A)$ 6.3 eV/ nm^2; solid-vapour: $\gamma_{SV}(\{111\}_B)$ 4.7 eV/ nm^2, $\gamma_{SV}(\{111\}_A)$ 5.7 eV/ nm^2, $\gamma_{SV}(\{100\}_B)$ 4.0 eV/ nm^2, $\gamma_{SV}(\{100\}_A)$ 5.0 eV/ nm^2; liquid-vapour: γ_{LV} 6.5 eV/ nm^2; twinning energy: γ_T0.068eV/ nm^2; edge energies: γ_{AA}0.20eV/nm; γ_{AB} 0.04 eV/nm; layer thickness: h 0.315 nm; contact angle at hexagonal droplet-nanowire interface: $\chi_X(0)$ 15 °; supersaturation: $\Delta\mu = 5.4$ eV/ nm^3, temperature T 460 °C.,"

Chapter 4

Twinning superlattices in InP nanowires

Rienk E. Algra, Marcel A. Verheijen, Magnus T. Borgström, Lou-Fé Feiner, George Immink, Willem J.P. v. Enckevort, Elias Vlieg, Erik P. A. M. Bakkers

We have investigated the formation of twinning superlattices in InP nanowires. We show that we control the crystal structure of indium phosphide (InP) nanowires by impurity dopants. We have found that zinc decreases the activation barrier for 2D nucleation growth of zinc-blende InP and therefore promotes the InP nanowires to crystallize in the zinc blende, instead of the commonly found wurtzite crystal structure. More importantly, we demonstrate that we can, once we have enforced the zinc blende crystal structure, induce twinning superlattices with long-range order in InP nanowires. We can tune the spacing of the superlattices by the wire diameter and the zinc concentration, and we present a model based on the distortion of the catalyst droplet in response to the evolution of the cross-sectional shape of the nanowires to quantitatively explain the formation of the periodic twinning.

This chapter has been published in *Nature, vol 456, p. 369-372* 2008.

4.1 Introduction

Semiconducting nanowires offer the possibility of nearly unlimited complex bottom-up design [1, 2], which allows for new device concepts [3, 4]. However, essential parameters that determine the electronic quality of the wires, and which have not been controlled yet for the III-V compound semiconductors, are the wire crystal structure and the stacking fault density [5]. In addition, a significant feature would be to have a constant spacing between rotational twins in the wires such that a twinning superlattice (TSL) is formed, since this is predicted to induce a direct bandgap in normally indirect bandgap semiconductors [6, 7], such as silicon and gallium phosphide. Optically active versions of these technologically relevant semiconductors will have major impact on the electronics [8] and optics [9] industry. Here, we first show that we control the crystal structure of indium phosphide (InP) nanowires by impurity dopants. We have found that zinc decreases the activation barrier for 2D nucleation growth of zinc-blende InP and therefore promotes the InP nanowires to crystallise in the zinc blende, instead of the commonly found wurtzite crystal structure [10]. More importantly, we demonstrate that we can, once we have enforced the zinc blende crystal structure, induce twinning superlattices with long-range order in InP nanowires. We can tune the spacing of the superlattices by the wire diameter and the zinc concentration, and we present a model based on the distortion of the catalyst droplet in response to the evolution of the cross-sectional shape of the nanowires to quantitatively explain the formation of the periodic twinning.

4.2 Methods

The InP nanowires were synthesized in a low pressure (50 mbar) Aixtron 200 MOVPE reactor on InP $(111)_B$ substrates. The substrates were treated with a piranha etch for 1 min to remove the surface oxide, before deposition of Au colloids of different diameters (ranging from 10 to 200 nm). The nanowires were grown in the VLS growth mode using trimethylindium (TMIn) and phosphine (PH_3) as precursors, at partial pressures of $1.19*10^{-3}$ and $4.17*10^{-1}$ mbar, respectively, in a total flow of $6l$ min^{-1} hydrogen (H_2) carrier gas. As dopant material diethylzinc (DEZn) was used for p-type doping. Before growth, an anneal step was carried out under PH_3/H_2 atmosphere to desorb any surface oxide and to alloy the Au colloids with the InP substrate to ensure epitaxial growth. Growth was initiated when a temperature of 420 °C was reached by switching on the TMIn. To change the dopant concentrations in the wires the DEZn partial pressure was varied between 10^{-2} and 10^{-7} mbar, at constant TMIn and PH_3 molar fractions

in H_2. We like to point out that the used molar fractions for DEZn are controlled gas flows in the reactor and not necessarily the built-in atomic fractions in the wires. The samples were analyzed using transmission electron microscopy (TEM FEI Tecnai 300 kV) in bright field, and high resolution (HRTEM).

4.3 Crystal structure

Twin planes and, more generally, planar stacking faults are commonly found in III-V nanowires grown in the [111] direction by the vapour-liquid-solid (VLS) mechanism. A twin plane in a zinc-blende (ZB) (stacking fault in a wurtzite (WZ)) nanowire can be considered as a monolayer of the WZ (ZB) phase [11]. Stacking faults can significantly affect the electronic properties of the nanowires [5, 7]. The electron wavefunction is discontinuous at a stacking fault which leads, for instance, to a reduced mobility of charge carriers. The formation and resulting morphology of randomly distributed stacking faults in nanowires have been investigated by several authors [11–14]. Twin planes that have a constant spacing within a nanowire form a twinning superlattice (TSL); this modifies the electronic band structure, giving rise to the formation of minibands [7]. Recently, small domain TSLs have been observed locally in bulk Si [15, 16], and occasionally in ZnS nanowires [17], but the parameters controlling the phenomenon were not identified.

The first step in obtaining a twinning superlattice is to control the nanowire crystal structure. Bulk InP has the ZB crystal structure, because the free energy is slightly lower (ΔE=6.8 meV/III-V atom pair) [18] for ZB than for WZ InP. However, nominally undoped InP nanowires commonly exhibit the wurtzite crystal structure. Possible explanations for the formation of WZ nanowires are the lower surface energy of the parallel side facets of WZ wires compared to that of ZB wires [18] and the interface energies at the V-L-S three-phase line [19]. These effects would make crystallisation in the WZ phase especially favourable for thin wires that have a large surface to bulk ratio. We have synthesized InP nanowires from colloidal gold particles by VLS growth using metal-organic vapour phase epitaxy (MOVPE) with trimethylindium and phosphine as molecular precursors, as described in the Methods Section. We consistently observe that undoped InP wires (with diameters from 10 up to 250 nm) have the WZ structure, though in general contain many stacking faults. With increasing diameter the number of stacking faults decreases, leading to wires with a larger fraction of WZ and showing that the above mentioned factors do not ultimately determine the crystal structure of the wires. The main difference between bulk and VLS growth is the presence

of the catalyst particle from which the crystal is precipitated, and therefore the atomic interactions at the liquid-solid interface should be considered. We find that the parameter critically determining the nanowire crystal structure and the stacking fault density is the chemical composition of the catalyst particle near the liquid-solid interface. We introduce diethylzinc (DEZn) in the growth system to establish p-type doping in our nanowires. Importantly, when sufficient Zn is added to the system, the nanowires precipitate in the ZB crystal structure. We find a transition from WZ to ZB at a DEZn partial pressure of $4.6*10^{-5}$ mbar ($4.6*10^{-4}$ mbar corresponds to a free hole concentration of 10^{18} cm^{-3} in the InP nanowires [20]) as is shown in figure 4.1a (see also section 4.9).

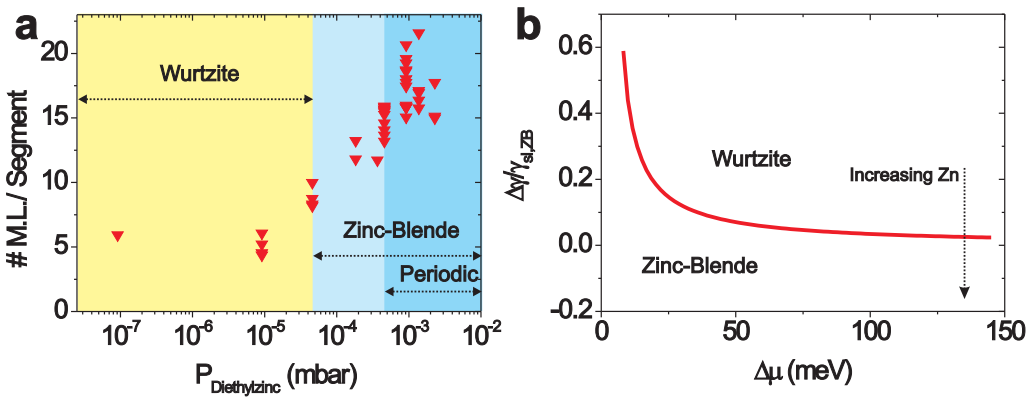

Figure 4.1: The effect of Zn-doping on the nanowire crystal structure (a), The average segment length between two adjacent stacking faults or twin planes as a function of the Zn concentration. A transition from the WZ to the ZB crystal structure is observed at $4.85*10^{-5}$ mbar DEZn, and above $4.85*10^{-4}$ mbar the twin planes have a constant spacing for a given dopant level. The data refers to wires with diameters between 15 and 25 nm. **(b)**, Calculated kinetic phase diagram showing the domains of WZ and ZB as a function of $\Delta\gamma/\gamma_{sl,ZB}$ and $\Delta\mu$. Zn reduces the liquid-solid step energy of ZB with respect to WZ and thus promotes the formation of zincblende InP wires.

For Zn partial pressures between $4.6*10^{-5}$ and $4.6*10^{-4}$ mbar we find that twin planes are randomly distributed in the nanowires. Strikingly, above $4.6*10^{-4}$ mbar the twin planes exhibit a constant spacing for a given Zn concentration and wire diameter, and the nanowire develops a twinning superlattice. The segment length of the TSL increases with the Zn concentration. In order to quantify the effect of Zn on the crystal structure we have calculated, based on 2D nucleation, a

kinetic phase diagram, as shown in figure 4.1b. The obtained curve, which relates the supersaturation in the droplet, $\Delta\mu$, to the (normalized) difference in solid-liquid step free energy between a ZB and a WZ nucleus, $\Delta\gamma/\gamma_{sl,ZB}$, separates the domains of WZ and ZB nanowire growth (see section 4.10). As elaborated in more detail in section 4.10, we argue that the main effect of adding zinc during growth is a decrease in $\Delta\gamma/\gamma_{sl,ZB}$, which means a lowering of the liquid-solid step energy for ZB as compared to WZ. This suggests a strong interaction of the zinc atoms with the InP growth interface as was also observed during electrical resistance measurements of Au(Zn)-InP contacts [21, 22]. In general, for nanowires grown by the VLS mechanism the crystal structure may be intrinsically different from that of the bulk material and will depend on the combination of semiconductor with catalyst material.

4.4 Twinning superlattice

Having adequate control over the nanowire crystal structure, we can now address the formation of twinning superlattices. In figure 4.2, transmission electron micrographs (TEM) are shown of Zn-doped ($9.2*10^{-4}$ mbar) InP nanowires with nominal diameters of 10, 20, 50 and 100 nm.
It is clear from the overview images in figure 4.2a that the periodically twinned structure is general, although not all of the wires have the optimal orientation with respect to the electron beam. The segment length is uniform (figure 4.2b) throughout the wires. From the high resolution images in figure 4.2c we observe that the periodic nanowires have the ZB crystal structure with {111} side facets, which are not parallel with respect to the long nanowire axis. From the high resolution images the number of monolayers between successive twin planes was counted and the data is plotted in the histograms shown in figure 4.3a (here, a monolayer with thickness d_{111}=3.4 Å contains pairs of In and P atoms).
Segment lengths of 7±2, 13±2, 25±3 and 33±6 monolayers were found for wires with a diameter of 10, 20, 50 and 100 nm, respectively, see figure 4.3b. Importantly, the periodicity in twinning is demonstrated by the relatively narrow distributions in segment lengths.

4.5 Qualitative model

For the formation of the twinning superlattice it is crucial that the $\{111\}_A$ and $\{111\}_B$ side facets are tilted in opposite directions (by $\theta = \theta_B = -\theta_A \approx 19.5$) with respect to the nanowire axis (see figure 4.2c).

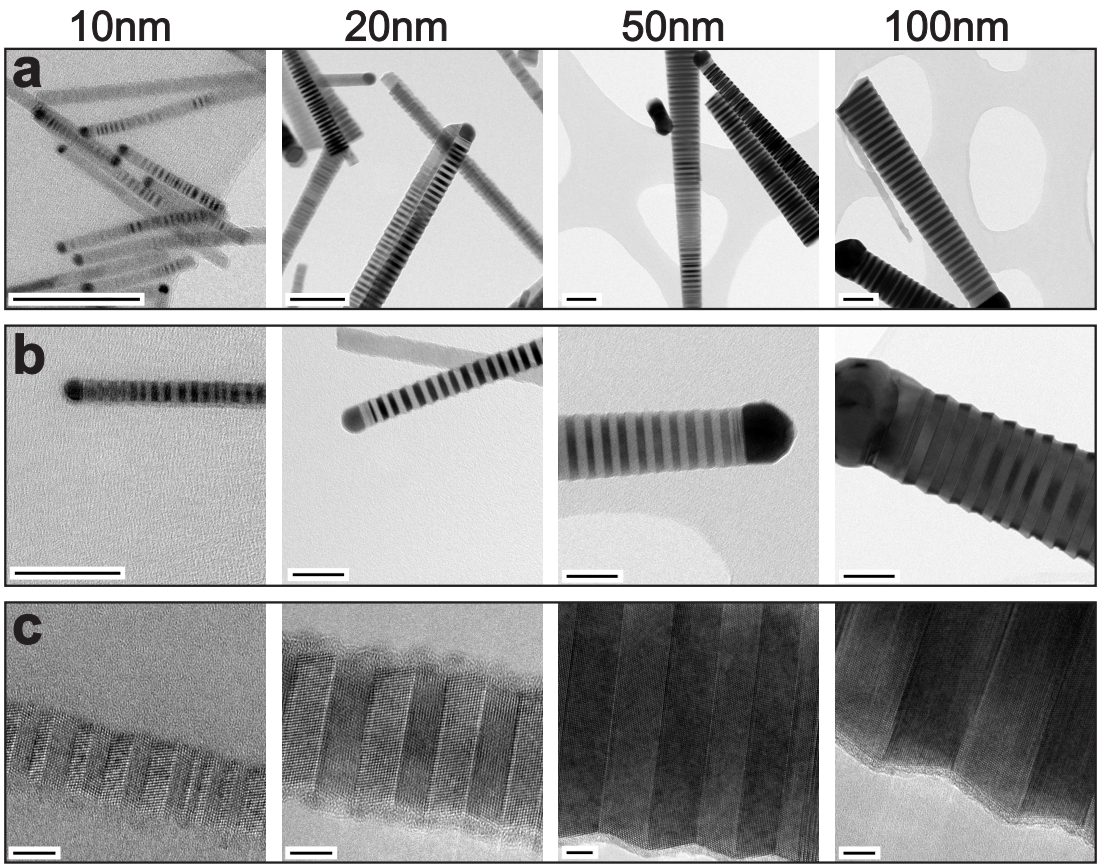

Figure 4.2: Transmission electron micrographs of nanowire twinning superlattices. **(a,b)**, Overview and **(c)**, high resolution TEM images of InP nanowires with a diameter of nominally 10, 20, 50, and 100nm and a DEZn partial pressure of $9.7*10^{-4}$ mbar. The scalebars correspond to **(a)**, 100 nm, **(b)**, 50 nm, and **(c)**, 5 nm. The images are all taken close to the catalyst particle and therefore the observed side facets are due to the VLS growth. Further down the nanowire also lateral growth is observed.

As shown schematically in figure 4.4, at a certain moment during growth (situations 1 and 3) the top surface of the nanowire is a hexagon, and the shape of the catalyst droplet, connected to this surface, is close to spherical. When the wire grows, the $\{111\}_A$ edges move inward and their length increases, while the $\{111\}_B$ edges move outward and their length decreases. Thus the shape of the nanowire-droplet interface becomes increasingly triangle-like, as shown for situations 2 and 4 in figure 4.4b. This induces the catalyst droplet to distort so as to minimize its surface area, leaning over towards the long $\{111\}_A$ edges. At a certain point it becomes more favorable to form a twin plane and to start reducing the distor-

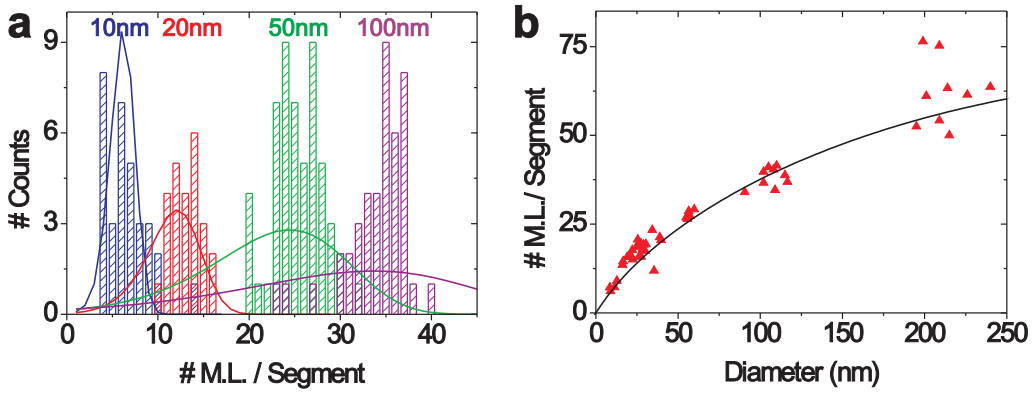

Figure 4.3: The effect of wire diameter on the twin lattice spacing. **(a)**, Histograms of the number of monolayers between two consecutive twin planes for wires with a nominal diameter of 10, 20, 50, and 100 nm. The narrow distributions demonstrate the periodicity. The curves give the calculated distributions obtained from the quantitative model, by using the same parameter values as in 4.3b. **(b)**, The number of monolayers per segment versus the diameter. Each data point represents an averaged value of 25-50 segments, taken from a single nanowire with $9.7*10^{-4}$ mbar DEZn doping. The curve is the theoretical expression given in the text, with $\Delta = 4.5$ and $N_c = A*D$ with $A = 0.35$ nm^{-1}.

tion of the catalyst particle by re-growth towards a hexagonal shape, rather than to continue growth towards a completely triangular shape. This mechanism of inverting triangularly shaped interfaces repeats itself continuously and produces the periodically structured wire.

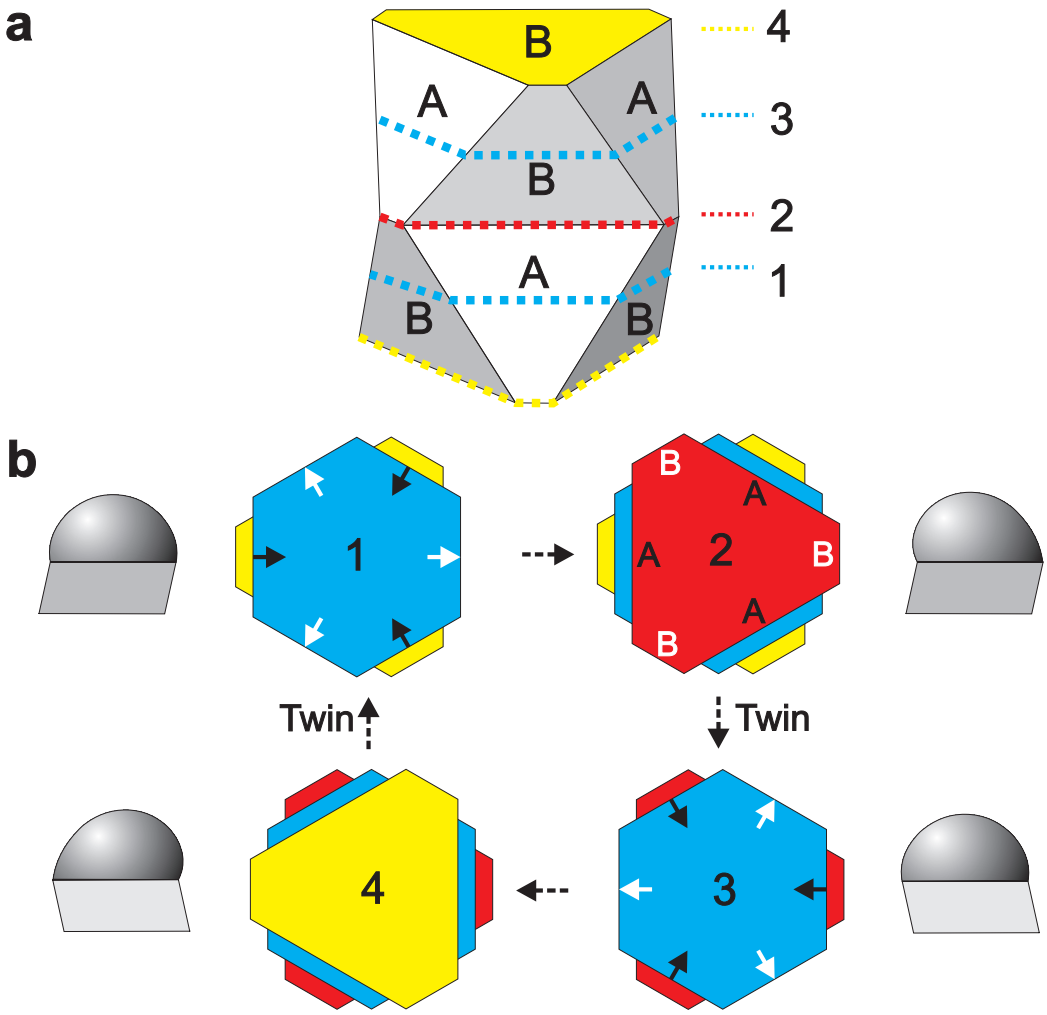

Figure 4.4: Model for periodic twinning in nanowires. **(a)**, Schematic representation of the morphology of a twinned nanowire with the zincblende crystal structure with nonparallel {111} side facets. **(b)**, The cross-sectional shapes of the top facet of the nanowire crystal at the solid-liquid interface during growth. The numbers correspond to the positions indicated in a. Due to the non-parallel orientation of the side facets, $\{111\}_A$ edges increase and $\{111\}_B$ edges decrease in length during vertical growth, and as a result a hexagonal interface develops into a triangle-like shape. At a certain moment, it is energetically more favorable to create a twin plane rather than to continue growing towards a fully triangular top interface. After twin formation a triangle-like shape evolves back to a hexagonal shape and the cycle is repeated as schematized in **(b)**. To the left and right the corresponding calculated shape of the catalyst particle on a hexagonal (1 & 3) and a triangularly deformed (2 & 4) interface is depicted, showing the skewing of the droplet towards the long $\{111\}_A$ side edge and demonstrating that the contact angles depend sensitively on the cross-sectional shape.

4.6 Quantitative model

In order to understand this process in more detail, we developed a quantitative model based upon a specific mechanism relating the distortion of the droplet to the growth process (details are given in section 4.11). Nanowire growth proceeds layer by layer with a single nucleation event per layer, initiated at the nanowire edge [12]. The free energy of formation of the nucleus depends upon the difference between the liquid-solid contact angle and the tilt angle of the external facet of the nucleus. We have analyzed this dependence quantitatively, making use of the simulator program "Surface Evolver" [23, 24]. It follows that the formation of nuclei with an external (solid-vapour) A-facet is strongly suppressed. As a result, the dominant processes are nucleation of external-B-facet nuclei at either B edges, adding another facet-conserving ZB layer, or at A edges, introducing a layer that involves a twin plane and initiating re-growth. During facet-conserving growth the liquid-solid contact angles increase (decrease) at the A edges (B edges) due to the progressing droplet distortion illustrated in figure 4.4. We find that the contact angles depend linearly on the ratio of the wire height $H = Nh$ (with N the number of monolayers measured from the last hexagonal cross section, and h the layer thickness) and the wire diameter D. This is similar to what has been observed for sawtooth faceting in Si nanowires and tentatively explained by considerations based upon total energies instead of nucleation energies [25]. From this, it follows that the difference in free energy of the two competing nucleation processes, $\delta\Delta G^*$, decreases linearly with wire height as

$$\delta\Delta G^* = \delta\Delta G_0^* - CN_h/D \tag{4.1}$$

where $\delta\Delta G_0^*$ is the free energy difference at hexagonal interface shape and C is a constant with the dimension of energy. As a result, we find that the critical number of monolayers, N_c, at which twin formation becomes the more favourable process, is proportional to the wire diameter D. However, the segment length will be substantially less than $2N_c$, because it is determined by the probability of an uninterrupted series of facet-conserving nucleations followed by a facet-changing nucleation. Taking this statistical aspect into account we find that the number of layers in a segment is given by

$$N_s = 2N_c(1 + (1/\Delta)ln[1 - exp(-\Delta/N_c)]) \tag{4.2}$$

where

$$\Delta = \delta\Delta G_0^*/k_BT \tag{4.3}$$

We find excellent agreement between this expression and the observed diameter dependence, as shown in figure 4.3b, if we make use of the explicit expressions (see section 4.11, and [26], in preparation) of $\delta\Delta G_0^*$ and N_c in terms of the physical parameters, *viz.* the solid-liquid surface tension γ_{SL}, liquid-vapour surface tension γ_{LV}, surface energy of a twin plane γ_T, supersaturation $\Delta\mu$, tilting angle θ, contact angle at hexagonal interface shape β_0, and temperature T. In figure 4.3 we used $T = 713$ K, $\gamma_T = 0.009$ J/m^2 [18, 27], $\gamma_{SL}{\approx}\gamma_{SV}{\approx}0.8$ J/m^2 [28], $\gamma_{LV} = 1.0$ J/m^2 (in between the values for liquid Au and In), with $\beta_0 \approx 98\,^\circ$, and $\Delta\mu = 180$ meV/atom pair, which are physically plausible values. In addition, the statistical analysis yields the width of the segment length distribution, as shown in figure 4.3a, using the same parameter values. The trend of increasing width with diameter is correctly reproduced, but the effect is overestimated for the thicker wires. This cannot solely be explained by the probably slightly smaller supersaturation for the larger-diameter nanowires and could indicate that other energies or effects not included in the model might play a role here. In general, to obtain a nanowire TSL with a narrow segment distribution a large $\delta\Delta G_0^*$ and fairly small N_c are required. Since $\delta\Delta G_0^*$ depends on supersaturation as

$$\delta\Delta G_0^* \propto (1/\Delta\mu)^2 \tag{4.4}$$

and N_c on supersaturation and wire diameter as

$$N_c \propto D/\Delta\mu \tag{4.5}$$

it is clear that the supersaturation, determined by the TMI flow, should be chosen low in order to increase $\delta\Delta G_0^*$, and the accompanying increase of N_c be compensated by having a small wire diameter, determined by the catalyst size. Taking the above design rules into consideration, we have recently obtained a twinning superlattice structure in Zn-doped GaP nanowires as well, albeit with a broader segment length distribution. This preliminary result from a different materials system substantiates the general nature of the present approach.

4.7 Complex structures

Our insight in the formation of twins allows the fabrication of more complex structures by varying the Zn concentration during growth. Without Zn, random stacking faults in a WZ crystal structure should occur, and with Zn present the twinning should become periodic. This is indeed the case as demonstrated by the TEM images in figures 4.5a and b, showing a wire for which intermittently a Zn partial pressure of $9.2{*}10^{-4}$ mbar has been used during growth.

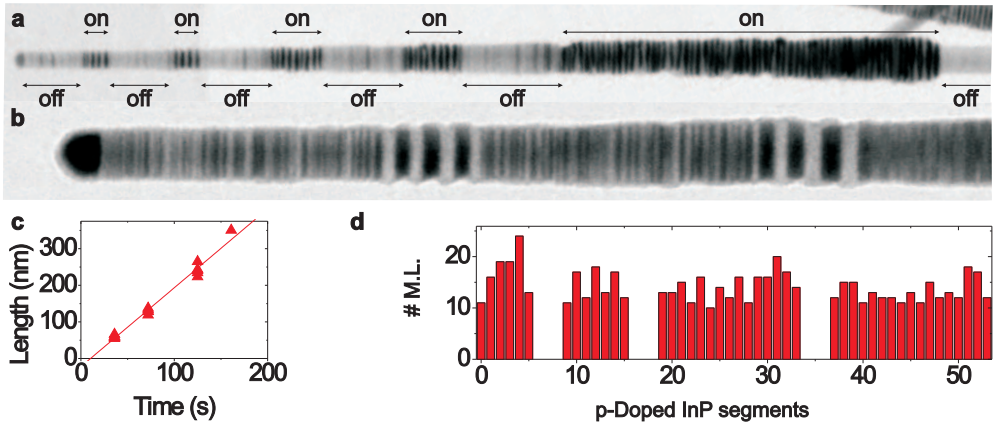

Figure 4.5: InP nanowire with alternating periodic and non-periodic segments. **(a)** An overview TEM image of a wire containing segments of intrinsic InP (containing randomly distributed stacking faults in a WZ structure) and Zn doped ($9.7*10^{-4}$ mbar) segments (with different lengths) with periodic twin planes in a ZB structure. **(b)** Higher magnification TEM image of the segments closest to the gold particle. **(c)** ZB section length versus the time interval during which the Zn precursor gas flow was switched on. The intercept at zero shows abrupt switching between the ZB and WZ crystal structure. **(d)** Number of monolayers in each segment obtained from HRTEM. An average of ∼13±3 monolayers is found.

The tapering of the nanowire is due to sidewall growth, which preferentially occurs on the ZB sections. In figure 4.5c, the length of the ZB sections has been plotted versus the time interval during which the Zn precursor gas flow was switched on. The fitted linear curve has an insignificant offset from zero, suggesting an almost immediate switching from the WZ to the ZB phase and vice versa. In figure 4.5d the number of monolayers between two twin planes is presented for the first four ZB sections. The average segment length is 13±3 monolayers, showing that the periodicity is clearly preserved in these short sections and is not affected by the growth history.

4.8 Conclusions

We have presented a viable and general route for the fabrication of twinning superlattices in nanowires by controlling the nanowire morphology. This new instrument for manipulating the electronic properties of nanowires can be combined with already demonstrated features such as axial and radial heterostructures and doping profiles, further expanding the nanowire toolbox.

4.9 Transition from WZ to ZB by addition of Zinc

By p-doping with zinc, the WZ fraction in the wires changes dramatically at a partial pressure of DEZn around 4.6*10^{-5} mbar. At high dopant levels fewer twin planes are found, and the twinning superlattices develop, see figure 4.6.

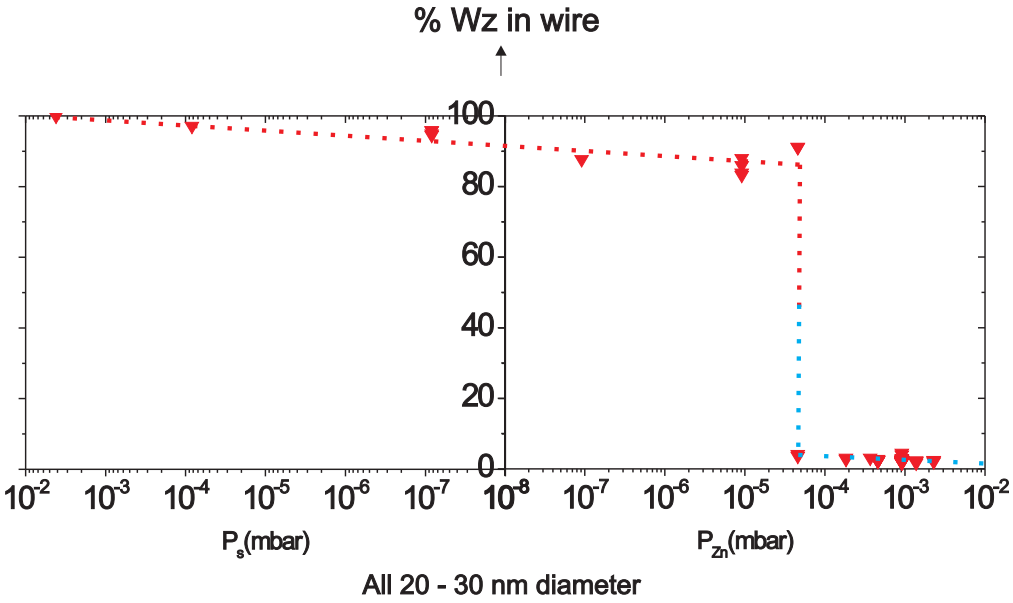

Figure 4.6: Transition from Wz to ZB. Intrinsic InP wires exhibit a Wz crystal structure. At a DEZn partial pressure of 4.6*10^{-5} mbar the crystal structure of the nanowire changes from mainly Wz to mainly ZB. Sulphur on the other hand does not change the crystal structure, but leads to a perfect Wz structure without any stacking faults at high [S].

4.10 Competition of WZ and ZB growth by 2D nucleation

The growth of the InP nanowires proceeds by repeated formation of two-dimensional nuclei on the top faces. To simplify our considerations we approximate the nucleus here as a circle segment and the edge of the nanowire top face as a straight line (figure 4.7).
The shape of the 2D nucleus is determined by the line energies, γ_{sl}, γ_{sv} and γ_{lv}, which are the free energies of the boundaries between the nucleus and the

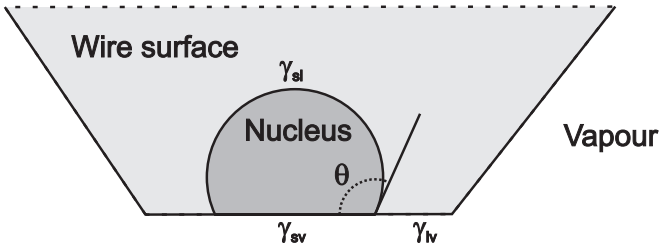

Figure 4.7: Equilibrium shape of a circular 2D nucleus in contact with a straight nanowire edge. Corner nucleation is not taken into consideration because, as explained in section 4.11, the nucleation energy of a corner nucleus is much higher than that of an edge nucleus so that corner nucleation is strongly suppressed.

mother phase, of the nucleus at the nanowire edge and of the mother phase at the nanowire edge respectively. Lower-case subscripts in indicate line energies, whereas capital subscripts denote surface energies. Following Young's equation [29], the contact angle of the nucleus, θ , is given by

$$\cos\theta = \frac{\gamma_{edge}}{\gamma_{sl}} \tag{4.6}$$

with $\gamma_{edge} = \gamma_{lv} - \gamma_{sv}$. The activation barrier, ΔG^*_{het}, for the formation of a heterogeneous two-dimensional nucleus is [30]

$$\Delta G^*_{het} = f(\theta)\Delta G^*_{homo} \tag{4.7}$$

with ΔG^*_{homo} the activation barrier for homogeneous nucleation

$$\Delta G^*_{homo} = \pi\frac{\gamma^2_{sl}}{\Delta\mu}s \tag{4.8}$$

and

$$f(\theta) = \frac{(\theta - 0.5\sin(2\theta))}{\pi} \tag{4.9}$$

In this equation $\Delta\mu = \mu_f - \mu_s$, is the difference in chemical potential of the solute in the droplet, μ_f, and in the solid phase, μ_s, and s is the surface area per molecule. If $\theta = 180\ ^\circ$, *i.e.* $\gamma_{edge}/\gamma_{sl} \leq -1$, then $f(\theta) = 1$ and we have homogeneous nucleation; for heterogeneous nucleation $\theta < 180^\circ$ and $0 \leq f(\theta) < 1$. Wurtzite is preferentially formed if the nucleation barrier for wurtzite (WZ) is less than that for zincblende (ZB):

$$\Delta G^*_{het,WZ} < \Delta G^*_{het,ZB} \tag{4.10}$$

or

$$f(\theta_{WZ})\Delta G^*_{hom,WZ} < f(\theta_{ZB})\Delta G^*_{hom,ZB} \tag{4.11}$$

The reverse holds for preferred ZB growth. Rewriting this criterion and using $\Delta\mu_{WZ} = \Delta\mu_{ZB} - \Delta\Delta\mu$, with $\Delta\Delta\mu$ the difference in chemical potential per III-V pair between the WZ and ZB structure (for InP: $\Delta\Delta\mu = 6.8$ meV [18]) gives

$$\frac{f(\theta_{ZB})\gamma^2_{sl,ZB}}{f(\theta_{WZ})\gamma^2_{sl,WZ}} = \frac{\Delta\mu_{ZB}}{\Delta\mu_{ZB} - \Delta\Delta\mu} \tag{4.12}$$

If we define three edge free energies normalized with respect to $\gamma_{sl,ZB}$, namely $\gamma_{e,ZB} = \frac{\gamma_{edge,ZB}}{\gamma_{sl,ZB}}$, $\gamma_{e,WZ} = \frac{\gamma_{edge,WZ}}{\gamma_{sl,ZB}}$, $\frac{\Delta\gamma}{\gamma_{sl,ZB}}$ with $\Delta\gamma = \gamma_{sl,ZB} - \gamma_{sl,WZ}$ then equation 4.12 can be rewritten as

$$\frac{f(\theta_{ZB})}{f(\theta_{WZ})}\left(\frac{1}{1 - \Delta\gamma/\ \gamma_{sl,ZB}}\right)^2 = \left(1 - \frac{\Delta\Delta\mu}{\Delta\mu_{ZB}}\right)^{-1} \tag{4.13}$$

with $\cos\theta_{ZB} = \gamma_{e,ZB}$ and $\cos\theta_{WZ} = \frac{\gamma_{e,WZ}}{1-\Delta\gamma/\gamma_{sl,ZB}}$. This equation, which can easily be solved numerically, which allows for the construction of (kinetic) $\Delta\gamma/\gamma_{sl,ZB} \leftrightarrow \Delta\mu_{ZB}$ phase diagrams, separating the domains of WZ and ZB growth.
Possible phase diagrams are given in figure 4.8. For homogeneous nucleation the boundary between the domains of WZ and ZB growth is indicated by the red line. A similar boundary is found for heterogeneous nucleation; it is quite close to that of homogeneous nucleation if the energies of the border lines between the nucleus and the nanowires edge are identical for both structures, *i.e.* if $\gamma_{sv,ZB} = \gamma_{sv,WZ}$, and $-1 \leq \gamma_{e,ZB}(= \gamma_{e,WZ}) < 0.2$. If $\gamma_{sv,WZ} < \gamma_{sv,ZB}$, and therefore $\gamma_{e,WZ} > \gamma_{e,ZB}$, then the domain of WZ growth widens as indicated by the lower -green- line in figure 4.8. On the other hand, if $\gamma_{sv,ZB} < \gamma_{sv,WZ}$, ZB is more easily formed and the domain of WZ growth shrinks (upper -blue- line in figure 4.8)
In literature [19], the commonly encountered formation of WZ structure nanowires has been explained by the preferential 2D nucleation of this metastable phase at the edge of the nanowire, due to a lower free energy of the nucleus-nanowire borderline for WZ as compared to ZB nucleation. This leads to an increased domain size of WZ growth, as $\gamma_{e,WZ} > \gamma_{e,ZB}$. Another factor that might enhance preferential nucleation of WZ is a difference in interaction energy of the droplet gold atoms with the InP units at the edge of a WZ and a ZB nucleus, causing $\gamma_{sl,WZ} < \gamma_{sl,ZB}$. Such a difference leads to an increase in $\Delta\gamma/\gamma_{sl,ZB}$ and thus promotes WZ growth (figure 4.8). A high driving force promotes WZ growth as well.
The addition of small amounts of Zn to the vapour phase results in the growth of InP nanowires with ZB structure. It is clear from figure 4.8 that there are three

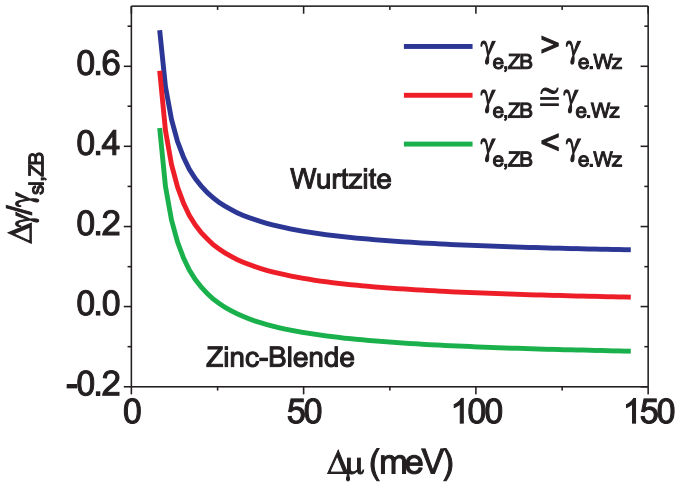

Figure 4.8: Kinetic phase diagram $\Delta\gamma/\gamma_{sl,ZB} \leftrightarrow \Delta\mu_{ZB}$, separating the domains of wurtzite and zincblende formation. Middle red- line: homogeneous nucleation and heterogeneous nucleation with -1 $\leq \gamma_{e,ZB} = \gamma_{e,WZ} <$0.2; Lower green- line: heterogeneous nucleation growth with $\gamma_{e,WZ} = 0.2$ and $\gamma_{e,ZB} = 0$; Upper red- line: heterogeneous nucleation growth with $\gamma_{e,ZB}$= 0.0 and $\gamma_{e,WZ}$ = -0.2. $\Delta\Delta\mu = 6.8$ meV per III-V atom pair. The value of 0.2 is rather arbitrary, and has been chosen to show clearly the effect of differences in $\gamma_{e,ZB}$ and $\gamma_{e,WZ}$. Note, however, that approximating $\gamma_{e,WZ}$ or $\gamma_{e,ZB}$ by $(\gamma_{LV} - \gamma_{SV})/\gamma_{SL}$ and using the surfaces energies mentioned in the main text gives a value close to 0.2.

ways of changing from WZ growth to ZB growth: i) lowering the supersaturation, ii) decreasing $\gamma_{e,WZ} \propto \gamma_{lv} - \gamma_{sv,WZ}$, iii) decreasing $\Delta\gamma$. Driving forces estimated in literature for similar systems range from 50 meV [12] to several hundreds meV [19]. As for these large values of $\Delta\mu$ the transition value of $\Delta\gamma/\gamma_{sl,ZB}$ changes weakly with supersaturation, we expect that in our case the slight alteration in supersaturation introduced by zinc addition plays a limited role in deciding between WZ and ZB growth. The difference between $\gamma_{sv,WZ}$ and $\gamma_{sv,ZB}$ results from a difference in the number of InP dangling bonds [18, 19]. This energy difference, induced by crystallographic properties of the two structures is not influenced by zinc addition. Finally, we do not think that adding small amounts of Zn affects significantly the solid-vapour or the liquid-vapour surface energy of the gold droplet and thus the line energy, γ_{lv}. If γ_{LV} and γ_{SV} would be strongly dependent on Zn concentration, then the droplet contact angle, and thus the nanowire width would vary with the Zn content in the gas phase. This was not

observed as follows directly from figures 4.4a and 4.4b.
The most likely explanation of the transition from WZ to ZB structure growth is a reduction in $\Delta\gamma/\gamma_{sl,ZB} \propto \gamma_{sl,ZB} - \gamma_{sl,WZ}$ upon zinc addition. Resistance measurements have shown that minor amounts of Zn (down to ≈ 0.1 atomic percent Zn) lower the electrical resistance of Au-InP contacts by five orders of magnitude [22]. These samples were annealed at 400 °C prior to measurement; this is a temperature not far from the temperatures used in our nanowire growth experiments. This indicates that Zn atoms strongly interact with the Au-InP interface. As the misorientated and chemically corroded surfaces used in these experiments show a high density of steps, it is quite feasible that the presence of Zn atoms changes the relative values of $\gamma_{sl,ZB}$ and $\gamma_{sl,WZ}$ and thus $\Delta\gamma/\gamma_{sl}$. To verify our hypothesis surface X-ray diffraction experiments are being planned to investigate the atomic structure of the Au-InP and Au(Zn)-InP interfaces.

4.11 Quantitative twinning model

We have developed a model describing the edge-nucleation driven [111] growth of {111}-faceted nanowires, which we summarize here, while a more complete description will be given elsewhere (L.F. Feiner, in preparation). We start by deriving the free energy of formation ΔG^* for the various edge nuclei involved, following the approach of Voronkov [31], which is similar to that applied by Glas et al. to explain the preference for wurtzite growth of nanowires [19]. One finds that ΔG^* takes the familiar form $\Delta G^* \propto (\gamma_{eff})^2/\Delta\mu$, where γ_{eff} is an effective step energy which depends upon the contact angle between the droplet and the external (solid-vapour) facet of the nucleus considered (see figure 4.10).
In order to determine δ we have used the simulator program 'Surface Evolver' [23, 24] to calculate the dependence of the two contact angles (with respect to the droplet-nanowire interface) β_A and β_B at the $\{111\}_A$ and the $\{111\}_B$ side facets, respectively, on the deformation of the droplet-nanowire interface, which we parametrize by (see figure 4.9) the angle $\phi = \arctan(2d/l_0)$, where d is the displacement of the edges, and l_0 is the edge length of the hexagon (proportional to the nanowire diameter D). The dependence is close to linear up to fairly large deformation ($\phi \approx 15\,°$), *i.e.* $\beta_A \approx \beta_0 + \phi$ and $\beta_B \approx \beta_0 - \phi$, where β_0 is the value for a hexagonal interface. This establishes the dependence of β_A and β_B on the wire height H (measured from the hexagonal cross section), since $\tan(\phi) = 4H\tan(\theta)/aD$, where $\theta = \theta_B = -\theta_A \approx 19.5\,°$ is the angle between the 111_B facets and the growth direction (figure 4.9), and $a = 1.10$. Because β_A is not equal to β_B, each of the four possible edge nuclei (*viz.* attached to either

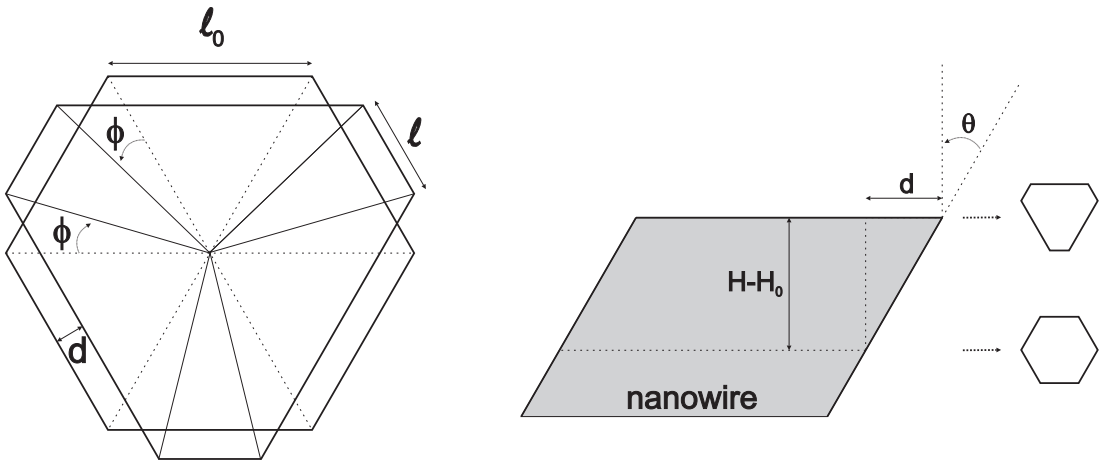

Figure 4.9: Geometry of the droplet-nanowire interface (top) and wire growth (bottom) , defining the deformation angle ϕ , the edge displacement d, the tilting angle θ, and the nanowire height H.

a long-edged A facet or to a short-edged B facet, labeled X, and itself having externally either an A- or a B-facet, labeled Y; see figure 4.10) has a different free energy of formation,

$$\Delta G^*_{XY} \propto \gamma_{SL} - \left(\frac{\gamma_{LV}}{6}\right)\cos(\delta)^{\,2}/\Delta\mu_{XY} \tag{4.14}$$

where $\delta_{XY} = \beta_X - \theta_Y - \pi/2$ is the contact angle of the droplet with respect to the external nucleus facet, and $\Delta\mu_{AA} = \Delta\mu_{BB} = \Delta\mu$ for the nuclei that do not change the side facet, while for the nuclei involving creation of a twin $\Delta\mu_{AB} = \Delta\mu_{BA} = \Delta\mu - \gamma_T/h$, where γ_T is the surface energy of a twin plane and h is the thickness of the nucleus, *i.e.* of a single InP layer. In deriving equation 4.14 it has been assumed that the nuclei have hexagonal shape themselves, and that $\gamma_{SL} \approx \gamma_{SV}$ (because the contact angle between a Au droplet and a planar III/V surface is commonly observed to be close to 90 °). It is straighforward to allow for unequal SL and SV, but this gives only small quantitative corrections. Consideration of the free energies [23, 24] shows that formation of A-facet nuclei is strongly disfavoured because of the unfavourable contact angles, and so the occurrence of twins is determined by the competition between B-facet nuclei nucleating at B edges, adding another ZB layer, and at A edges, introducing a layer involving a twin plane and initiating re-growth. This is governed by the probabilities for the individual nucleation processes,

$$p_{BB}(\phi) \propto (1 - \sqrt{3}\tan\phi) exp\left[\frac{-\Delta G^*_{BB}(\phi)}{k_B T}\right] \tag{4.15}$$

$$p_{AB}(\phi) \propto (1 - \sqrt{3}\tan\phi) exp\left[\frac{-\Delta G^*_{AB}(\phi)}{k_B T}\right] \tag{4.16}$$

with the difference in edge lengths, $l_A > l_B$, taken into account by the prefactors. Setting these probabilities equal determines a critical deformation c, or equivalently a critical height H_c or critical number of layers N_c (with $H_c = N_c\ h$), at which nucleation of a facet-changing nucleus becomes the more favorable process. Because the difference between the free energies of formation is, as follows from equation 4.14,

$$\delta\Delta G^*(\phi) = \Delta G^*_{AB}(\phi) - \Delta G^*_{BB}(\phi) \tag{4.17}$$

$$\propto \left(\frac{1}{\Delta\mu}\right)\left[\frac{\gamma_T}{h\Delta\mu} - 4\frac{\gamma_{LV}}{6\gamma_{SL}}\cos(\beta_0 - \theta)\sin\phi\right] \tag{4.18}$$

$$= \Delta G^*_0 - CNh/D \tag{4.19}$$

where $\delta\Delta G^*_0$ and C depend on the materials parameters γ_{LV}, γ_{SL}, γ_T, $\Delta\mu$, h, θ, and β_0, it follows that H_c is proportional to the diameter D. The segment length $H_s = N_s h$ is smaller than $2H_c$, because it is determined by the probability of an uninterrupted series of N_s facet-conserving nucleations followed by a facet-changing nucleation, not by that for a single facet-changing nucleation. An accurate estimate for N_s is obtained by considering the probability for a segment to end after N_h layers starting from the hexagonal interface, determining the value $N_{h,max}$ for which this probability reaches its maximum value, and setting $N_s = 2N_{h,max}$. The result is

$$N_s = 2N_c\left[1 + \left(\frac{1}{\Delta}\right) ln\left(1 - exp\left[\frac{-\Delta}{N_c}\right]\right)\right] \tag{4.20}$$

as given in the text and shown in figure 4.3b. Finally, we note that the 'Surface Evolver' simulations show that the contact angle is in fact not constant along the edges but decreases rapidly when one approaches a corner. This implies that, according to equation 4.14, the nucleation energy is much higher for a nucleus at the corner (both for the type producing facet continuation and for the type inducing a twin plane) than for a nucleus at the edge center. Corner nucleation is thus strongly suppressed, which justifies our neglect of it.

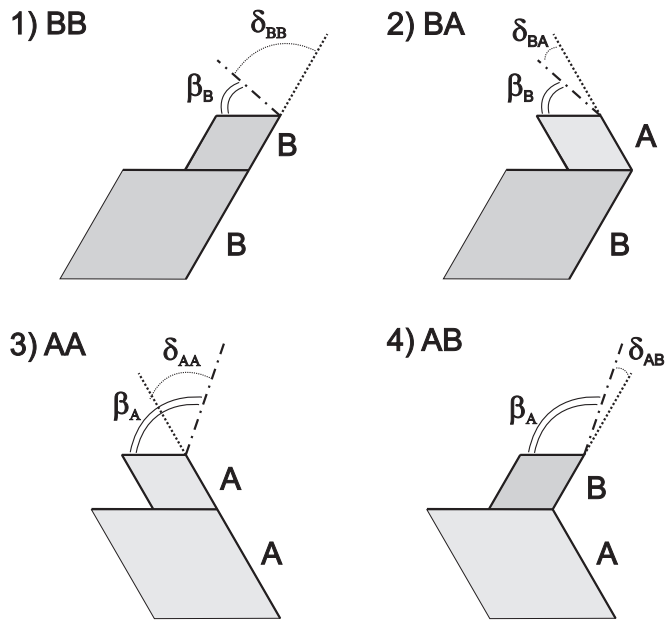

Figure 4.10: The four possible nucleation processes, denoted by XY for nucleation of a nucleus with external (solid-vapour) Y-type facet at the edge of an X-type side facet of the nanowire. The contact angles β_X between the droplet and the droplet-nanowire interface are determined by the edge of the side facet.

References

[1] M. Gudiksen, L. Lauhon, J. Wang, D. Smith, and C. Lieber, "Growth of nanowire superlattice structures for nanoscale photonics and electronics.," *Nature*, vol. 415, pp. 617–620, 2002.

[2] K. Dick, K. Deppert, M. Larsson, T. M*å*rtensson, W. Seifert, L. R. Wallenberg, and L. Samuelson, "Synthesis of branched 'nanotrees' by controlled seeding of multiple branching events," *Nature Mat.*, vol. 3, pp. 380–384, 2004.

[3] A. Hochbaum, R. Chen, R. Delgado, W. Liang, E. Garnett, M. Najarian, A. Majumdar, and P. Yang, "Enhanced thermoelectric performance of rough silicon nanowires," *Nature*, vol. 451, pp. 163–168, 2008.

[4] J. A. van Dam, Y. Nazarov, E. P. A. M. Bakkers, S. De Franceschi, and L. P. Kouwenhoven, "Supercurrent reversal in quantum dots," *Nature*, vol. 442, pp. 667–670, 2006.

[5] J. Bao, D. Bell, F. Capasso, J. Wagner, T. M*å*rtensson, J. Tr*ägå*rdh, and

L. Samuelson, "Optical properties of rotationally twinned InP nanowire heterostructures," *Nano Lett.*, vol. 8, pp. 836–841, 2008.

[6] Z. Ikonic, G. Srivastava, and J. C. Inkson, "Electronic properties of twin boundaries and twinning superlattices in diamond-type and zinc-blende-type semiconductors.," *Phys. Rev. B*, vol. 48, pp. 17181–17193, 1993.

[7] Z. Ikonic, G. P. Srivastava, and J. C. Inkson, "Optical properties of twinning superlattices in diamond-type and zinc-blende-type semiconductors.," *Phys. Rev. B*, vol. 52, pp. 14078–14085, 1995.

[8] A. Lui and M. Paniccia, "Advances in silicon photonic devices for silicon based optoelectronic applications," *Physica E*, vol. 35, pp. 223–228, 2006.

[9] M. Krames, O. Shchekin, R. Mueller-Mach, G. Mueller, L. Zhou, G. Harbers, and M. Craford, "Status and future of high-power- light-emitting diodes for solid-state lighting.," *J. Display Tech.*, vol. 3, pp. 160–175, 2007.

[10] M. Mattila, T. Hakkarainen, M. Mulot, and H. Lipsanen, "Crystal-structure-dependent photoluminescence from InP nanowires.," *Nanotechnology*, vol. 17, pp. 1580–1583, 2006.

[11] K. Hiruma, M. Yazawa, T. Katsuyama, K. Ogawa, K. Haraguchi, M. Koguchi, and H. Kakibayashi, "Growth and optical properties of nanometer scale GaAs and InAs whiskers.," *J. Appl. Phys.*, vol. 77, pp. 447–462, 1995.

[12] J. Johansson, L. S. Karlsson, C. Patrik, T. Svensson, T. Mårtensson, B. A. Wacaser, K. Deppert, L. Samuelson, and W. Seifert, "Structural properties of $(111)_B$-oriented III-V nanowires.," *Nat. Materials*, vol. 5, pp. 574–580, 2006.

[13] Q. Xiong, J. Wang, and P. C. Eklund, "Coherent twinning phenomena: Towards twinning superlattices in III-V semiconducting nanowires.," *Nano Lett.*, vol. 6, pp. 2736–2742, 2006.

[14] M. Verheijen, R. Algra, M. Borgström, G. Immink, E. Sourty, W. van Enckevort, E. Vlieg, and E. Bakkers, "Three dimensional morphology of GaP-GaAs nanowires revealed by transmission electron microscopy tomography.," *Nano Lett.*, vol. 7, pp. 3051–3055, 2007.

[15] A. Fissel, E. Bugiel, C. Wang, and H. Osten, "Formation of twinning-superlattice regions by artificial stacking of Si layers," *J. Cryst. Growth*, vol. 290, pp. 392–397, 2006.

[16] H. Hibino, K. Sumitomo, and T. Ogino, "Twinned epitaxial layers formed on Si(111) 3x 3-B.," *J. Vac. Sci. Technol. A*, vol. 16, pp. 1934–1937, 1998.

[17] Y. Hao, G. Meng, Z. Wang, C. Ye, and L. Zhang, "Periodically twinned nanowires and polytypic nanobelts of ZnS: The role of mass diffusion in vapor-liquid-solid growth.," *Nano Lett.*, vol. 6, pp. 1650–1655, 2006.

[18] T. Akiyama, K. Sano, K. Nakamura, and T. Ito, "An empirical potential approach to wurtzite- zinc-blende polytypism in group III-V semiconducting nanowires.," *J. J. Appl. Phys.*, vol. 45, pp. L275–L278, 2006.

[19] F. Glas, J. Harmand, and G. Patriarche, "Why does Wurtzite form in nanowires of III-V Zinc Blende semiconductors? ," *Phys. Rev. Lett.*, vol. 99, p. 146101, 2007.

[20] E. Minot, F. Kelkensberg, M. V. Kouwen, J. V. Dam, and L. Kouwenhoven, "Single Quantum dot nanowire LEDs ," *Nano Letters*, vol. 7, pp. 367–371, 2007.

[21] V. Malina, V. Micheli, J. Kohout, and D. Berkova, "Effect of deposition parameters in the electrical and metallurgical properties of Au-Zn contacts to p-type InP.," *Semicond. Sci. Technol.*, vol. 9, pp. 1523–1528, 1994.

[22] G. Weizer, N. Fatemi, and A. Koreni-Both, "Au/Zn contacts to -InP: Electrical and metallurgical characteristics and the relationship between them.," *NASA Technical Memorandum*, p. 106590, 1994.

[23] K. Brakke, "The surface evolver," *Experimental Mathematics*, vol. 1, pp. 141–165, 1992.

[24] "http://www.susqu.edu/brakke/evolver/evolver.html,"

[25] F. M. Ross, J. Tersoff, and M. C. Reuter, "Sawtooth faceting in silicon nanowires.," *Phys. Rev. Lett.*, vol. 95, p. 146104, 2005.

[26] L. Feiner, "To be published.,"

[27] D. Hurle, "A mechanism for twin formation during Czochralski and encapsulated vertical Bridgman growth of III-V compound semiconductors.," *J. Cryst. Growth*, vol. 147, pp. 239–250, 1995.

[28] Q. Liu, N. Moll, M. Scheffler, and E. Pehlke, "Equilibrium shapes and energies of coherent strained InP islands.," *Phys. Rev. B*, vol. 60, p. 17008, 1999.

[29] T. Young, "An essay on the cohesion of fluids," *Phil. Trans. Roy. Soc.(London)*, vol. 95, p. 65, 1805.

[30] W. v. Enckevort, "Contact nucleation of steps: Theory and Monte Carlo simulations," *J.Cryst. Growth*, vol. 259, pp. 190–207, 2003.

[31] V. Voronkov, "Processes at the boundary of a crystallization front.," *Sov. Phys. Crystallogr.*, vol. 19, pp. 573–577, 1974.

Chapter 5

The effect of the catalyst surface energy and chemical potential during GaP twinning superlattice nanowire growth

Rienk E. Algra, Marcel A. Verheijen, Lou-Fé Feiner, George G.W. Immink, Willem J.P. van Enckevort, Elias Vlieg, Erik P.A.M. Bakkers

Twinning superlattices are predicted to give rise to a direct bandgap in normally indirect materials. Control in the segment length between two successive twin planes is crucial in order to manipulate the band structure. Here we show for the first time that we are able to synthesize GaP twinning superlattice nanowires. Moreover by controlling the Ga pressure during growth we can alter the segment length independently from already known parameters like the nanowire diameter, Zn-concentration and temperature. From the experimental data we are able to extract the effect of the chemical potential on the superlattice segment length and compare this with our previously developed quantitative model for InP superlattices. We find that the surface energy rather than the chemical potential has a major effect on the superlattice segment length.

This chapter has been submitted

5.1 Introduction

The defect density and crystal structure critically determine the opto-electronic properties [1–3] of nanowires. For nanowires grown by the vapor-liquid-solid (VLS) growth mechanism, it has been shown that these structural characteristics can be tuned by impurities [4], temperature [5, 6], diameter [7–9], III-V [6, 10] ratio or by a combination of these parameters. It has been argued that the chemical potential in the droplet [11], the nanowire surface energy [12], the solid-liquid [4] or the liquid-vapor [13] interface energies could be affected by these parameters and thereby driving the formation of planar defects and/or specific crystal structures. These energies have not been determined experimentally and their exact role has not been substantiated. Here, we quantify the chemical potential in the liquid catalyst particle ($\Delta\mu$) and the liquid-vapor surface energy (γ_{LV}) during growth of GaP twinning superlattice (TSL) nanowires. We demonstrate that the catalyst surface tension is the main parameter determining the defect density. This unexpected result implies that surfactants can be used during nanowire growth to uniquely engineer the nanowire defect and crystal structure.
The formation of a twinning superlattice, in which the distance between neighbouring twin planes is constant, in nanowires has been well understood. Our quantitative model [4] gives the particular possibility to reveal the contribution of individual parameters to the nanowire growth from the combination of experiment and theory. In this study, we use GaP twinning superlattice nanowires and investigate the effect of the tri-methyl-gallium (TMG) vapor pressure, P_{Ga}, on the defect density for a range of nanowire diameters. We find that P_{Ga} affects both the segment length (the distance between two neighboring twin defects) and the nanowire growth rate. By fitting our model [4] describing the formation of a TSL to the data, we obtain absolute values of $\Delta\mu$ and γ_{LV}. As a reference, $\Delta\mu$ has been determined independently from the overall nanowire growth rate. The values obtained from these two routes are consistent.

5.2 Results

5.2.1 GaP superlattices

We have synthesized twin superlattices in GaP nanowires via the Vapor-Liquid-Solid (VLS) growth mechanism on $(111)_B$ GaP substrates at a temperature of 550 °C similar as described previously [14]. Wires grown without dopants have the wurtzite crystal structure containing many defect planes [6]. Following the strategy to make TSLs in InP [4], we have added diethylzinc (DEZn). With

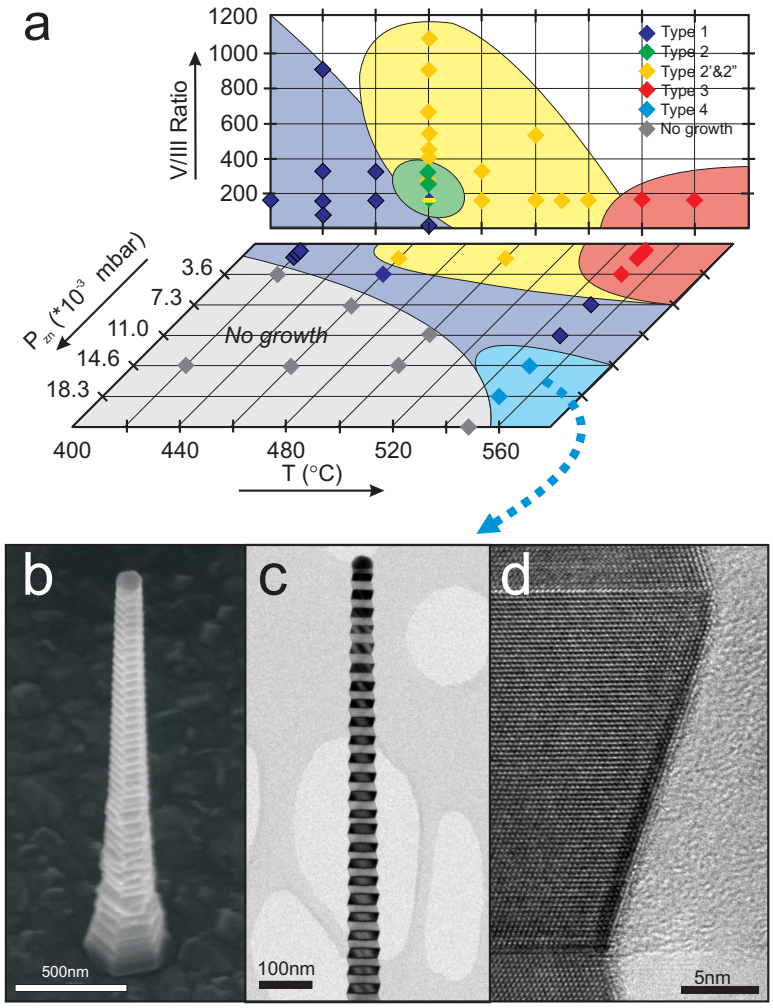

Figure 5.1: GaP superlattice (a) Graph showing the different morphology regimes of GaP nanowire growth. The temperature versus III-V ratio reveals 3 different types of morphology [6]. Type 1 being a {111} and type 2 a $\{11\bar{2}\}$ terminated morphology with the zinc-blende crystal structure. Type 3 represents the wurtzite crystal structure. By adding sufficient DEZn as a p-dopant during growth at high temperature the regime of the TSL (type 4), can be recognized. The samples with DEZn are grown on a GaP substrate, whereas the samples in the III-V versus temperature graph are grown on SiO_2. These two substrates can have a different effective decomposition of the precursors. Therefore the two graphs are deliberately separated, since it is unknown how the GaP III-V relates to that of SiO_2. **(b)** SEM image of a 100nm diameter GaP twin superlattice nanowire. Clearly the characteristic regular {111} faceting can be seen which is originated by the twin superlattice. **(c)** TEM image revealing the twin superlattice in GaP. Each change in contrast is a twin plane which can be seen in high resolution (HRTEM) in **(d)**.

a DEZn partial pressure (P_{DEZn}) above $\sim 7{*}10^{-3}$ mbar, the wires crystallize in the zinc-blende structure with randomly spaced defect planes, and for $P_{DEZn} \geq \sim 1.4{*}10^{-2}$ mbar the wires exhibit a periodic twinning structure. Below 550 °C no periodic structures were obtained even with high P_{DEZn} [see figure 5.1a]. Although it is not clear what the effect of the addition of Zn is, it appears to have the general effect to change the crystal structure from wurtzite to zinc-blende and induce a TSL above a certain concentration [15]. All data in this paper has been collected from wires grown with a P_{DEZn} of $1.4{*}10^{-2}$ mbar.
In figure 5.1b a SEM image is shown for a GaP nanowire that reveals a periodic structure, typical for a twinning superlattice. The TSL can be seen in more detail in the bright field TEM images (figure 5.1c) where the twin planes are at a constant distance. These planar defects can be recognized by the alternating change in contrast. From high resolution TEM in figure 5.1d the crystal structure is determined to be zinc-blende. Additionally, the characteristic {111} side facets, which make an angle of 19.5 ° with respect to the growth direction, are clearly visible. During growth, these non-parallel side facets result in a deformation of the nanowire top facet, which is in contact with the liquid metal particle. This leads to a distortion of the liquid particle, changing the contact angles with the nanowire. At a specific level of distortion a twin plane is formed, inverting the structure, and the process starts over again. The repetition of this process results in the formation of periodic twin superlattices [4].

5.2.2 Ga partial pressure

In order to verify if the mechanism for the formation of the TSL in GaP is the same as in InP, we have studied the dependence of the segment length on the wire diameter (figure 5.2a). It is clear that the segment length increases with diameter (for a given P_{Ga}) following a similar trend as observed for InP wires indicating that the same mechanism applies (the appendix 5.5 shows the comparison between InP and GaP superlattices). A detailed analysis will be given later. Importantly, we also observe an increase of the segment length with decreasing P_{Ga}. This is a new parameter, which allows us to tune the defect density without affecting other nanowire properties (dopant concentration, morphology or diameter [4] and temperature [5]).
We find a maximum (minimum) segment length for $P_{Ga} = 2.3{*}10^{-4}$ mbar ($P_{Ga} = 4.6{*}10^{-3}$ mbar), under the present growth conditions (figure 5.2a). For even lower P_{Ga} the segment length still increases, but these wires have a rough {111} morphology. At the lowest applied P_{Ga} the axial growth rate is very low and due to the long exposure time to the gas phase, lateral growth is more pronounced

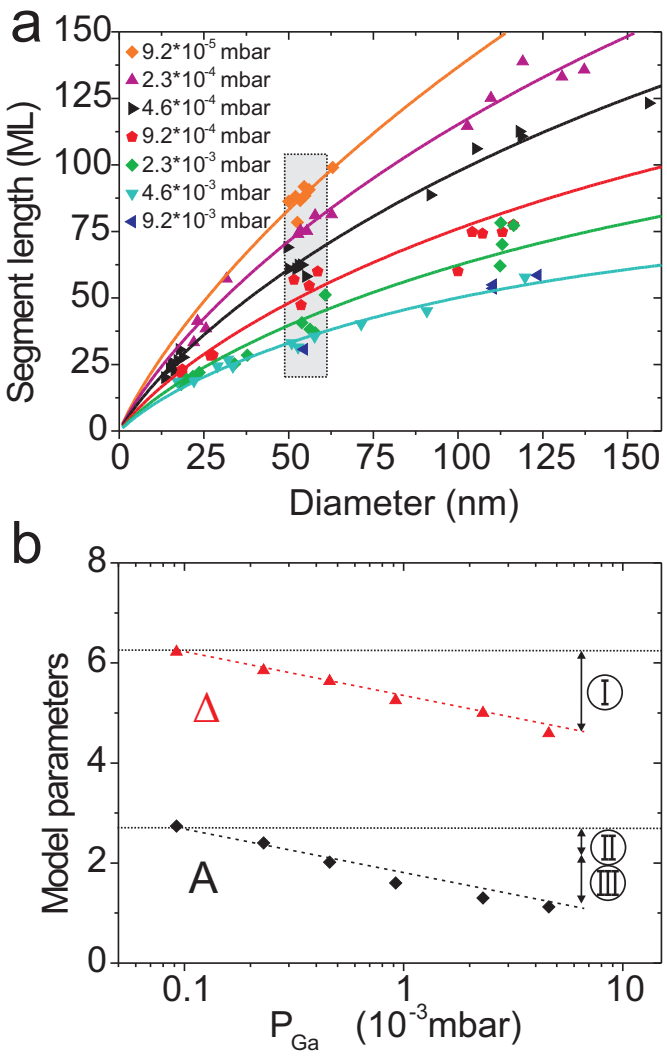

Figure 5.2: Ga partial pressures (a) Segment length of the twin superlattice as a function of diameter for different TMGa partial pressures ranging from $9.2*10^{-5}$ to $9.2*10^{-3}$ mbar. The solid lines are curves fitted by our model with surface and twin energies typical for GaP. The grey box indicates the regime where the distributions shown in figure 5.3 are taken. The lines are fits by our quantitative model [4], which depend on the chemical potential and the surface energies. **(b)** The fit parameters for the segments lengths versus TMGa pressures, plotted in **(a)**. The effect of the chemical potential as well as the liquid-vapor surface energies in shown. (I) indicates the effect of $(\gamma_{SL}/\Delta\mu)^2$ whereas (II) shows the effect of $(\gamma_{SL}/\Delta\mu)$ and (III) $(1/\gamma_{LV})$.

compared to samples grown with slightly higher P_{Ga}. The lateral growth rate is different for the different {111} facets, which induces roughening of the wire. At the highest applied P_{Ga} the morphology is no longer determined by 'pure', non-parallel {111} facets, but rather by a combination of {111} and $\{11\bar{2}\}$ nanofacets.

These $\{11\bar{2}\}$ side facets are oriented parallel to the growth direction. The cross-sectional nanowire shape will not deform with these parallel nano-facets and therefore the deformation of the growth droplet during axial growth is slowed down. As a result, the segment length increases. As the $\{11\bar{2}\}$ nucleation is a random event, the segment length distribution will widen to larger segment lengths. Furthermore, as can be seen from figure 5.3b, due to this additional nucleation event the characteristic {111} zig-zag morphology no longer coincides with the twin planes. Thus, the range, in which a TSL can be controllably grown is $2.3*10^{-4} < P_{Ga} < 4.6*10^{-3}$ mbar.
For wires with a diameter shown in the shaded gray area in figure 5.2a the distribution in segment length has been determined in more detail from high-resolution TEM and is shown in figure 5.3a. We use wires within a narrow range of diameters (52.8 nm < D < 60.8 nm), since the diameter also affects the average segment length and the width of the distribution [4]. The narrow distributions in the histograms demonstrate the periodicity of the superlattice structures. The absolute width of the distribution does not significantly change with P_{Ga} (except for the highest P_{Ga} which is outside the controlled TSL growth regime, due to the presence of $\{11\bar{2}\}$ facets).

5.2.3 Chemical potential and surface energy

In our paper on InP [4] we have shown that the separation (N_s) between adjacent twins in a twin superlattice nanowire follows the relation

$$N_s = 2N_c(1 + (1/\Delta)ln[1 - exp(-\Delta/N_c)]) \tag{5.1}$$

in which the critical segment length, at which twin formation becomes the more favorable process is defined as $N_c = A\ D$, with D is the wire diameter, and $\Delta = \delta\Delta G_0^*/k_BT$. $\delta\Delta G_0^*$ is the free energy difference at the hexagonal interface shape, $/k_B$ the Boltzmann constant and T the temperature. The two fitting parameters A and Δ are used to describe the turning point where the creation of a twin plane becomes more favorable than continued growth and are given by:

$$A \propto \left(\frac{\gamma_{SL}}{\Delta\mu}\right)\left(\frac{1}{\gamma_{LV}}\right) \tag{5.2}$$

and

$$\Delta \propto \left(\frac{\gamma_{SL}}{\Delta\mu}\right)^2 \tag{5.3}$$

where γ_{LV} and γ_{SL} are the surface energies of the liquid-vapor and solid-liquid interfaces, respectively, and $\Delta\mu$ is the chemical potential in the liquid particle.

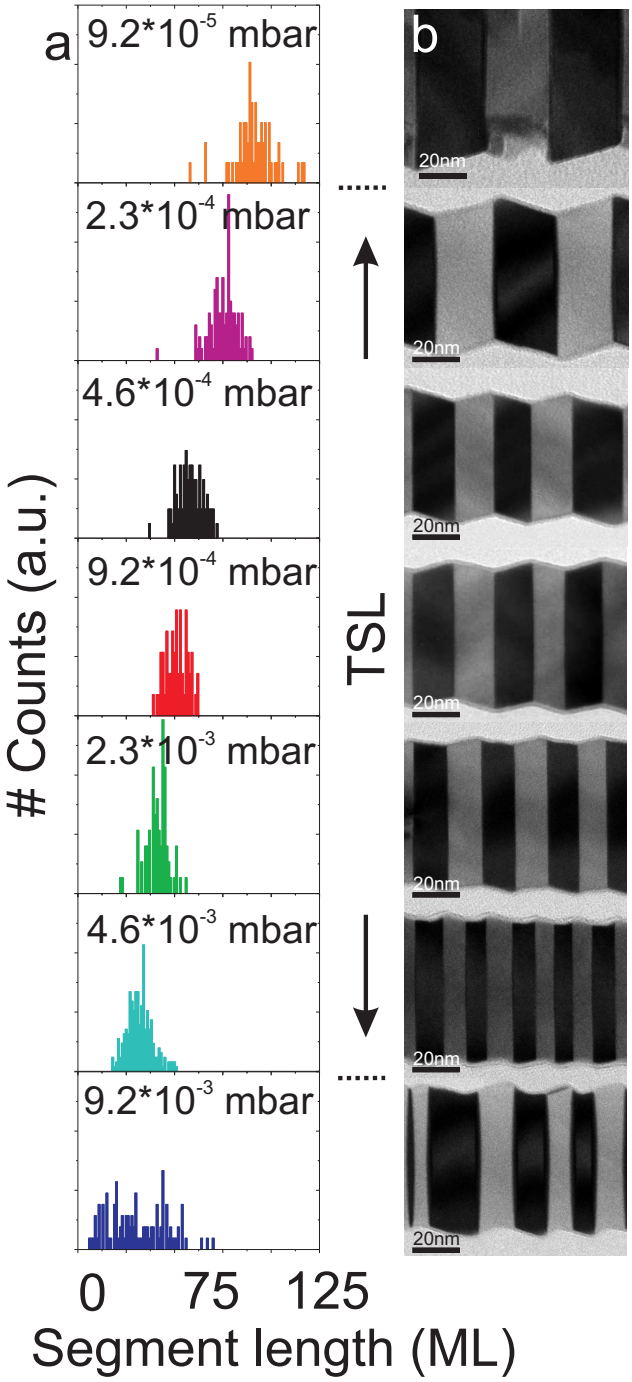

Figure 5.3: Distributions **(a)** For different P_{Ga} pressures the segment length distribution is shown. The data is collected by counting 56-253 segments in a single wire with diameters between 52.8 and 60.8nm. **(b)** TEM images corresponding to the distributions shown in **(a)**. Clearly the segment length decreases with increasing P_{Ga}.

Here we use equation 5.1 to analyse the obtained data in figure 5.2a in order to reveal the effect of the supersaturation and surface energies on the TSL formation. For this, we fit the segment length (N_s) as a function of the diameter for the different P_{Ga} as shown in the same figure. The good agreement between the data and the fits shows that the formation of the GaP TSL is accurately described by the model. The obtained parameter values are plotted in figure 5.2b.
From equations 5.2 and 5.3 we expect a linear decrease of A and a quadratic decrease of Δ with $\Delta\mu^{-1}$, if either $\Delta\mu$ or γ_{SL} is the only parameter affected by a change in P_{Ga}. We find, however (see figure 5.2b), that A decreases from 2.7 to 1.1 and Δ from 6.2 to 4.6. The relatively small change of Δ compared to A shows that $\Delta\mu$ and γ_{SL} are thus not the main origin for the change of the TSL segment length as a function of P_{Ga}. The observed trends in the parameter values can only be explained by a strong dependency of γ_{LV} on P_{Ga}, since γ_{LV} is the parameter that only affects A (and not Δ). From equations 5.2 and 5.3, we can obtain quantitative values for $\Delta\mu$ and γ_{LV}, if we assume that γ_{SL} does not change with P_{Ga}. The fact that the size of the gold-particle does not change significantly as a function of the P_{Ga}, as can be seen in the gray area of figure 5.2, indicates that the liquid status does not change too much. This indicates a more or less constant γ_{SL}. In figure 5.2b the effect of the different parameters is given. (I) Indicates the effect of $(\gamma_{SL}/\Delta\mu)^2$ whereas (II) shows the effect of $(\gamma_{SL}/\Delta\mu)$ and (III) $(1/\gamma_{LV})$. We find that the effect of the surface tension is approximately three times larger than the effect of the supersaturation on the segment length of the TSL. If we assume γ_{SL} to be constant, then the effect (I) indicates a $\Delta\mu$ change of only $\approx 5\%$ upon going from P_{Ga}= 9.2*10^{-5} mbar to 4.6*10^{-3} mbar.
The large effect of γ_{LV} on the defect density could be employed to engineer the crystal structure in nanowires. The liquid-vapor surface energy can be affected by surfactants during growth to induce controllable homo-junctions, *i.e.* junctions between different crystal structures of the same material.
As a reference, we have used another, independent, route to obtain $\Delta\mu$ by using the nanowire growth rate, R. Figure 5.4a shows that the growth rate increases with P_{Ga}. We derive the chemical potentials from R via the following equation for growth through 2D nucleation [16]:

$$R = [B_0 D] exp\left(\frac{\Delta\mu}{kT}\right)(\Delta\mu)^{1/2} exp\left(\frac{Y}{kT\Delta\mu}\right) \tag{5.4}$$

where Y/kT is a constant ($\sim$ 17*10^{-19} J) for the activation energy of homogeneous nucleation and B_0 a kinetic constant, which is independent of the chemical potential. Using equation 5.4, we obtain a plot of $\Delta\mu$ versus P_{Ga} for three different values of B_0 as shown in figure 5.4b. Importantly, independent of the value for

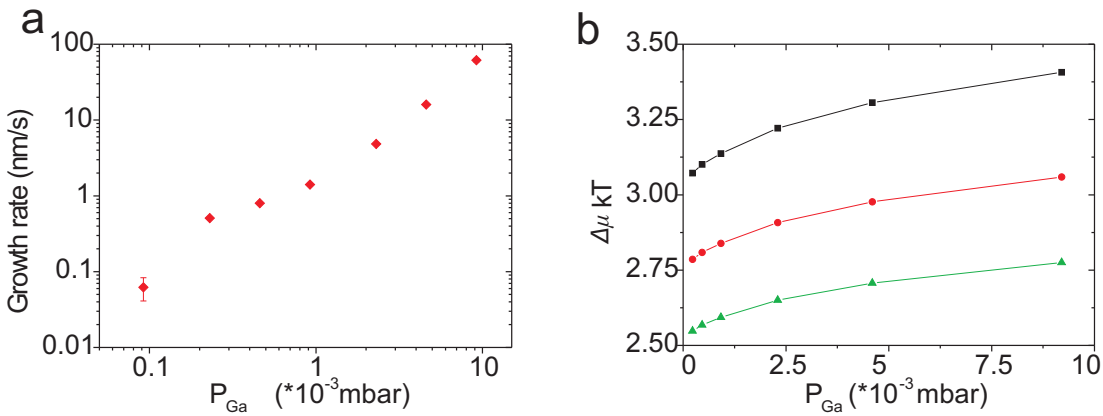

Figure 5.4: Chemical potential and surface energy (a) Dependence of growth rate as a function of the applied Ga-flow during growth. The growth rate are shown for nanowires with a diameter of 50-60nm. **(b)** Calculated chemical potentials for the different partial pressure via the measured growth rates, as shown in equation 1. The green, red and black curves are calculated with a B_0D of 58, 53 and 48, respectively. For all calculations a value of 17*10^{-19} J is used for Y/kT.

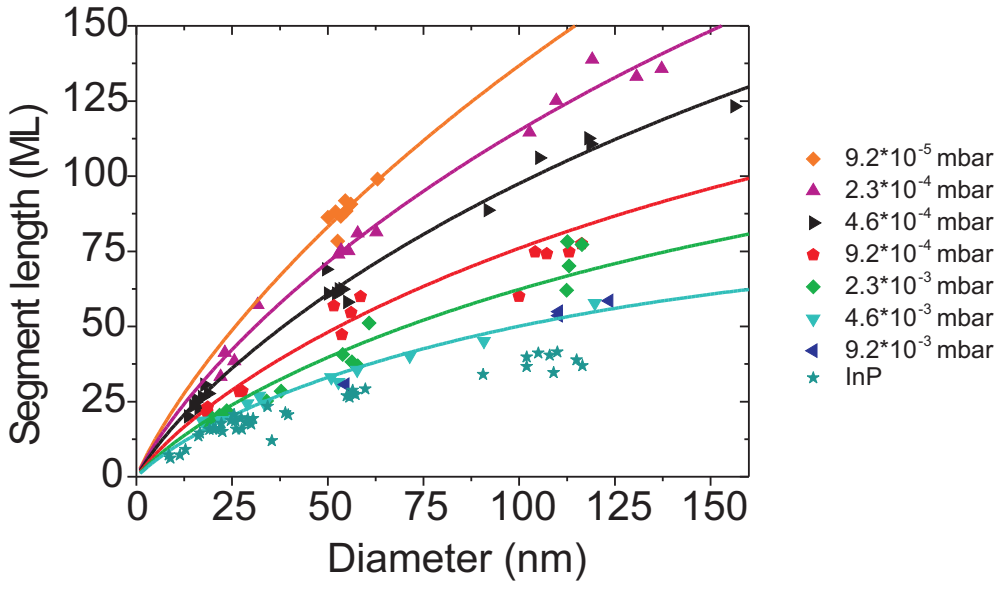

Figure 5.5: Comparison GaP and InP superlattices Segment length of the GaP twin superlattice as a function of diameter for different P_{Ga} partial pressures (equivalent to figure 5.2) and the InP TSL [4]. Clearly both materials systems obey the same trends which indicates that our quantitative model is applicable to both systems.

the kinetic constant B_0 we find that $\Delta\mu$ increases only slightly with P_{Ga} showing that a change of P_{Ga} only slightly affects $\Delta\mu$, which is consistent with the TSL analysis.

5.3 Conclusions

To our best knowledge this is the first time that the chemical potential and the catalyst surface energy have been determined quantitatively from experiments. These general parameters are essential for a better understanding and proper modeling of nanowire growth. Ultimate control of nanowire crystal structure, and defect density can be obtained by tuning the surface energies.

5.4 Acknowledgements

This research was carried out under project number MC3.05243 in the framework of the strategic research program of the Materials Innovation Institute (M2i) (www.M2i.nl), the former Netherlands Institute of Metals Research, the FP6 NODE (015783) project, the ministry of economic affairs in the Netherlands (NanoNed) and the European Marie Curie program.

5.5 Appendix InP and GaP superlattices

As shown in figure 5.5 the same trend is observed for InP (data from chapter 4) as well as GaP superlattices. Our model, describing the twin superlattice formation, is capable of fitting both materials. Different surface and twin energies are used to fit the data.

References

[1] A. Boukai, Y. Bunimovich, J. Tahir-Kheli, J.-K. Yu, W. Goddard, and J. Heath, "Silicon nanowires as efficient thermoelectric materials," *Nature*, vol. 451, pp. 168–171, 2008.

[2] A. Hochbaum, R. Chen, R. Delgado, W. Liang, E. Garnett, M. Najarian, A. Majumdar, and P. Yang, "Enhanced thermoelectric performance of rough silicon nanowires," *Nature*, vol. 451, pp. 163–168, 2008.

[3] J. Bao, D. Bell, F. Capasso, J. Wagner, T. Mårtensson, J. Trägårdh, and L. Samuelson, "Optical properties of rotationally twinned InP nanowire heterostructures," *Nano Lett.*, vol. 8, pp. 836–841, 2008.

[4] R. Algra, M. Verheijen, M. Borgström, L. Feiner, G. Immink, W. van Enckevort, E.Vlieg, and E. Bakkers, "Twinning superlattices in indium phosphide nanowires," *Nature*, vol. 456, pp. 369–372, 2008.

[5] P. Caroff, K. Dick, J. Johansson, M. Messing, K. Deppert, and L. Samuelson, "Controlled polytypic and twin plane superlattices in III-V nanowires," *Nature Nanotechnology*, vol. 4, pp. 50–55, 2008.

[6] M. Verheijen, R. Algra, M. Borgström, G. Immink, E. Sourty, W. van Enckevort, E. Vlieg, and E. Bakkers, "Three dimensional morphology of GaP-GaAs nanowires revealed by transmission electron microscopy tomography.," *Nano Lett.*, vol. 7, pp. 3051–3055, 2007.

[7] M. Borgström, G. Immink, B. Ketelaars, R. Algra, and E. Bakkers, "Synergetic nanowire growth," *Nature Nanotechnology*, vol. 2, pp. 541–544, 2007.

[8] K. Pemasiri, M. Montazeri, R. Gass, L. Smith, H. Jackson, J. Yarrison-Rice, S. Paiman, Q. Gao, H. Tan, C. Jagadish, X. Zhang, and J. Zou, "Carrier dynamics and quantum confinement in type II ZB-WZ InP nanowire homostructures," *Nano Lett.*, vol. 9, pp. 648–654, 2009.

[9] M. Mattila, T. Hakkarainen, M. Mulot, and H. Lipsanen, "Crystal-structure-dependent photoluminescence from InP nanowires," *Nanotechnology*, vol. 17, pp. 1580–158, 2006.

[10] K. Dick, S. Kodambaka, M. Reuter, K. Deppert, L. Samuelson, W. Seifert, L. Wallenberg, and F. Ross, "The morphology of axial and branched nanowires hetereostructures," *Nano Lett.*, vol. 7, p. 1817, 2007.

[11] F. Glas, J. Harmand, and G. Patriarche, "Why does Wurtzite form in nanowires of III-V Zinc Blende semiconductors? ," *Phys. Rev. Lett.*, vol. 99, p. 146101, 2007.

[12] T. Akiyama, K. Sano, K. Nakamura, and T. Ito, "An empirical potential approach to wurtzite- zinc-blende polytypism in group III-V semiconducting nanowires.," *J. J. Appl. Phys.*, vol. 45, pp. L275–L278, 2006.

[13] H. Joyce, J. Wong-Leung, Q. Gao, H. Tan, and C. Jagadish, "Phase Perfection in Zinc Blende and Wurtzite III-V Nanowires Using Basic Growth Parameters," *Nano Lett.*, vol. 10, pp. 908–915, 2010.

[14] M. A. Verheijen, G. Immink, T. de Smet, M. T. Borgstrom, and E. P. A. M. Bakkers, "Growth Kinetics of Heterostructured GaP-GaAs Nanowires.," *J. Am. Chem. Soc.*, vol. 128, pp. 1353–1359, 2006.

[15] R. Algra, V. Vonk, D. Wermeille, W. Noorduin, F. Bruele, A. Bode, E. Tancini, A. D. Jong, W. Szweryn, M. Verheijen, E. Bakkers, W. v. Enckevort, and E. Vlieg, "Pre-ordering at the liquid-solid AuIn-InP interface during nanowire growth," *submitted to Nano Lett.*, 2010.

[16] W. van Enckevort, "Een inleiding in kristalgroei," *Dictaat Kristalgroei*, 2009.

Chapter 6

Formation of wurtzite InP nanowires explained by liquid-ordering

Rienk E. Algra, Vedran Vonk, Wiesiek J. Szweryn, Didier Wermeille, Marcel A. Verheijen, Willem J.P. v. Enckevort, Arno A.C. Bode, Wim L. Noorduin, Aryan E.F. de Jong, Erik Tancini, Erik P. A. M. Bakkers, Elias Vlieg.

We report an *in-situ* surface X-ray diffraction study of liquid AuIn metal alloys in contact with zinc-blende InP $(111)_B$ substrates at elevated temperatures. We observe strong layering of the liquid metal alloy in the first three atomic layers in contact with the substrate. The first atomic layer of the alloy has a higher indium concentration than in the bulk. In addition, in this first layer we find evidence for in-plane ordering at stacking fault positions. This can explain the typical formation of the wurtzite crystal structure in InP nanowires grown from AuIn metal particles. The strong layering and in-plane ordering have implications for the diffusion of precursor material through the metal particle at the growth interface during nanowire growth.

This chapter has been submitted

6.1 Introduction

Nanowires can be grown from nano-sized metal droplets by the Vapor-Liquid-Solid (VLS) growth mechanism, which was first reported by Wagner and Ellis already in 1964 [1]. As the name 'vapor-liquid-solid' suggests, three phases are involved in this type of nanowire growth [2]. Precursor molecules from the gas phase are decomposed and form an alloy with the metal particle. At the solid-liquid interface nucleation occurs and the crystalline nanowire grows layer by layer. The crystal structure of nanowires grown by the VLS mechanism is often different from corresponding bulk crystals [3, 4]. For instance, intrinsic InP nanowires crystallize in the wurtzite structure, while bulk grown InP crystals have the zinc-blende structure. The metal alloy positioned on top of the nanowires is typical for the VLS growth and has many functions. It has been argued that the shape of the metal particle, and more specifically the contact angle of the droplet with the nanowire side facets determines the nanowire crystal structure [3, 5]. In previous work [4], we have suggested that not the particle shape, but the chemical composition and the precise atomic positions at the solid-liquid interface determine the nanowire crystal structure. In this paper, we use Surface X-Ray Diffraction (SXRD) in order to solve *in-situ* the atomic structure at the liquid-solid interface of an AuIn alloy in contact with a $(111)_B$ InP bulk crystal surface at elevated temperatures, simulating the solid-liquid interface during InP nanowire growth from an initial Au particle.
A closely related issue that we will address in this paper, is on the physical state of the alloy particle during nanowire growth. Nanowires are often grown below the eutectic temperature of the specific alloy. Several studies have shown that the particle is in the solid state during growth [6], whereas others have shown that the growth rate is much lower for solid than for liquid particles [7]. We show by using SXRD that while the bulk of the alloy layer is in the liquid phase, the first three layers closest to the InP substrate are layered in the substrate normal direction, suggesting a 'quasi-solid' interface layer. The first layer, in direct contact with the substrate, is enriched with In atoms and shows in-plane ordering. The In atoms preferably occupy stacking fault positions, which induce the formation of the wurtzite InP crystal structure.

6.2 Experimental

Studying the solid-liquid interface of genuine nanowires in-situ encounters two major problems. First, the actual area covered by nanowires is quite small and

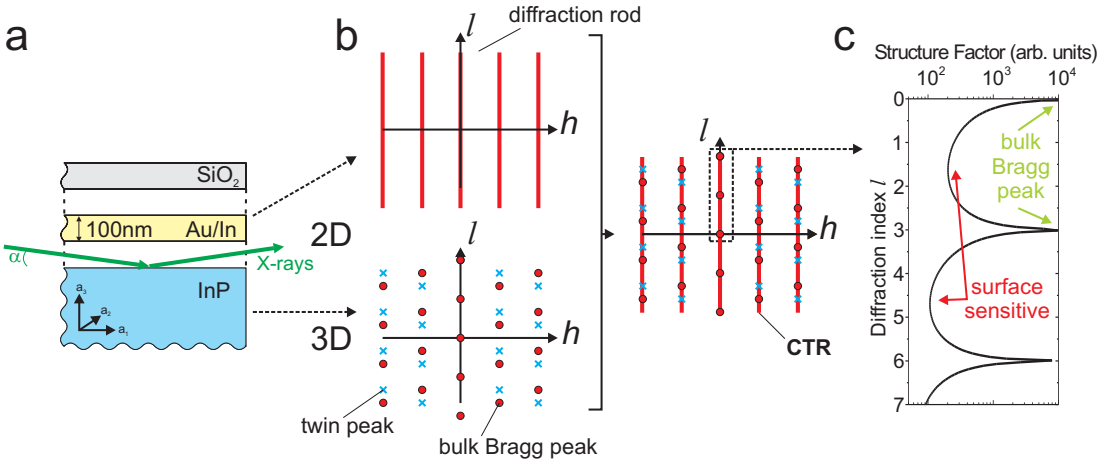

Figure 6.1: Surface X-Ray Diffraction (a) A schematic representation of the sample layout. A $[111]_B$ oriented zinc-blende InP wafer is used, followed by a 100 nm thick layer of simultaneously evaporated Au/In alloy (60:40). The metal layer is covered by a SiO_2 layer of 100 nm to minimize decomposition of the InP by evaporation of phosphor. The scattering geometry during SXRD measurements was typically in grazing incidence mode, indicated by the angle α. **(b)** Diffraction pattern in reciprocal space for a 2D layer resulting in "diffraction rods" (top) and for a 3D bulk crystal resulting in "Bragg peaks" (bottom, red dots). Twin peaks are shown as blue crosses, which are the mirror positions of the Bragg peaks around l. If the solid-liquid interface is probed by X-rays, the combination results in Crystal Truncation Rods (CTRs). **(c)** A CTR gives surface sensitive information in between the bulk Bragg peaks.

second, it requires growth conditions with highly toxic precursor gasses. We therefore use a thin alloy film in contact with an InP $(111)_B$ substrate as a model system. The samples consist of triangular pieces, with 5-8 mm sides, of a $[111]_B$ oriented zinc-blende InP wafer. Here the terminology 'B' stands for a phosphor terminated surface. The substrate is covered by a 100 nm metal layer, which is obtained by simultaneous evaporation of Au and In, resulting in a binary composition with a ratio of 60:40, which was verified with EDX (Energy Dispersive X-ray) in a SEM (Scanning Electron Microscope). This ratio corresponds to the eutectic composition of the AuIn alloy (ϕ phase) at a temperature of 727K [8]. The sample lay-out is shown in figure 6.1a. The SXRD experiments are performed in a vacuum chamber (10^{-5} mbar), thus without a PH_3 background pressure. To minimize the decomposition of the InP substrate by phosphor desorption during heating, a 100 nm SiO_2 layer was deposited on top as a diffusion barrier. The samples are resistively heated to 773K in order to liquefy the AuIn alloy, similar to the annealing steps prior to nanowire growth. Next, the samples were cooled

down to 693K, a typical growth temperature for InP nanowire growth [4, 9, 10]. Although this is below the eutectic temperature of the ϕ phase, nanowires are grown at these temperatures with a typical rate of several nm/sec, indicating that the particles are in the liquid state [4, 10–14].
The X-rays probe the periodicity of the bulk InP crystal (3D) and give rise to Bragg peaks in reciprocal space, figure 6.1b, at integer diffraction indices (hkl). A perfect 2D layer, on the other hand, has no periodicity in the normal direction and therefore diffraction occurs along rods in reciprocal space for all l values. The combined diffraction from the 2D layer and 3D bulk crystal is called a Crystal Truncation Rod (CTR) [15]. By measuring the scattered intensities along the CTRs the amplitude of the structure factors (Fourier transform of the electron density of the unit cell) can be found, see figure 6.1c. From these structure factors the atomic positions and electron density of the interfacial atoms can be derived. The surface sensitive information thus can be found in the CTRs in between the bulk Bragg peaks, as indicated in figure 6.1c.
The SXRD experiments were performed at the ID03 beamline [16, 17] of the European Synchrotron Radiation Facility (ESRF), Grenoble, using an X-ray energy of 27.5 keV. At the solid-liquid interface, it is expected that the atomic ordering decreases from being completely ordered in the substrate to completely disordered in the liquid. The technique of SXRD is only sensitive to the ordered part of the interface and gives information about the gradual decrease of atomic ordering in the z-direction [18], which is perpendicular to the surface. In order to describe our results, we use a surface unit cell, which is defined in terms of the InP bulk cubic unit cell as $a_1 = \frac{1}{2}\,[1\bar{1}0]$, $a_2 = \frac{1}{2}\,[\bar{1}10]$ and $a_3 = [111]$. According to convention, h and k lie in the surface plane and l is along the surface normal. The integrated intensity of different (hkl) reflections is determined from rocking scans. After applying the appropriate correction factors [19], structure factor amplitudes are derived. We used the ANA-ROD package [20] to analyze the data.

6.3 Results

6.3.1 Specular

At 693K the specular (0,0,l) and the in-plane (1,0,l) rods were measured as shown in figure 6.2. At room temperature, the (0,0,l) rod shows powder diffraction peaks from the solid metal alloy film. The absence of these peaks at 693K proves that the alloy is liquid. The specular (0,0,l) rod contains information about the atomic ordering in the z-direction. At $l = 4.3$, the data reveals a broad peak

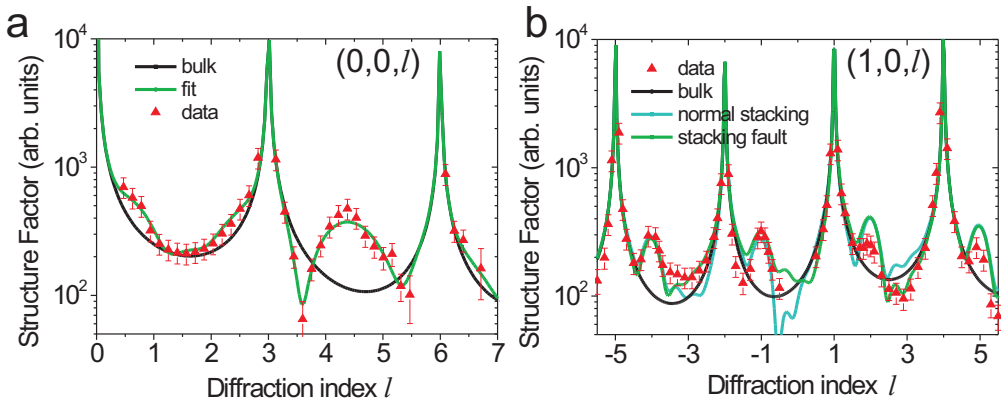

Figure 6.2: Experimental structure factors Experimental structure factors (red triangles) derived from measured scattered intensities along the **(a)** (0,0,l) rod and **(b)** (1,0,l) rod of the $\{111\}_B$ InP-AuIn solid-liquid interface at a temperature of 693 K . The solid black lines represent the calculated CTRs of a bulk terminated InP crystal. The blue and green curves represent a normal (continuing the bulk structure) and twinned stacking for the first liquid layer, respectively.

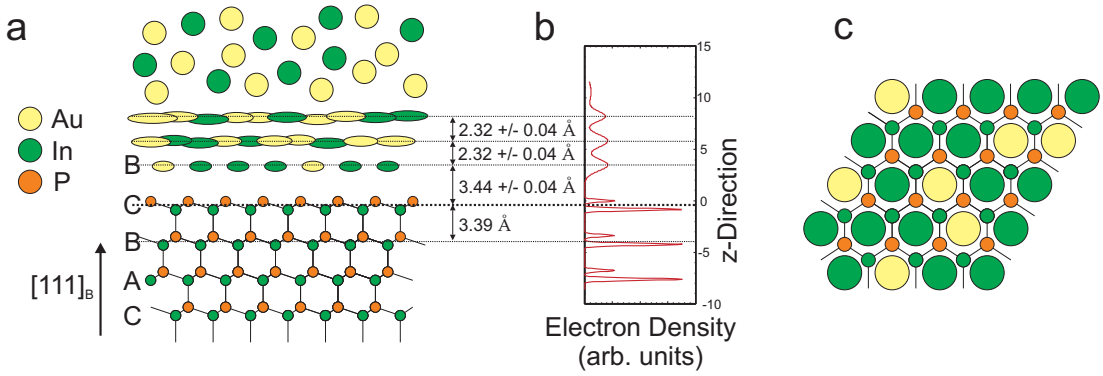

Figure 6.3: Layering (a) Schematic atomic structure of the solid-liquid interface accompanied by the corresponding z-projected electron density distribution **(b)**. The different atoms are represented in green (In), orange (P) and yellow (Au). The elliptic shapes symbolize the anisotropic in- and out-of-plane liquid ordering whereas the bulk liquid is characterized by larger spheres. **(c)** Top-view image of the stacking of the first liquid layer at the wurtzite "B" position on top of a zinc-blende ABC bulk InP structure, indicating that the atoms are positioned in hexagonal rings, at the wurtzite position. The larger spheres represent the in-plane ordering of the atoms in the first liquid layer. The accompanying Debye-Waller parameters are given in table 6.4.

(red triangles), which is absent in bulk terminated InP (solid black line). From the position, width and height of the peak at $l = 4.3$, we find that 3 to 4 atomic layers with a spacing of approximately 2.3 Angstrom, contribute to this broad peak. To describe the solid-liquid interface a model was used consisting of a liquid of n atomic layers with a constant spacing and an offset with respect to the substrate surface (fig. 6.3a). Each layer, having the composition of the ϕ phase, has an occupancy and an anisotropic Debye-Waller factor to define the degree of ordering. The test model uses a phosphor terminated zinc-blende structure to model the crystalline InP at the interface. More refined models, with varying spacings and atom types, did not give an improved fit, hence this simple model is sufficient to describe the current experimental data.

Fitting of the model to the (0,0,l) rod confirms the layering in the z-direction: three layers show a strong perpendicular order, a fourth only a little. Subsequent layers are invisible, and thus have a bulk liquid structure. The fit is shown in figure 6.2a, the corresponding structure in figure 6.3. The first layer is positioned at 3.44 $\pm$ 0.04 Angstrom from the InP surface, approximately at the position where the next In-layer of the bulk InP is expected. We find that the spacing between subsequent layers is 2.32 $\pm$ 0.04 Angstrom.

The first atomic layer in the liquid is expected to be ordered the most, due to its strongest interaction with the substrate. Each next layer should be less ordered. This results in a decrease of the occupancies of the ordered positions with each next layer, and thus in a decrease in the measured electron density. However, from the fit results it can be seen that the electron densities (see figure 6.3b) are almost equal for the first three layers.

This observed layering is rather uncommon compared to other solid-liquid interfaces reported in the literature, where normally the ordering decreases rapidly after the first layer [18, 21–23]. Usually the ordering decreases exponentially. The fact that here the first three layers show an equal electron density, suggests an unusual step function after three layers. Simulations of exponential segregation and ordering profiles (not shown here) lead to a specular rod profile without any signs of the finite thickness oscillations, that *are* visible in the data at the fringes for l values around 0.8 and 2.2 in figure 6.2a. Such oscillations are characteristic for density profiles which contain abrupt steps. Therefore, the density and/or segregation profile at the present interface must contain an abrupt decrease after about three atomic layers. It should be realized that the system is thermodynamically very close to an ordered solid phase (ϕ phase) [8], which could induce the observed strong layering. The three layers are quasi-liquid and not solid, because

	Au:In ratio	Occupancy	DW in-plane (Å^2)	DW out-plane (Å^2)	Spacing (Å)
Layer 1	60:40 30:70	0.86 +/- 0.09 1.00	70 +/- 10	30 +/- 10	3.44 +/- 0.04
Layer 2	60:40	0.99 +/- 0.07	∞	30 +/- 10	2.32 +/- 0.04
Layer 3	60:40	0.65 +/- 0.07	∞	30 +/- 10	2.32 +/- 0.04
Layer 4	60:40	0.75 +/- 0.13	∞	180 +/- 40	2.32 +/- 0.04

Figure 6.4: Fit parameters The optimum in- and out- of plane parameters are given for each ordered layer, starting with the layer closest to the substrate. The occupancies of ordered atoms in the ϕ phase (60:40 AuIn) are given and the degree of ordering is shown by the Debye-Waller parameters. The spacing is defined as the distance between two successive layers in the liquid alloy. For layer 1, also the composition corresponding to an occupancy of 1 is shown.

that would result in much lower Debye-Waller parameters **.

The spacing of 2.32 Angstrom in the quasi-liquid layer matches d_{110} of bulk In, d_{111} of Au and d_{102} of the ϕ phase, suggesting that all corresponding layer compositions are plausible. With X-rays, the electron densities are probed, which makes it difficult to distinguish between different types of atoms. Indeed, using models with layers of pure Au, In or combinations of these atoms, always resulted in the same electron density profile. Figure 6.4 lists the parameters assuming the layers have a 60:40 Au:In composition. The occupancy of the first layer is found to be lower than the second one. This is unlikely. If the first layer is enriched with In, a lighter element than Au, the fitted occupancy increases. An occupancy of 1, corresponds to a Au:In composition of 30:70. It is known that the surface tension of liquid In is a factor 2 lower [24] than that of Au [25]. It is plausible that also at the present solid-liquid interface the interface free energy of In will be lower than that of Au, the more so since the substrate itself contains In and the first alloy layer is positioned at the next InP bulk position. These arguments all indicate an In-rich solid-liquid interface, containing approximately 70% In in the first layer.

** It is also known from temperature-dependent nanowire growth investigations that at temperatures lower than the 693 K reported here the growth velocities become as low as is expected for Vapor-Solid-Solid (VSS) growth [7].

6.3.2 In-plane ordering

The (1,0,l) rod, shown in figure 6.2b, contains information about in-plane ordering. Besides the bulk Bragg peaks at l equals -5,-2,1 and 4, additionally smaller but significant peaks are found at l values of exactly -4,-1,2 and 5. These peaks correspond to twinned InP islands on the surface with a surface coverage of about 5%. Important to note is that these twinned features are absent before heating and appeared during the measurements after roughly one hour at elevated temperature. The twin peaks become more pronounced in time, but during the total data collection never covered more than 10% of the surface [26].

By comparing the CTR from bulk-terminated InP (black line) with the measured data (red triangles), we find that at l values around +3 and -3 there are clear systematic deviations. Around $l = 3$ the scattered intensity is somewhat lower than what would be expected and around $l =$ -3 somewhat higher. The deviations indicate that some degree of in-plane ordering is present in the first layer of the liquid. From fitting different models, we find that only the first layer shows such ordering. If all the atoms in the quasi-liquid layer would show strong in-plane ordering, the (1,0,l) rod should, just as the specular one, also show a broad diffraction feature, which is absent. The other layers can therefore be described using an 'infinitely' large in-plane Debye-Waller parameter.

If we now consider in-plane ordering of the first layer atoms in the metal alloy, they can be located at two positions on top of the zinc-blende substrate, which has an ABC stacking. Starting from the zinc-blende C layer, the first layer can be at an 'A' position (continued zinc-blende bulk, which gives ABC**A**) or a 'B' position (wurtzite position, which gives ABC**B**), indicated in figure 6.3a. Two model calculations are shown in figure 6.2 with the first layer at the wurtzite (green) and zinc-blende position (blue). By comparing the calculated rod profiles for these stacking possibilities we find that the asymmetry is reproduced only by placing the atom in the first layer of the quasi-liquid at the 'B' wurtzite InP position. The atoms are thus preferentially located in the center of the hexagonal rings, the wurtzite position, as shown in figure 6.3c. In other words, the atoms in the first liquid layer occupy positions that would facilitate the growth of a twinned zinc-blende or a wurtzite crystal structure. We argue therefore that the particular preferential in-plane ordering of the In atoms in the quasi-liquid can explain the fact that VLS-grown InP nanowires crystallize in the metastable wurtzite structure instead of the stable zinc-blende structure.

The data presented here indicate that close to the interface a strong ordering occurs in the z-direction, manifested by layering, as well as preferential in-plane

ordering. The formation of a quasi-liquid on top of the substrate surface will have a major impact on the growth behavior. At the free surface of SiAu alloys close to their eutectic composition, even a layering of 7 layers is found [27], which is accompanied by the formation of a solid 2D surface alloy. It could be that the driving force which is responsible for the crystallization of the alloy layer, at temperatures close to the eutectic point, induces the strong layering. Due to the strong layering we argue that the growth mechanism is more complex than simply VLS, and in principle should be described by a "Vapor-*Quasi*Liquid-Solid (VQLS)" growth. Interfacial ordering is expected to have a large influence on the crystal growth, most notably on the growth rate. Pre-ordering towards a solid phase will affect the mass-transport through the droplet and thereby the growth dynamics, such as the nanowire growth rate. For other materials systems the alloy compositions could have a different pre-ordering at the growth interface and possibly lead to other preferential crystal structures. This could be the case for GaP, which exhibits the zinc-blende crystal structure for nanowires grown by a AuGa alloy [11, 14] awhich is the same as for bulk-grown crystals.

6.4 Conclusions

In summary, we have shown that the first three atomic layers of the liquid AuIn metal alloy are strongly layered and that the first of these atomic layers shows in-plane ordering with the periodicity of the underlying substrate. This quasi-liquid structure will have clear consequences for the mass transport during nanowire growth at this interface. The first layer, closest to the P-terminated InP substrate interface, is likely an In rich layer and contains approximately 70% In, compared to 40% in the bulk of the liquid. From the in-plane ordering we find evidence for a preferential positioning of the first atomic layer at stacking fault substrate positions. These positions coincide with the wurtzite crystal structure positions and the liquid can therefore induce the formation of wurtzite InP nanowires.

6.5 Vacuum chamber

The experimental setup is used to perform SXRD experiments at elevated temperatures is shown in figure 6.5. The sample is placed on a heater, capable of reaching temperatures up to 1200 K, and placed in a vacuum chamber to minimize

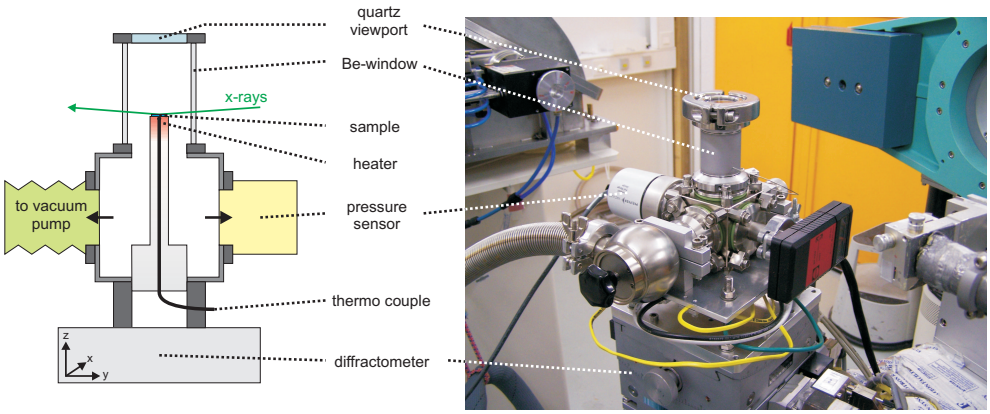

Figure 6.5: Experimental setup Schematic representation of the sample chamber for surface X-ray diffraction. The sample is placed on a 1 inch heater in a vacuum chamber, which is pumped down to 10^{-5} mbar. The samples were glued directly on to the heater with a special two-component high temperature adhesive (CERASTILE-C7). To allow for good X-ray penetration the cylindrical tube surrounding the sample is made from Beryllium. A thermocouple is mounted directly under the surface of the heater to measure the sample temperature. The photograph shows the complete sample chamber placed on the diffractometer of beamline ID03 at the ESRF.

thermal conduction. A Beryllium cylinder surrounds the sample area, to allow for minimal losses in X-ray intensity. The cylinder is closed with a quartz window to visually inspect the sample. The complete vacuum chamber is mounted on the diffractometer of beamline ID03 at the ESRF, Grenoble.

6.6 Acknowledgements

This research was carried out under project number MC3.05243 in the framework of the strategic research program of the Materials Innovation Institute (M2i) (www.M2i.nl), the former Netherlands Institute of Metals Research, the FP6 NODE (015783) project, the ministry of economic affairs in the Netherlands (NanoNed) and the European Marie Curie program. The authors would like to thank E. van Thiel for the deposition of metal alloys, H. Wondergem for ex-situ XRD measurements and H. de Barse for SEM imaging. Correspondence should be addressed to E. Vlieg.

References

[1] R. Wagner and W. Ellis, "Vapor-Liquid-Solid mechanism of single crystal growth," *Applied Physics Letters*, vol. 4, pp. 89–90, 1964.

[2] M. A. Verheijen, G. Immink, T. de Smet, M. T. Borgstrom, and E. P. A. M. Bakkers, "Growth Kinetics of Heterostructured GaP-GaAs Nanowires.," *J. Am. Chem. Soc.*, vol. 128, pp. 1353–1359, 2006.

[3] H. Joyce, J. Wong-Leung, Q. Gao, H. Tan, and C. Jagadish, "Phase Perfection in Zinc Blende and Wurtzite III-V Nanowires Using Basic Growth Parameters," *Nano Lett.*, vol. 10, pp. 908–915, 2010.

[4] R. Algra, M. Verheijen, M. Borgström, L. Feiner, G. Immink, W. van Enckevort, E.Vlieg, and E. Bakkers, "Twinning superlattices in indium phosphide nanowires," *Nature*, vol. 456, pp. 369–372, 2008.

[5] F. Glas, J. Harmand, and G. Patriarche, "Why does Wurtzite form in nanowires of III-V Zinc Blende semiconductors? ," *Phys. Rev. Lett.*, vol. 99, p. 146101, 2007.

[6] B. S. Sorensen, M. Aagesen, C. B. Sorensen, P. E. Lindelof, K. L. Martinez, and J. Nygård, "Ambipolar transistor behavior in p-doped InAs nanowires grown by molecular beam epitaxy," *Appl. Phys. Lett.*, vol. 92, p. 012119, 2008.

[7] S. Kodambaka, J. Tersoff, M. C. Reuter, and F. M. Ross, "Germanium Nanowire Growth Below the Eutectic Temperature," *Science*, vol. 316, pp. 720–732, 2007.

[8] Landolt-Bornstein, *New Series IV/5a*.

[9] K. Dick, S. Kodambaka, M. Reuter, K. Deppert, L. Samuelson, W. Seifert, L. Wallenberg, and F. Ross, "The Morphology of Axial and Branched Nanowire Heterostructures," *Nano lett.*, vol. 7, pp. 1817–1822, 2007.

[10] E. Bakkers and M. A. Verheijen, "Synthesis of InP nanotubes," *J. Am. Chem. Soc.*, p. 3440, 2003.

[11] M. Verheijen, R. Algra, M. Borgström, G. Immink, E. Sourty, W. van Enckevort, E. Vlieg, and E. Bakkers, "Three dimensional morphology of GaP-GaAs nanowires revealed by transmission electron microscopy tomography.," *Nano Lett.*, vol. 7, pp. 3051–3055, 2007.

[12] K. Dick, S. Kodambaka, M. Reuter, K. Deppert, L. Samuelson, W. Seifert, L. Wallenberg, and F. Ross, "The morphology of axial and branched nanowires hetereostructures," *Nano Lett.*, vol. 7, p. 1817, 2007.

[13] M. Borgström, G. Immink, B. Ketelaars, R. Algra, and E. Bakkers, "Synergetic nanowire growth," *Nature Nanotechnology*, vol. 2, pp. 541–544, 2007.

[14] J. Johansson, L. S. Karlsson, C. Patrik, T. Svensson, T. Mårtensson, B. A. Wacaser, K. Deppert, L. Samuelson, and W. Seifert, "Structural properties of $(111)_B$-oriented III-V nanowires.," *Nat. Materials*, vol. 5, pp. 574–580, 2006.

[15] I. Robinson, "Crystal truncation rods and surface roughness," *Phys. Rev. B*, vol. 33, p. 38303836, 1986.

[16] S. Ferrer and F. Comin, "Surface diffraction beamline ESRF," *Rev.Sci. Instrum.*, vol. 66, p. 1674, 1995.

[17] O. Balmes, R. Rijnand, D. Wermeilleand, A. Restaand, L. Petitand, H. Isernand, T. Dufraneand, and R. Felici, "The ID03 surface diffraction beamline for in-situ and real time x-ray investigations of catalytic reactions and surfaces," *Catalysis Today*, vol. 145, pp. 220–226, 2009.

[18] M. Reedijk, J. Arsic, F. Hollander, S. de Vries, and E. Vlieg, "Liquid order at the interface of KDP crystals with water: Evidence for icelike layers.," *Phys. Rev. Lett.*, vol. 90, p. 066103, 2003.

[19] E. Vlieg, "Integrated Intensities Using a Six-Circle Surface X-ray Diffractometer," *J. Appl. Cryst.*, vol. 30, pp. 532–543, 1997.

[20] E. Vlieg, "ROD: a program for surface X-ray crystallography," *J. Appl. Cryst.*, vol. 401-405, p. 33, 2000.

[21] D. Kaminski, N. Radenovic, M. Deij, W. v. Enckevort, and E. Vlieg, "pH-dependent liquid order at the solid-solution interface of KH_2PO_4 crystals," *Phys Rev. B*, vol. 72, p. 245404, 2005.

[22] J. Arsic, D. Kaminski, P. Poodt, and E. Vlieg, "Liquid ordering at the Brushite-{010}water interface," *Phys. Rev. B*, vol. 69, p. 245406, 2004.

[23] W. Huisman, J. Peters, M. Zwanenburg, S. de Vries, T. Derry, D. Abernathy, and J. van der Veen, "Layering of a liquid metal in contact with a hard wall," *Nature*, vol. 390, pp. 379–381, 1997.

[24] M. McClelland and J. Sze, "Surface tension and density measurements for indium and uranium using sessile-drop apparatus with glow discharge cleaning," *Surf. Sci.*, vol. 330, p. 313, 1995.

[25] J. Lee, M. Nakamoto, and T. Tanaka, "Thermodynamic study on the melting of nanometer-sized gold particles on graphite substrate," *J. Mat. Sci.*, vol. 40, p. 2167, 2005.

[26] "For unknown reasons, re-crystallization at the interface occurs, due to some kind of surface restructuring, leaving InP islands of which a fraction is twinned. Although these unwanted twinned InP islands could not be prevented and were present on all the samples investigated, their relatively low coverage (<10 percent) does not influence the data analysis strongly. Indeed, the Bragg reflections of these twinned islands are found to contribute significantly only in a confined region ($\Delta l \approx 0.5$) and do not influence the scattering further away along the CTR's. In the (0,0,l) specular reflection twinning is not observed, because the z-direction is not sensitive to in-plane rotational twins. The twinned islands are modeled by a 2 unit cells (6 monolayers) high layer with a surface coverage of 5 percent.,"

[27] O. Shpyrko, R. Streitel, V. Balagurusamy, A. Grigoriev, M. Deutsch, B. Ocko, M. Meron, B. Lin, and P. Pershan, "Surface Crystallization in a Liquid AuSi Alloy," *Science*, vol. 313, p. 77, 2006.

Chapter 7

Generic nano-imprint process for fabrication of nanowire arrays

Aurelie Pierret, Moïra Hocevar, Silke L. Diedenhofen, Rienk E. Algra, E. Vlieg, Eugene C. Timmering, Marc A. Verschuuren, George W.G. Immink, Marcel A. Verheijen, Erik P.A.M. Bakkers

A generic process has been developed to grow nearly defect free arrays of (heterostructured) InP and GaP nanowires. Soft nanoimprint lithography has been used to pattern gold particle arrays on full 2 inch substrates. After lift-off organic residues remain on the surface, which induce the growth of additional undesired nanowires. We show that cleaning of the samples before growth with piranha solution in combination with a thermal anneal at 550 °C for InP and 700 °C for GaP results in uniform nanowire arrays with 1% variation in nanowire length, and without undesired extra nanowires. Our chemical cleaning procedure is applicable to other lithographic techniques such as e-beam lithography, and therefore represents a generic process.

This chapter has been published in *Nanotechnology 21, p.065305* 2010

7.1 Introduction

Semiconductor nanowires (NWs) have been intensely studied because of their highly tuneable optical and electrical properties. They have been employed as functional elements in light emitting diodes (LEDs) [1, 2], transistors [3], and antireflection coatings [4]. The Vapor-Liquid-Solid (VLS) bottom-up growth process [5] allows growing (radial) core/shell structures or (axial) quantum dot heterostructures [6]. A metal nanoparticle is used as catalyst for nanowire growth, and can be deposited via spin coating from a colloidal solution, spraying an aerosol solution, or by deposition of a thin film, which will break up by heating the sample. However, the density and position of the nanowires are not controlled using these approaches. We have previously observed [7] that the nanowire growth rate sensitively depends on the density and the dimensions of the gold particles. Such a variation of the growth rate can result in non uniform optical or electrical properties. It is likely that, for instance, the dispersion of the electron mobility in InAs/InP core-shell nanowires [8], is related to the large spread in shell thickness of these nanowires grown from randomly deposited colloidal gold particles. Besides the axial growth rate, most probably also the radial (shell) growth is affected by the catalyst density. Hence, in order to improve the nanowire uniformity, it is important to control the position and density of the catalyst particles on the substrate. Different approaches have already been reported, such as e-beam lithography [9–11], gold deposition through an anodic aluminium oxide template [12] and nanosphere lithography [13]. In general, these techniques do not allow for large-area structuring because of either high cost or lack of long range order. Alternatively, nanoimprint lithography [14] has been reported to define nanowire positions. This technique enables patterning of large surface areas at relatively low-cost. However, this process has not been fully optimised and extra undesired nanowires were obtained. It has been shown that nanowire growth can be nucleated by organic molecules [15] and the undesired nanowires probably origin from organic residues from the photoresist.

We have developed and optimized a wafer scale soft nano-imprint method, called Substrate Conformal Imprint Lithography (SCIL) to control the position of InP and GaP nanowires. In order to fabricate uniform, defect free nanowire arrays we have systematically studied the effect on nanowire growth of chemical and thermal treatment of the substrate which contained gold catalyst particles. These treatments were focused on the removal of organic residues from the photoresist layer. The process has been further optimized by adjusting the gold layer thickness. Finally, the quality of the grown nanowire material has been evaluated by optical characterization on InAsP quantum dots in InP nanowires.

7.2 Experimental details

Our substrate conformal imprint lithography method makes use of a flexible patterned stamp made from Poly-Di-Methyl-Siloxane (PDMS) [14] which is molded from a silicon master pattern which contained arrays of holes and was fabricated using e-beam lithography. The composite stamp is molded from the master following the procedure described in [16, 17] which yields a two layer soft PDMS stamp with protruding pillars. The developed nano-imprint and lift-off process has the following steps. A ∼100 nm thick layer of Poly-Methyl-Meth-Acrylat (PMMA) is applied by spin coating on full 2 inch annealed $(111)_B$ InP or freshly etched $(111)_B$ GaP wafers, after which the wafers with the PMMA layer are baked on a hotplate at 150 °C for 15 minutes. Next, a precise amount of silica based sol-gel imprint resist is applied by spin coating over the PMMA layer [18]. Within two minutes after the spin coat process the stamp is applied in the still liquid sol-gel resist. The features in the stamp are filled by capillary forces with the sol-gel resist. The sol-gel reacts to form solid silica glass in about 20 minutes, where residual solvents and reaction products (alcohols and water) are absorbed in the PDMS rubber. Finally the stamp is carefully removed from the patterned silica layer by peeling. In this way the full 2" wafer area is patterned with an array of holes with a diameter of ∼100 nm. The ∼10 nm thick remaining residual sol-gel layer between the bottom of the features and the PMMA layer is removed by a CF_4 based reactive ion etch (RIE). Then oxygen RIE is used to transfer the pattern of the sol-gel layer into the underlying PMMA layer. The oxygen etch stops as the III-V material is reached and a short over etch is applied in order to remove any residual PMMA. A short etch in a 1% HF solution removes the formed Ga or In oxide, after which a thin (1-6 nm) gold layer is deposited onto the patterned sol-gel / PMMA pattern by perpendicular evaporation. The lift-off process is performed in acetone which dissolves the PMMA layer and releases the silica and gold metal which are suspended by PMMA. This leaves precisely placed gold dots of controlled diameter and thickness on the semiconductor material. In this work different stamps were used with 90 and 100 nm hole diameters on a corresponding pitch of 0.5 μm (tetragonal) and 1 μm (hexagonal).

The lift-off process leaves (organic) residues on the substrate besides the patterned metal particles. Various chemicals were tested to clean the substrate surface. We investigated the effect of fumic nitric acid (HNO_3), Piranha (H_2SO_4 : H_2O_2 : H_2O, 5:1:1), King's Water (HCl : HNO_3 : H_2O, 3:2:3) and (1 %) fluoric acid (HF) and bromine-methanol (Br_2 : MeOH, $1{:}10^3$ or $1{:}25{*}10^3$) on the NWs growth quality. After exposure to these chemicals at room temperature the samples were left in streaming deionized cold water for about 5 min.

The nanowires were synthesized in an Aixtron 200 Metal-Organic Vapour-Phase Epitaxy (MOVPE) reactor from Tri-Methyl-Gallium (TMGa) or Tri-Methyl-Indium (TMIn) for the group III elements and Phosphine (PH_3) for the group V-elements. For growth of an InAsP heterostructure, Arsine (AsH_3) was added. A thermal anneal was applied before nanowire growth for 10 minutes at different temperatures under a PH_3 flow. During the thermal anneal the gold droplets form a eutectic, Au-In or Au-Ga, depending on the substrate. The native oxide layer covering the samples, and residual organic materials are removed at annealing temperature exceeding 550 °C.
Scanning Electron Microscopy (SEM) images were obtained with a Philips XL 40 FEG system. NWs lengths and diameters were measured in these images by investigating 30 nanowires per array. The samples were studied with a Tecnai 300 keV TEM in both brightfield as well as in high-angle annular dark field (HAADF) mode. The chemical composition of the nanowires was studied using scanning TEM in combination with energy-dispersive X-ray analysis (EDX). Microphotoluminescence measurements on InAsP heterostructure nanowires transferred on SiO_2 substrates were performed at 4.2 K. The nanowire quantum dots were excited with a 532 nm continuous wave laser focused to a spot size of 0.6 μm using a microscope objective with a numerical aperture $NA = 0.85$.

7.3 Results and Discussion

Figure 7.1(a) shows a SEM image of the surface after the lift-off process without further treatment. We can clearly see the high fidelity of the pattern transfer, as the Au particles are arranged in an ordered pattern. However, extra material is present around the Au islands. EDX measurements, carried out with the SEM, show that these contaminants are carbon based residues from the PMMA layer. The nanowires are grown by MOVPE on $(111)_B$ oriented InP and GaP substrates, on which the Au particle arrays were patterned using SCIL. The SEM image in figure 7.1(b) is taken after InP nanowire growth. Besides nanowires grown from the predefined catalyst particles in a regular pattern, a lot of undesired thin nanowires are obtained. These extra nanowires arise if no or improper pretreatment was used after the lift-off. This shows that growth of these extra nanowires is initiated by the organic material observed in figure 7.1(a). An extra cleaning step is necessary to remove the organics prior to growth, but it should not change the III-V substrate surface chemistry [19], since nanowire growth rates sensitively depend on the surface diffusion of the precursor molecules [7, 10]. We have investigated the effect of the following wet chemical treatments on the

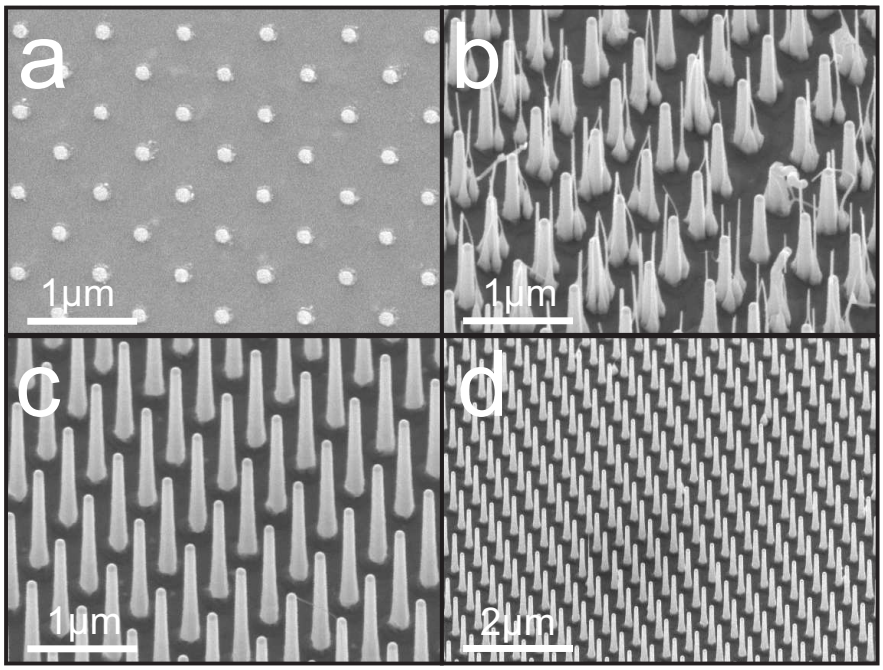

Figure 7.1: InP imprint. InP nanowire arrays by soft nano imprint lithography. **(a)** Pattern of Au dots after lift-off process, prior to the growth of nanowires. **(b)** Nanowire array without suitable cleaning step prior to growth resulting in extra "grass-like" wire growth between the patterned array. **(c)** and **(d)** Nanowire array with a piranha cleaning step and 550 °C anneal before growth.

quality of the nanowire growth: Fuming nitric acid, an acidic etchant, oxidizes InP and GaP. Piranha is a mixture that contains a very strong oxidizer which can remove organic residues. King's Water is a combination of a powerful oxidizer and strong acid, and Br_2/methanol is an electrochemical etchant for InP and GaP. After exposure to one of these solutions or a combination of them the samples were left in streaming deionized cold water for about 5 min. The results are summarized for InP and GaP in table 7.2 and table 7.3, respectively.

InP samples treated with King's Water, HNO_3, and (HNO_3+HF) show a large number of undesired nanowires around the intended nanowires. During the longer treatments with King's Water, the gold has been removed and only undesired nanowires were grown (see supplementary information figureS1). Samples exposed to a piranha solution at 20 °C show a very low density of undesired nanowire, as shown in figure 7.1c and d. (Almost) no undesired nanowires were obtained and all the nanowires grow at the predefined position. The overview SEM image in figure 7.1d shows that the InP nanowire dimensions are uniform across the sample and that just a few nanowires are missing. The obtained InP

Solution	Treatment time	InP nanowires		
		undesired	missing	misplaced
HNO_3	5 min	10 %	<1%	<1%
HNO_3+HF	5+1 min	14 %	<1%	7%
King's Water	5 sec	95%	1%	13%
Piranha	30 sec	2.5 %	<1%	<1%

Figure 7.2: InP treatment. Influence of different chemical treatments on the InP nanowire growth quality. The Au layer thickness was 6 nm in all cases. The samples have been annealed at 550 °C for InP just before growth. The percentage of defects (undesired, missing or misplaced nanowires) is determined from a large number (400-2000) of nanowires.

nanowires have an interspacing of 500 nm, as defined by the mold, and a length of 1761 ± 19 nm which is only a spread of 1.1%. Furthermore the nanowires are tapered and have a top diameter of 95 ± 4 nm and base diameter of 171 ± 4 nm. Important to note is that all InP samples presented in the table have been thermally annealed at 550 °C before growth. The effect of the anneal temperature will be discussed below.

GaP samples treated with Br_2/MeOH, (HNO_3 + Piranha), (Piranha+ HNO_3) or Piranha for 5 min show not only extra nanowires (due to inherent added contamination with each processing step) but also misplaced and/or missing nanowires. We believe that these chemicals can oxidize and/or etch the Au/GaP interface, which can result in removal of Au particles from the surface. We found that, similar to the results for InP wires, piranha treatment gives the best results [20], and the optimum treatment time for GaP wire growth is 1 minute. At shorter times more undesired NWs arise, but at longer times NWs tend to kink and some of them are missing, which is probably due to an overetching of the surface. The best results were obtained in combination with the higher anneal temperature of 700 °C. We will now show that an extra thermal anneal step is necessary to optimise the growth.

We have studied the effect of annealing temperature on the nanowire growth. The annealing was done after piranha treatment, but prior to the growth. It is well-known that a thermal anneal at high enough temperatures can remove In_2O_3 or Ga_2O_3 from the substrate surface [21]. To our best knowledge it is not known if the photoresist residues can be removed or react with the metal oxides by thermal treatment.

In figure 7.4 the effect of annealing on the growth of InP nanowires is shown.

Solution	Treatment time	GaP nanowires		
		undesired	missing	misplaced
10000 Br_2/MeOH	2 sec	100%	5%	65%
Piranha	5 min	104%	<1%	13%
Piranha	3 min	300%	<1%	<1%
Piranha	1 min	535%	<1%	<1%
Piranha	1 min*	6%	<1%	<1%
Piranha + HNO_3	1+5 min*	9%	<1%	6%
HNO_3 + Piranha	5+1 min*	5%	27%	15%

*annealing temperature at 700°C

Figure 7.3: GaP treatment. Influence of different chemical treatments on the GaP nanowire growth quality. The Au layer thickness was 6 nm in all cases. The samples have been annealed at 550 °C for GaP, but samples indicated with an * have been annealed at 700 ° C. The percentage of defects (undesired, missing or misplaced nanowires) is determined from a large number (400-2000) of nanowires.

Clearly, too low annealing temperatures, or no annealing at all results in undesired extra wire growth and irregular growth of the patterned nanowires (see figure 7.4a and b). An annealing temperature of at least 550 °C proves to be sufficient for defect free InP wire growth (figure 7.4c). At higher temperatures nanowires with a thicker base are obtained (figure 7.4d). Probably the surface chemistry changes at these temperatures and promote the lateral growth at the base of the nanowires. Similar results were obtained for the growth of GaP nanowires [20]. Whereas at an annealing temperature of 550 °C still undesired GaP nanowires are obtained, at a temperature of 700 °C the defect density is very low (see also table 7.3). The GaP nanowires show slight tapering, but do not have a thick base as observed for the InP nanowires when annealed at this temperature [20]. Growth without chemical cleaning but with an anneal step prior to growth resulted in many undesired nanowires. This shows that the combination of piranha treatment with a sufficiently high anneal temperature is essential for both InP and GaP wire growth. The different optimum annealing temperatures for InP and GaP shows that the removal process is substrate dependent and suggests that the metal oxides play an important role in removing the organic residues.

To define the pattern in our process, we have used PMMA in direct contact with the substrate surface. The organic contaminants, from which the undesired nanowires grow, are probably a product from the PMMA layer. Our cleaning

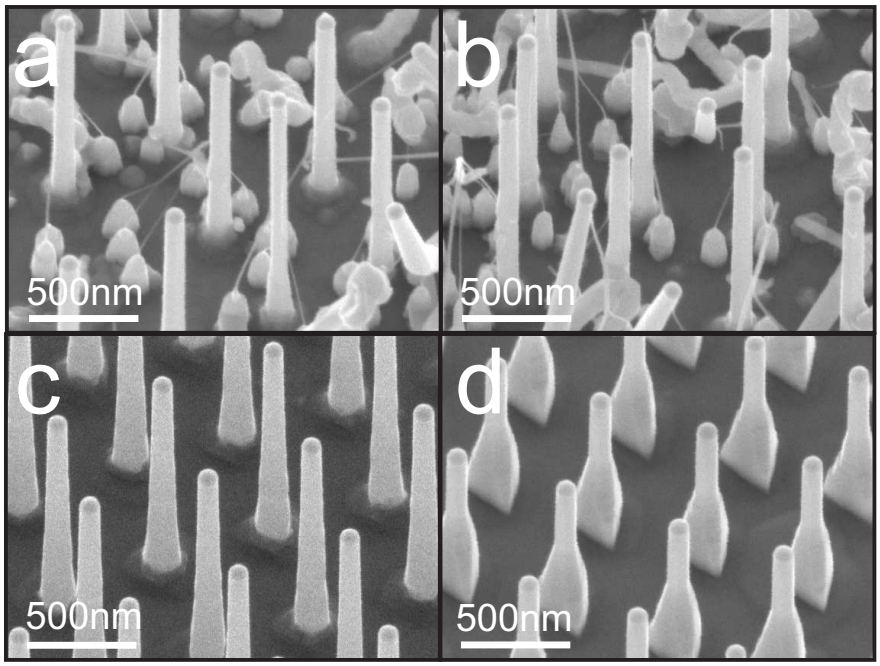

Figure 7.4: Influence of anneal step prior to growth InP nanowire arrays by surface conformal imprint lithography. Influence of annealing steps prior to growth. **(a)** No annealing **(b)** 420 °C anneal step **(c)** 550 °C anneal step **(d)** 700 °C anneal step. All samples are pre-treated with a piranha etch.

process effectively removes these residues and this cleaning process should also work successful for other lithographic techniques, such as e-beam, in which the same photo resist is used. This shows that we have found a generic method to clean the substrate surface after lithography and to avoid the growth of undesired nanowires.

Now that we managed to control the NWs position on a clean substrate, the growth parameters can be studied. In several papers that report on nanowire position control, it has been shown that the gold dots can break up into several droplets [9, 22], which resulted in several nanowires being produced from one intended gold island. Detailed studies of this phenomenon have been published for the growth of carbon nanotubes, where arrays are fabricated with the same techniques [23, 24]. We have investigated this effect by systematically varying the thickness of the gold layer from 1 nm to 6 nm. Clearly for 1 nm and 2 nm (see figure 7.5a and b) the gold dots split into several droplets (probably during the anneal), catalyzing the growth of several NWs close to each other. The gold splitting can be explained by the concept of surface tension. For a small thickness, the ratio surface/volume (or diameter/thickness) ratio is large, and the islands have

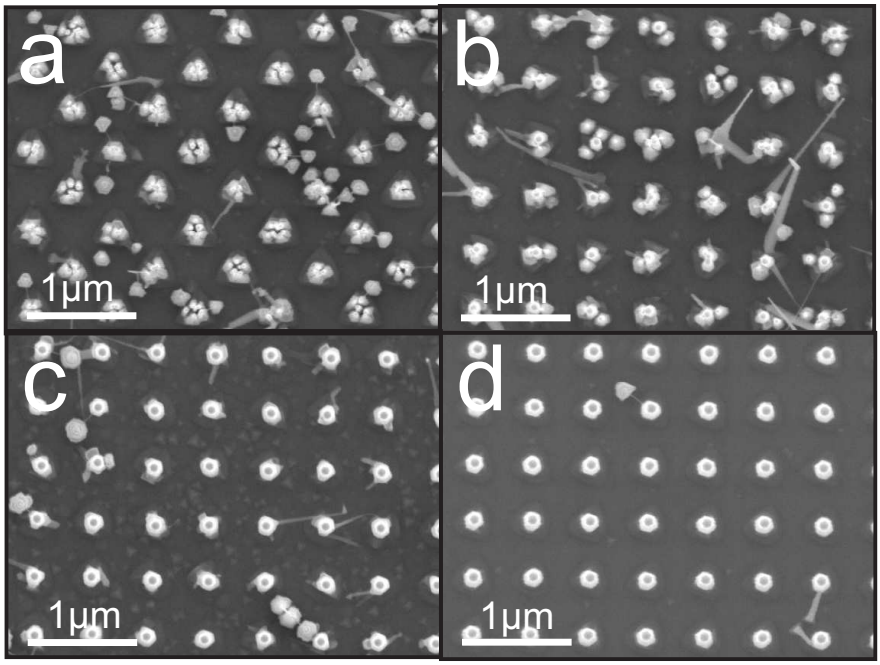

Figure 7.5: Influence of Au thickness Influence of Au thickness deposited on the imprinted arrays on the quality of nanowire growth. **(a)** 1nm Au **(b)** 2nm Au **(c)** 4nm Au **(d)** 6nm Au. All samples are pre-treated with an anneal step at 550 °C and a piranha etch.

a pancake-like shape. Due to the surface tension the gold dots split up to form spherical particles, which will decrease the liquid/air interface. At a thickness of 4 nm (figure 7.5c) still a few extra nanowires grow, however at 6 nm (figure 7.5d) no splitting of the gold droplet is observed. In order to test the quality of the nanowires grown in the arrays, we have synthesised InP/InAsP/InP heterostructured nanowires from the nanoimprinted Au islands. The optical properties of the InAsP section sensitively depend on the segment length and As/P ratio. We have applied different growth times and AsH_3 flows to fabricate segments with different lengths and compositions.

In figure 7.6a a representative tilted view SEM image is shown. The overall wire length is determined to be 5 microns. The base of the wire (up to 2 microns) is tapered, but the top part has a constant diameter. Such wire arrays are interesting for their photonic properties. We have used TEM HAADF and EDX measurements to determine the length and composition of the InAsP segments. The segment shown in figure 7.6b has a length of around 22 nm and has a $In_{50}As_{37}P_{13}$ composition. The quality of these nanowire segments has been studied optically by measuring the photoluminescence at 5K. The nanowires were transferred on

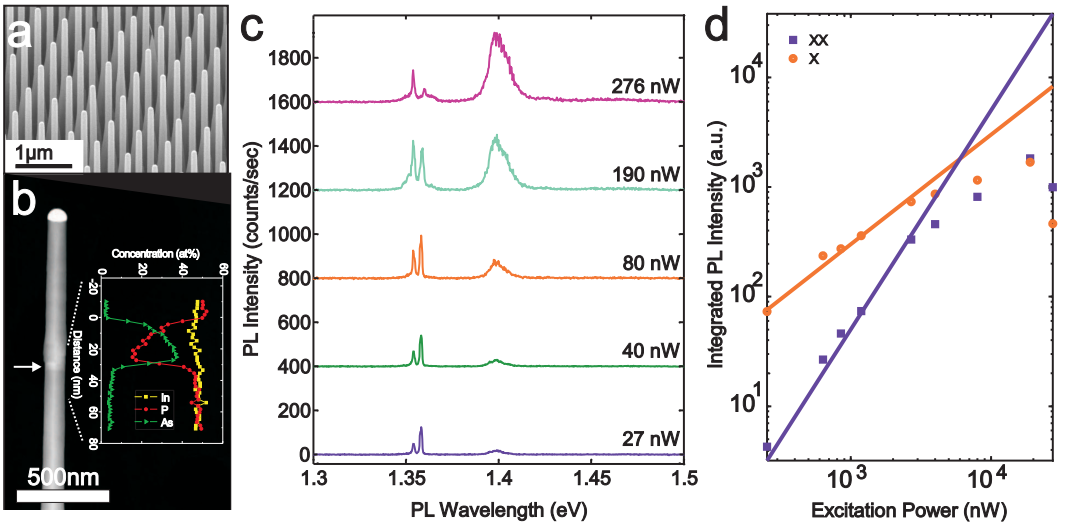

Figure 7.6: Heterostructures. Heterostructured InP-InAsP-InP nanowires. **(a)** SEM image viewing the array of heterostructured nanowires **(b)** HAADF TEM image showing the InAsP segment (bright) indicated by an arrow in the InP nanowires (dark). The inset shows the As concentration along the nanowire axis. The increased As concentration clearly shows the InAsP segment. Different As concentrations are observed before and after the InAsP segment. This is due to an As shell around the first InP part segment. **(c)** Photoluminescence data showing the quality of the dot emission grown in a patterned nanowire array.

a SiO_2 substrate to measure their optical properties, as the pitch between InP nanowires is too small to optically characterize standing single nanowire. Figure 7.6c presents the power dependence of a 10 nm long $In_{50}As_{37}P_{13}$ segment in the InP nanowire. In figure 4d is shown that the exciton (1.358 eV) emission at low excitation power (linear dependence) and a biexciton line (1.354 eV) evolves at higher powers (superlinear dependence). The line width (FWHM) is 2 meV for both peaks, which is higher than previous results obtained on InP/InAsP/InP nanowires [6]. In parallel with the biexciton line, a peak appears at 1.398 eV, corresponding to the PL emission of the InP nanowire segments. We show in the inset the exciton and biexciton intensities dependence with the power, and slopes of 1 and 2 are obtained for the exciton and biexciton. These results show that these dots grown using nanoimprint technique have a good optical quality and pave the way to large scale opto-nanoelectronic applications and photonic applications.

7.4 Conclusion

A generic process has been developed to grow arrays of (heterostructured) InP and GaP nanowires. Substrate conformal nanoimprint lithography has been successfully used to pattern gold particles on the substrate. We have shown that the preparation of the samples before growth with piranha solution in combination with a thermal anneal is a significant step to obtain perfect arrays. We are able to pattern complete 2 inch wafers with perfect nanowire arrays with excellent uniformity. This cleaning procedure is applicable to other lithography techniques as e-beam lithography, and therefore it is a generic process.

References

[1] X. Duan, Y. Huang, Y. Cui, J. Wang, and C. Lieber, "Indium phosphide nanowires as building blocks for nanoscale electronic and optoelectronic devices ," *Nature*, vol. 409, pp. 66–69, 2001.

[2] E. Minot, F. Kelkensberg, M. V. Kouwen, J. V. Dam, and L. Kouwenhoven, "Single Quantum dot nanowire LEDs ," *Nano Letters*, vol. 7, pp. 367–371, 2007.

[3] M. van Weert, A. Helman, W. van den Einden, R. Algra, M. Verheijen, M. Borgström, G. Immink, J. Kelly, L. Kouwenhoven, and E. Bakkers, "Zinc Incorporation via the Vapor-Liquid-Solid Mechanism into InP Nanowires," *Journal of the American Chemical Society*, vol. 131, pp. 4578–4579, 2009.

[4] S. Diedenhofen, G. Vecchi, R. Algra, A. Lagendijk, A. Hartsuiker, O. Muskens, G. Immink, E. Bakkers, W. Vos, and J. G. Rivas, "Broadband and omnidirectional antireflection coating based on semiconductor nanorods," *Advanced Materials*, vol. 21, pp. 973–978, 2009.

[5] R. Wagner and W. Ellis, "Vapor-Liquid-Solid mechanism of single crystal growth," *Applied Physics Letters*, vol. 4, pp. 89–90, 1964.

[6] M. van Weert, N. Akopian, U. Perinetti, M. van Kouwen, R. Algra, M. Verheijen, E. Bakkers, L. Kouwenhoven, and V. Zwiller, "Selective Excitation and Detection of Spin States in a Single Nanowire Quantum Dot," *Nano Letters*, vol. 4, pp. 1989–1993, 2009.

[7] M. Borgström, G. Immink, B. Ketelaars, R. Algra, and E. Bakkers, "Synergetic nanowire growth," *Nature Nanotechnology*, vol. 2, pp. 541–544, 2007.

[8] J. van Tilburg, R. Algra, G. Immink, M. Verheijen, E. Bakkers, and L. Kouwenhoven, "Surface passivated InAs/InP core/shell nanowires," *Sem. Sci. and Technology*, 2010.

[9] T. Mårtensson, M. Borgström, W. Seifert, B. Ohlsson, and L. Samuelson, "Fabrication of individually seeded nanowire arrays by vapour-liquid-solid growth," *Nanotechnology*, vol. 14, pp. 1255–1258, 2003.

[10] L. Jensen, M. Bjork, S. Jeppesen, A. Persson, B. Ohlsson, and L. Samuelson, "Role of Surface Diffusion in Chemical Beam Epitaxy of InAs Nanowires," *Nano Letters*, vol. 4, pp. 1961–1964, 2004.

[11] P. Mohan, J. Motohisa, and T. Fukui, "Controlled growth of highly uniform, axial/radial direction-defined, individually addressable InP nanowire arrays," *Nanotechnology*, vol. 16, pp. 2903–2907, 2005.

[12] H. Fan, W. Lee, R. Scholz, A. Dadgar, A. Krost, K. Nielsch, and M. Zacharias, "Arrays of vertically aligned and hexagonally arranged ZnO nanowires: a new template-directed approach," *Nanotechnology*, vol. 16, p. 913, 2005.

[13] H. Fan, B. Fuhrmann, R. Scholz, F. Syrowatka, A. Dadgar, A. Krost, and M. Zacharias, "Well-ordered ZnO nanowire arrays on GaN substrate fabricated via nanosphere lithography," *Journal of Crystal Growth*, vol. 287, pp. 34–38, 2006.

[14] T. Mårtensson, C. Patrik, T. Svensson, B. A. Wacaser, M. W. Larsson, W. Seifert, K. Deppert, A. Gustafsson, R. L. Wallenberg, and L. Samuelson, "Epitaxial III-V nanowires on silicon," *Nano Lett.*, vol. 4, pp. 1987–1990, 2004.

[15] T. Mårtensson, J. Wagner, E. Hilner, A. Mikkelsen, C. Thelander, J. Stangl, B. Ohlsson, A. Gustafsson, E. Lundgren, L. Samuelson, and W. Seifert, "Epitaxial growth of indium arsenide nanowires on silicon using nucleation templates formed by self-assembled organic coatings," *Advanced Materials*, vol. 19, pp. 1801–1806, 2007.

[16] M. Verschuuren and S. Wuister, "Imprint lithography," *US patent*, US 2008/0011934, 17/01/08.

[17] T. Odom, J. Love, D. Wolfe, K. Paul, and G. Whitesides, "Improved Pattern Transfer in Soft Lithography Using Composite Stamps," *Langmuir*, vol. 18, pp. 5314–5320, 2002.

[18] M. Verschuuren and H. van Sprang, "3D Photonic Structures by Sol-Gel Imprint Lithography," *Mater. Res. Soc. Symp. Proc*, vol. 1002, pp. 1002–N03–05.

[19] A. Clawson, "Guide to references on III-V semiconductor chemical etching," *Materials Science and Engineering: R: Reports*, vol. 31, pp. 1–438, 2001.

[20] A. Pierret, M. Hocevar, S. Diedenhofen, R. Algra, E. Vlieg, E. Timmering, M. Verschuuren, G. Immink, M. Verheijen, and E. Bakkers, "Generic nano-imprint process for fabrication of nanowire arrays," *Nanotechnology*, vol. 21, p. 065305, 2010.

[21] G. Stringfellow, *Growth mechanism of truncated triangular III-V nanowires*. Academic press, 1999.

[22] A. Roest, M. Verheijen, O. Wunnicke, S. Serafin, H. Wondergem, and et al., "Position-controlled epitaxial III-V nanowires on silicon," *Nanotechnology*, vol. 17, p. S271, 2006.

[23] A. Melechko, T. Mcknight, D. Hensley, M. Guillorn, A. Borisevich, and et al., "Large-scale synthesis of arrays of high-aspect-ratio rigid vertically aligned carbon nanofibres," *Nanotechnology*, vol. 14, p. 1029, 2003.

[24] V. Merkulov, D. Lowndes, Y. Wei, G. Eres, and E. Voelkl, "Patterned growth of individual and multiple vertically aligned carbon nanofibers," *APL*, vol. 76, pp. 3555–3557, 2000.

Summary

Nanotechnology refers to the understanding and controlling of materials on the nano (10^{-9} m) scale. Nanowires are a beautiful example of nanotechnology, with dimensions of ∼5-100 nm in diameter and up to several microns in length. They have a large aspect ratio of 1000 or more and therefore nanowires are referred to as 1-D structures. Due to the dimensions of the nanowires interesting optical and electrical properties are found that are not seen in bulk (3-D) materials. The crystal structure, defect density and morphology are important parameters that determine the quality of the nanowires. This thesis reports in detail on the formation and control of these parameters during the Vapor-Liquid-Solid (VLS) growth mechanism of nanowires with Metal Organic Vapor Phase Epitaxy (MOVPE).

In chapter 2 we have investigated the morphology of heterostructured GaP-GaAs nanowires grown by metal-organic vapor-phase epitaxy as a function of growth temperature and V/III precursor ratio. The study of heterostructured nanowires with transmission electron microscopy tomography allowed the three-dimensional morphology to be resolved, and discrimination between the effect of axial (core) and radial (shell) growth on the morphology. A temperature- and precursor-dependent structure diagram for the GaP nanowire core morphology and the evolution of the different types of side facets during GaAs and GaP shell growth were constituted.

In these wires many planar defects (twin planes) are present in the zinc-blende nanowire crystal structure, which are generally positioned in a random fashion along the nanowire length axis. However, under certain conditions twin pairs are formed, as described in chapter 3. In such pairs the first twin plane is formed at a random position, rapidly followed by the formation of a second twin plane of which the position is directly related to that of the first one. We show that the triangular $\{11\bar{2}\}$ morphology of the nanowire is a key element in the formation of these twin pairs. We have used our kinetic nucleation model, and show that this describes the development of the nanowire morphology and its relation with the formation of single and paired twin planes.

In chapter 4 we have investigated the formation of twinning superlattices in InP nanowires. We show that we control the crystal structure of Indium Phosphide (InP) nanowires by impurity dopants. We have found that zinc decreases the activation barrier for 2D nucleation growth of zinc-blende InP and therefore promotes the InP nanowires to crystallize in the zinc-blende, instead of the commonly found wurtzite crystal structure. More importantly, we demonstrate that we can, once we have enforced the zinc blende crystal structure, induce twinning superlattices with long-range order in InP nanowires. We can tune the spacing of the superlattices by the wire diameter and the zinc concentration, and we present a model based on the distortion of the catalyst droplet in response to the evolution of the cross-sectional shape of the nanowires to quantitatively explain the formation of the periodic twinning.

Twinning superlattices are predicted to give rise to a direct bandgap in normally indirect materials. Control in the segment length between two successive twin planes is crucial in order to manipulate the band structure. In chapter 5 we show for the first time that we are able to synthesize GaP twinning superlattice nanowires. Moreover by controlling the Ga pressure during growth we can alter the segment length independently from already known parameters like the nanowire diameter, Zn-concentration and temperature, which are found for InP and InAs. From the experimental data we are able to extract the effect of the chemical potential on the superlattice segment length and compare this with our quantitative model for InP superlattices. We find that the effect of surface energies rather than the chemical potential has a major effect on the superlattice segment length.

The crystal structure is an important parameter that determines the morphology of the wire. As shown for the paired and superlattice twins the droplet dynamics are affected by the morphology. In chapter 6 we report on an *in-situ* surface X-ray diffraction study of liquid AuIn metal alloys in contact with zinc-blende InP $(111)_B$ substrates at elevated temperatures. We observe strong layering of the liquid metal alloy in the first three atomic layers in contact with the substrate. In the first atomic layer the alloy has a higher indium concentration than in the bulk. In addition, in this first layer we find evidence for in-plane ordering at stacking fault positions. This can explain the typical formation of the wurtzite crystal structure in InP nanowires grown from AuIn metal particles.

Finally in chapter 7 a generic process has been developed to grow nearly defect free arrays of (heterostructured) InP and GaP nanowires. Soft nanoimprint lithography has been used to pattern gold particle arrays on full 2 inch substrates. After lift-off organic residues remain on the surface, which induce the growth of additional undesired nanowires. We show that cleaning of the samples before

growth with a piranha solution in combination with a thermal anneal at 550 °C for InP and 700 °C for GaP results in uniform nanowire arrays with 1% variation in nanowire length, and without undesired extra nanowires. Our chemical cleaning procedure is applicable to other lithographic techniques such as e-beam lithography, and therefore represents a generic process. The patterned structures that can be made in this way are extremely useful for future experiments. The control in positioning eliminates fluctuations in nanowire diameter and density on the substrate. This ensures an equal mass transport and diffusion between the nanowires and thus an increased control in the nanowire growth compared to growth from colloids or thin film.

Rienk Algra

Samenvatting

Nanotechnologie verwijst naar het begrip en de beheersing van materialen op de nano schaal (een miljardste meter). Met een diameter van ongeveer 5 tot 100 nm en een lengte van enkele micrometers zijn nanodraden een prachtig voorbeeld van nanotechnologie. Ze hebben een grote aspect ratio van 1000 of meer en daarom worden nanodraden aangeduid als 1-dimensionale structuren. De afmetingen van de nanodraden bieden interessante optische en elektrische eigenschappen die niet voorkomen in bulk (3-D) materialen. Belangrijke parameters die de kwaliteit van de nanodraden bepalen zijn de kristalstructuur, defect dichtheid en de morfologie. Dit proefschrift beschrijft in detail de vorming van verschillende kristalstructuren met de hierbij behorende morfologie en hoe defecten optreden tijdens het groeiproces. Aan de hand van verschillende parameters wordt het dampvloeistof-vaste stof (in het engels beter bekend als het VLS (Vapor-Liquid-Solid))-groeimechanisme van nanodraden in een Metal Organic Vapor Phase Epitaxie (MOVPE) reactor beschreven.

In hoofdstuk 2 hebben we onderzoek gedaan naar de morfologie van GaP-GaAs heterostructuur nanodraden als functie van de temperatuur en de groei V/III precursor ratio. Met behulp van een transmissie elektronen microscoop, in tomografie mode, is het mogelijk om een reconstructie van de 3-D structuur van de nanodraden te maken. Dit stelt ons in staat onderscheid te maken tussen het effect van axiale (lengte) en radiale (dikte) groei van de morfologie. Voor de groei van de GaP nanodraad segmenten is een structuur diagram gemaakt als functie van de groei temperatuur en precusor-afhankelijkheid. Tevens wordt de evolutie van de verschillende zijfacetten besproken.

In deze draden komen in de zinc-blende kristalstructuur veel vlak-defecten (tweeling grenzen, ookwel 'twins' genoemd) voor, die over het algemeen op een willekeurige wijze langs de lengte-as van de nanodraad zijn verspreid. Echter, onder bepaalde condities worden tweelingparen gevormd, zoals beschreven in hoofdstuk 3. In zulke paren wordt het eerste defect gevormd op een willekeurige positie, snel gevolgd door de vorming van een tweede defect waarvan de positie direct gerelateerd is aan de eerste. We tonen aan dat de driehoekige $\{11\bar{2}\}$ morfologie van de

nanodraad een belangrijk element is in de vorming van deze tweelingparen. We hebben gebruik gemaakt van ons kinetisch nucleatie model om de vorming van enkele en dubbele tweeling grenzen te beschrijven en tonen aan dat er een sterke relatie is met de ontwikkeling van de nanodraad morfologie.
In hoofdstuk 4 hebben we onderzoek gedaan naar de vorming van superroosters in InP nanodraden. De kristalstructuur van Indiumfosfide (InP) nanodraden kan worden beïnvloed door het gebruikt van onzuiverheden als dotering. Het gebruikt van zink verlaagd de activeringsenergie die nodig is voor 2D-nucleatie van de zinc-blende InP nanodraden. Het stimuleert de groei van InP nanodraden in de zinc-blende kristal structuur, in plaats van de gewoonlijke wurtzite kristalstructuur. Als we eenmaal de zinc-blende kristalstructuur hebben afgedwongen, induceren we onder deze omstandigheden een superrooster van defecten over de volledige lengte van de InP nanodraden. De afstand tussen de defecten van de superroosters kunnen we afstemmen door middel van de draad diameter en de zink-concentratie. We presenteren een model dat gebaseerd is op de vervorming van de katalysator druppel in reactie op de evolutie van de dwarsdoorsnede vorm van de nanodraden om kwantitatief de vorming van de periodieke defecten (twinning superroosters) uit te leggen.
Berekeningen in de literatuur laten zien dat twinning superroosters kunnen leiden tot een directe bandgap in normaal indirecte materialen. Het is hiervoor van cruciaal belang om de segment lengte tussen twee opeenvolgende defecten (twins) te kunnen manipuleren. In hoofdstuk 5 laten we voor de eerste keer zien dat we in staat zijn om GaP twinning superrooster nanodraden te synthetiseren. Bovendien kunnen we de segmentlengte aanpassen door de Ga druk tijdens de groei aan te passen. Dit blijkt mogelijk te zijn naast de al bekende parameters zoals de nanodraad diameter, zink concentratie en de temperatuur, die zijn gevonden voor InP en InAs. Uit de experimentele gegevens zijn wij in staat om het effect van de chemische potentiaal te bepalen en deze te vergelijken met ons kwantitatieve model voor InP superroosters. Het effect van de oppervlakte energie, in plaats van de chemische potentiaal, blijkt een groot effect op de superrooster segmentlengte te hebben.
De kristalstructuur is een belangrijke parameter die de morfologie van de draad bepaalt. Zoals we hebben laten zien voor de gepaarde en superrooster twins beïnvloed de druppel dynamiek de morfologie van de nanodraad. In hoofdstuk 6 brengen we verslag uit van een *in-situ* oppervlakte röntgen diffractie studie bij verhoogde temperaturen van vloeibare AuIn metaallegeringen in contact met zink-blende InP $(111)_B$ substraten. We vinden een sterke gelaagdheid in de eerste drie atomaire lagen van de vloeibare metaal legering in contact met het substraat. De eerste atomaire laag van de legering vertoont een verhoogde concentratie

indium vergeleken met de bulk. Bovendien vinden we aanwijzingen voor in-plane ordening van deze atomen in deze eerste laag op stapelfout posities. Dit kan de typische vorming van de wurtzite kristalstructuur in InP nanodraden gegroeid vanuit AuIn metaal deeltjes verklaren.
Tenslotte wordt in hoofdstuk 7 een generiek proces beschreven dat is ontwikkeld om bijna foutloos gestructureerde velden te groeien van InP en GaP (heterostructuur) nanodraden. Het proces dat hiervoor gebruikt is heet soft nano-imprint lithografie en biedt de mogelijkheid om een patroon van Au deeltjes op een hele 2 inch wafer te zetten. Na het lift-off proces blijven vaak organische reststoffen achter op het oppervlak. Deze kunnen de groei van extra ongewenste nanodraden induceren. We laten zien dat het schoonmaken van de samples vóór de groei met een chemische etch (piranha-oplossing) in combinatie met een thermisch anneal bij 550 °C voor InP en 700 °C voor GaP resulteerd in uniforme gestructureerde velden van nanodraden met sechts 1 % variatie in de nanodraad lengte en zonder ongewenste extra nanodraden. Onze chemische reinigingsprocedure kan tevens gebruikt worden voor andere lithografische technieken zoals e-beam lithografie, en is daarom een generiek proces. De gestructureerde patronen die op deze manier gemaakt kunnen worden zijn uitermate geschikt voor toekomstige experimenten. De controle in de positie elimineert schommelingen in de nanodraad diameter en dichtheid van de draden op het substraat. Dit komt door een gelijk massa transport en gelijke diffusie van materiaal tussen de nanodraden. Hiermee wordt het inzicht in de groei vergroot en is er meer controle over het groeiproces vergeleken met de groei van nanodraden uit colloïden of dunne film.

Rienk Algra

Dankwoord

Nu dit proefschrift klaar is heb ik gemerkt dat de eerste alinea van een hoofdstuk of artikel altijd het moeilijkste is om te schrijven. Natuurlijk heb je voordat je begint met schrijven al een idee wat er ongeveer allemaal in moet komen te staan, maar het schrijven van een pakkende, inspirerende, originele en/of sappige introductie is lang niet altijd even voor de hand liggend. Vanzelfsprekend is dit hoofdstuk daar geen uitzondering op. Meerdere versies van deze allereerste alinea hebben hier gestaan, maar waren de moeite uiteindelijk toch niet waard. Kortom, schrijven is schrappen en zo schrijven wij onze hoofdstukken... [1]. Gelukkig heb ik op deze manier dit terugkerende probleem omzeild en kan ik mij nu richten op het doel van dit hoofdstuk.

Mijn promotieonderzoek was een samenwerking tussen het Materials innovation institute in Delft, de Radboud Universiteit Nijmegen en Philips Research in Eindhoven. Dit hield in dat ik vaak op verschillende locaties aan het werk was en op deze manier met veel mensen in contact ben gekomen. Hoewel het reizen af en toe niet mee viel, zeker niet in de vroege uurtjes om de files te vermijden, ben ik ervan overtuigd dat de nauwe samenwerking uiteindelijk heeft geleid tot de resultaten die beschreven staan in de voorgaande hoofdstukken.

Het doel van dit hoofdstuk is om iedereen te bedanken. Toch wil ik voorkomen dat het woord 'bedankt' in iedere regel terug komt en geef ik liever een impressie van mijn vier jaar onderzoek en iedereen die ik daarbij ben tegengekomen. Vandaar dat ik op deze plek iedereen wil bedanken voor de inzet, kennis, kunde, inspiratie en het enthousiasme waarmee jullie hebben bijgedragen aan het tot stand komen van dit proefschrift.

Voor het begin van mijn promotie had ik nauwelijks kennis van halfgeleiders en van nanodraden had ik zelfs nog nooit gehoord. Het was voornamelijk het onderzoek in kristalgroei, die ik tijdens mijn studie al had mogen ervaren, die mij ertoe geïnspireerd heeft om hierin verder te gaan. Die mogelijkheid kreeg ik toen Elias en Erik mij het nanodraden project toevertrouwden.

[1] Vrij vertaald naar Herman Finkers, uit het Elfstedentochtlied: 'Schrijven is schrappen en zo schrijven wij dus onze liedjes' en Godfried Bomans, 'Schrijven is Schrappen', 1989

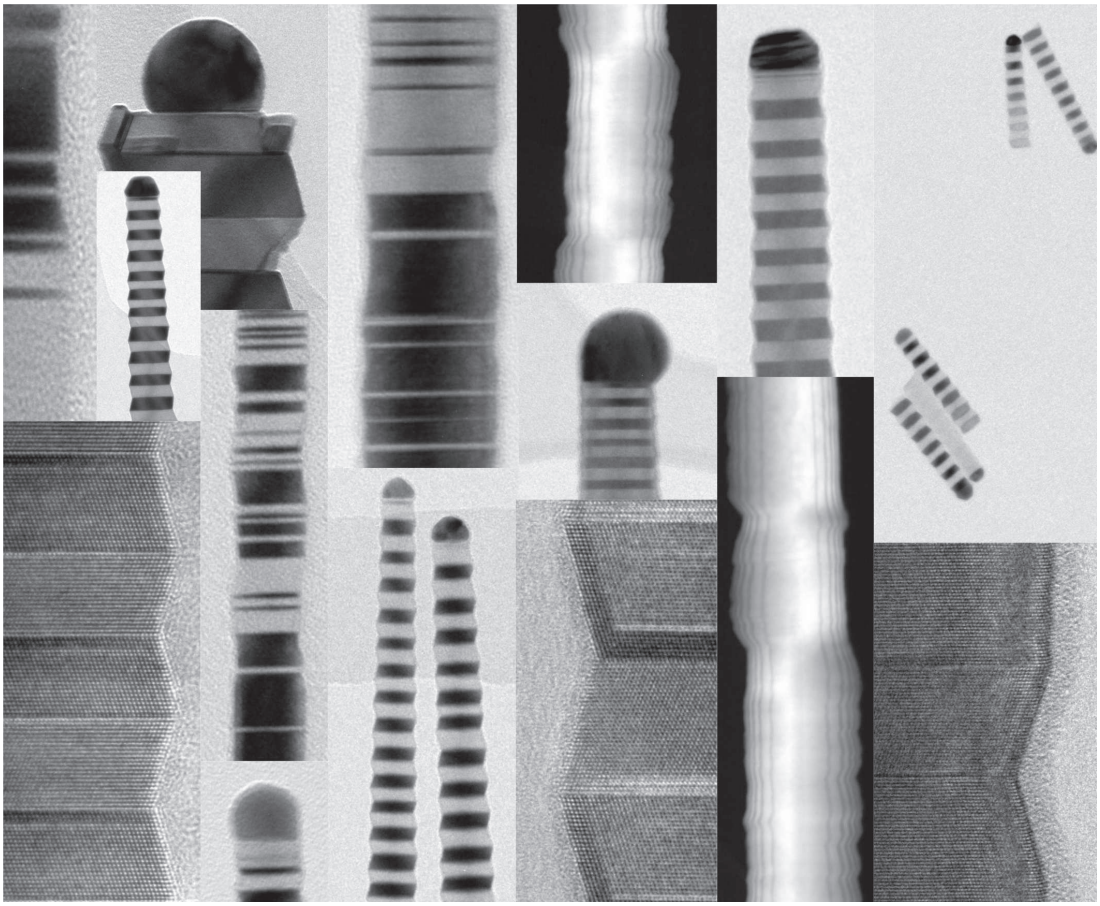

TEM collectie Impressie van nanodraden TEM foto's van vier jaar promotie.

Elias, je enthousiasme en toewijding in de kristalgroei zijn een grote inspiratie geweest voor mijn onderzoek. Zo heb je mij de wereld van oppervlakte diffractie laten zien en hebben we meerdere malen dag en nacht shifts tijdens ESRF runs uitgevoerd. Ook op niet-wetenschappelijk gebied heb ik leuke herinneringen zoals ons uitstapje naar de Bonneville Speedway op de zoutvlaktes in de buurt van Salt-Lake city, 'daar moesten we gewoon naar toe met de mannen...'. Uren rijden over kaarsrechte wegen door de zoutvlaktes in een Amerikaanse bak (wel jammer dat het geen Chevrolet caprice was, zo eentje met van die houten panelen) waren meer dan de moeite waard! De grijns staat nog steeds op onze gezichten naast al die futuristische racewagens.
Erik, ook jouw enthousiasme was onuitputtelijk. Je was al een tijd bezig met nanodraden voordat ik in je groep terecht kwam. Hierdoor kon ik een vliegende start maken en meteen profiteren van alle kennis die er al was over nanodraden. Altijd kon ik bij je terecht voor vragen of discussies en je kwam dan vaak met

goede ideeën en suggesties. Meestal begon het met 'even een vraagje', maar eigenlijk was het nooit 'even overleggen' en resulteerde dit in een uurtje discussie. Zeker de discussies naar welk journal het komende artikel dit keer moest worden gestuurd kwamen herhaaldelijk terug. Maar vaak eindigden de discussie ook in het praten over van alles en nog wat. Daarnaast heb je mij echt leren schrijven, wat zoals gezegd, niet eenvoudig is. Je hebt mij leren schrappen en de bevindingen kort maar krachtig, en vooral niet herhaaldelijk, op te schrijven. Helaas heb ik nog steeds niet (hoe is het mogelijk in vier jaar tijd) mogen meemaken hoe het is om met je te 'wadlopen'. Dit ging helaas niet door vanwege onweer in het geplande weekend. Ik houd me aanbevolen om dat alsnog eens te gaan doen!

Naast Erik heb ik dankzij de ruime ervaring met nanodraden van Magnus snel een goede basiskennis kunnen opbouwen over nanodraden. Veel aspecten die belangrijk zijn tijdens de groei van nanodraden en de 'pre-treatment' van de samples heb je mij geleerd. In de discussies over groei moest ik altijd met goede argumenten komen om je te overtuigen of het wel echt zo was. Net zo ging het als ik weer eens beweerde dat het weer in Nederland zo slecht nog niet is. Ook al vond je dat toentertijd niet, deel je die mening nu gelukkig wel nu je weer terug in Zweden bent. Tijdens de nanowire workshop in Lund mochten we bij jou logeren en heb je mij de Wii geïntroduceerd en vreemde maar wel lekkere soepen laten proeven zoals de blåbärsoppa en Nyponsoppa. Självklart försöker jag också att skriva något på Svenska. Därav med hjälp av en översättare på Internet hatt försök. Tack för all hjälp i tillväxten av nanotrådar och alla goda diskussioner.

Omdat de nanodraadjes zo klein zijn, de naam zegt het al, heb je speciale technieken nodig om de draden te bekijken. Hierin is Marcel echt een de expert. Met het grootste gemak weet je de nanodraden die gegroeid zijn haarscherp af te beelden met de TEM. Zelfs nieuwe technieken die het mogelijk maken om driedimensionaal de draden te bekijken schrikken je niet af. Je hebt echt ontzettend veel (bijna 7.000) plaatjes voor mij 'geschoten' en doordat je zo betrokken bent geweest met het nanodraden project, en je kristalgroei kennis, hebben we het maximale uit de TEM-plaatjes kunnen halen en nieuwe modellen kunnen maken die de groei van de draadjes beschrijft. Vaak kwam ik met lastige vragen bij je langs of het plaatje toch net niet iets anders kon, maar altijd stond je paraat en maakte je tijd in je overvolle agenda om nieuwe samples te bekijken of te discussiëren. Naast alle plaatjes hebben we veel gelachen en gepraat over onderwerpen variërend van vakantie en films tot tuinkabouters! Daarnaast waren we ook erg goed in korte email conversaties, waar je na tien mails denkt: 'ik had toch beter even kunnen bellen, dat was sneller geweest ...'.

Met alle vragen over kristalgroei kon ik altijd terecht bij Willem. Echt een lopende encyclopedie waar ontzettend veel kennis en gevoel voor groeiprocessen in zit.

Door de discussies met Willem kom je steeds weer op nieuwe ideeën of los je een probleem op door het bij de oorsprong aan te pakken. Zelf als het even iets minder met je gezondheid ging kon ik bij je thuis langs komen voor nieuwe input. Willem je bent echt een 'Grand Cru' op het gebied van kristallografie!
Ongeveer halverwege mijn promotie waren we druk bezig met het vinden van een model voor de vorming van 'twinning superlattices' in de nanodraden, waar de defecten op een regelmatige manier geordend zijn in de draad. Hier kwam de hulp van Lou-Fé als geroepen. Door heel precies en gestructureerd te kijken naar alle aspecten die een rol spelen tijdens de groei van de draadjes en ook de rol van het goud-druppeltje eens precies onder de loep te nemen, kwamen we uiteindelijk tot een prachtig model dat onze experimenten uitstekend beschrijft. Ik bewonder hoe kritisch je naar vraagstukken kunt kijken en hoe precies je kan werken. Ook de prachtige verhalen over Schotland en Italië zal ik niet snel vergeten.
Zonder George waren er nooit zulke mooie nanodraden gemaakt. De jarenlange ervaring met de B-reactor, en toch ook wel je liefde voor de nanodraadjes, zorgde ervoor dat bijna ieder runnetje een succes was. Vaak kwam ik 's ochtends vroeg na een uurtje sampletjes schoonmaken naar WZ (voor de niet Philips mensen: het gebouw waar George zit). Eerst 'een bakkie' doen uiteraard, soms wel twee, om vervolgens de komende runnetjes te bespreken. Hier en daar veranderden we dan terplekke nog een beetje het groeirecept en vaak dezelfde dag nog 'zag het sampletje er goed uit', ook al waren ze af en toe wel erg klein van formaat. Talloze onderwerpen hebben we besproken aan de koffietafel, te veel om op te noemen. En hoewel je mij af en toe plagend 'de klant' noemde heb ik dat nooit zo ervaren, maar zie ik je eerder als een echte collega waar we als team niet zonder kunnen!
Met Maarten (v. Weert) heb ik de optische kant van nanodraden bekeken. Talloze batches met QDs (Quantum Dots) in nano-draadjes hebben we op deze manier gemaakt. Daarnaast hebben we mijn TSL (Twin SuperLattice) nanodraden meerdere malen met de PL-opstelling in Delft bekeken. Veel sleutelen met spiegeltjes en filtertjes (die af en toe best moeilijk te vinden zijn...) om tot de conclusie te komen dat we niks zien. Ook de Matlab-skills van Maarten kwamen zeer van pas bij het zoeken naar periodieke structuren. En hoewel we de tijd niet hadden om alles af te maken ben ik ook van mening dat er misschien wel een super-super structuur in zat!
Samen met Silke heb ik gewerkt aan 'piramidevormige' nanodraden om hiermee een antireflectie-coating te maken. Na een aantal pogingen is dit ook daadwerkelijk gelukt. Naast het echte werk heeft Silke ons ook kennis laten maken met een gezellige Duitse traditie die 'feuerzangenbowle' heet!
Moïra, you arrived in the group at Philips roughly halfway my project and started on a difficult growth subject with Si. I am convinced that you will succeed in

making the hetero-structures. Together with you and Aurélie we achieved to developed a new cleaning method for nano-imprint and will continue used the stamps in further research, which will improve our control over nanowire growth. Although you also taught me some (interesting) French words I feel I should not mention them here...
Naast Aurélie hebben ook twee andere studenten zich gewaagd aan de nanodraden. Jordy heeft gewerkt aan de groei van draden vanuit goud-colloïden. Groeien deden de draden wel, maar toch was het erg lastig om de colloïden goed in contact te brengen met het substraat. Daarnaast kon je altijd een gezellig praatje bij jou maken en hebben we menig tripje in de auto naar Nijmegen gemaakt. Tristan heeft naar defecten in nanodraden gekeken en is hier uiteindelijk toch in geslaagd om een computermodel voor te schrijven.
Together with Jaime and Silke we had a nice collaboration with the group of Reiner after a chat in San Francisco. The sSNOM measurements of Johannes and Andy made it possible to analyze the doping profiles in the nanowires, resulting in a nice paper. Samen met Otto hebben we oude samples doorgespit en op basis hiervan nieuwe experimenten gedaan die tot mooie publicaties hebben geleid.
De meest exotische materialen (zoals Scandium) werden gebruikt door Tim, wat ook nanodraad groei tot gevolg had. Het bleek niet eenvoudig om vervolgens te achterhalen hoe deze nu precies tot stand zijn gekomen.
Naast het groei- en TEM-werk heb ik ook veelvuldig gebruik gemaakt van andere technieken. Hetty, Frans en Monique stonden altijd klaar om te SEMmen en de (vele) samples die ik langs kwam brengen werden altijd met enthousiasme ontvangen. De 'misbaksels' werden ook bekeken en deden vaak ergens aan denken zoals een lantaarn paal, bloemkool, eiffeltoren, taipei 101, etc. Bij Eddy en Emile (v. Thiel) kon ik terecht voor het opdampen van dunne metaal laagje op de samples. We hebben een aantal mooie legeringen op deze manier gemaakt die we vervolgens met oppervlaktediffractie hebben kunnen bekijken. Met Emile (Verstegen) heb ik heel wat moeite en tijd in Raman-metingen gestoken om te kijken of onze gemaakte structuren in de nanodraad een nieuwe eigenschap had. Helaas hebben we die (tot nu toe) nog niet kunnen vinden. Wel was het mooi om te zien dat een deel van de Raman opstelling was uitgebreid met lego-blokjes! Harry kon altijd helpen met diffractie en regeltjes die het makkelijk maken om te bepalen of bepaalde kristalvlakjes equivalent zijn of niet. And although we never met, Ralf helped us solving a polarity problem by using CBED and Erwan introduced use to TEM tomography. Thank you for the collaboration! Bij alle Philips mensen die ik hier al genoemd heb horen ook alle collega's uit de groep van Derk (Reefman) die hebben gezorgd voor een gezellige promotie tijd.

De afdeling Vaste Stof Chemie voelde voor mij als een tweede thuis. Iedereen was altijd even vrolijk en we hebben veel gelachen tijdens de koffiepauzes, afdelingsuitjes, congressen, wijnproefmiddagen en de Risk- en...of diner-avondjes. Om een idee te geven wat je zoal kunt verwachten op de afdeling:

Allereerst is het altijd fijn om de dag te beginnen met een goeie bak koffie. Als je 's ochtends op de afdeling aankwam was het altijd fijn om het eerste kopje koffie van die dag te ruiken die klaar stond bij Jan. Een sterke maag is wel vereist want het was altijd lekkere 'straffe' koffie. Alle onderwerpen die je kunt bedenken zijn de revue wel gepasseerd in vier jaar promotietijd. Ook met alle bestellingen en

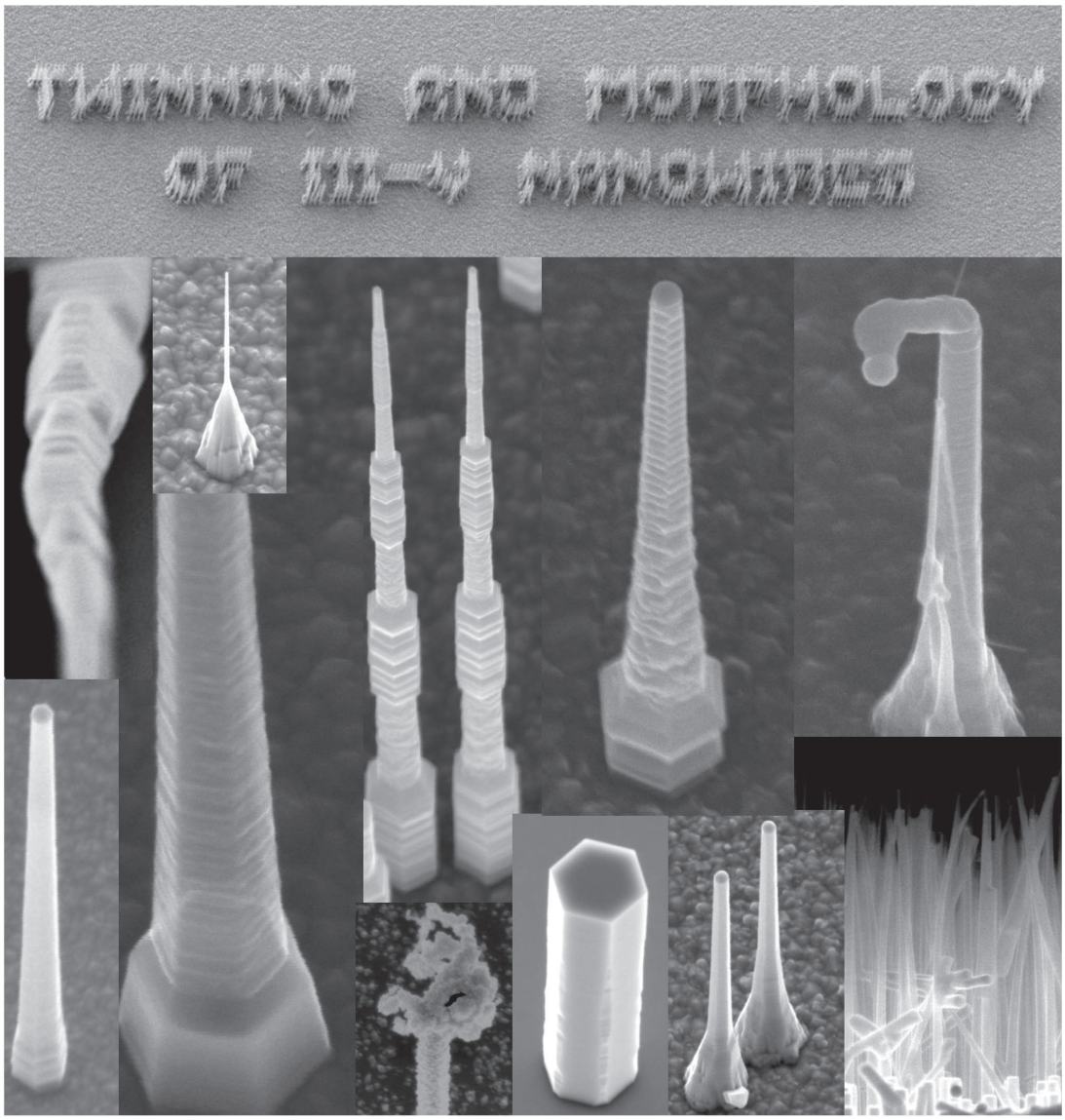

SEM collectie Impressie van nanodraden SEM foto's van vier jaar promotie.

betalingen stond Jan altijd voor je klaar.
Met Wim moet je vooral oppassen geen lichamelijk letsel op te lopen, hetzij in Park City dan wel de Ooipolder. Gelukkig blijft het dan bij een paar hechtingen en levert dit naderhand weer een hilarisch verhaal op! Ik hoop wel dat je in Harvard deze traditie niet voortzet, want nu ben ik niet meer in de buurt om je op te vangen. Om in de 'sportieve' hoek te blijven moet ik ook zeker het tavelvoetbal hier vermelden. De 'klinker' is zeker een bal die Wim veelvuldig wist te scoren, net als Angewandtes trouwens.
Paul (Tinnemans) is altijd in voor een praatje of verzetje en kan je altijd helpen met vragen over oppervlakte diffractie. Ook de haute cuisine kun je bij Paul vinden en graag laat hij foto's zien van de nieuwste creatie zoals plaatjes een overheerlijke vis(senkoppen)soep.
De analyse van onze ERSF data heb ik voornamelijk samen met Vedran gedaan en heel wat modelletjes hebben we geprobeerd om de structuur op het oppervlak te analyseren. De bonenschotel (cassoulet) was echt enorm (en volgens mij nog steeds niet helemaal op...).
Samen met Ismail heb ik heel wat (nachtelijke) uurtjes tijdens de ESRF runs doorgebracht. En tja, dan moet ik toch altijd weer denken aan het eindeloos lekdicht maken van de sampletjes op de houdertjes met twee-komponenten lijm: oui, oui, normalement ce n'est pas de problème, mais...
Tijdens een aantal ESRF runs waren ook Fieke (gek op de chocoladetaartjes van de kantine), Arno (weet alles over bevolkingsaantallen (altijd handig) en vond de koeientong inclusief haren van de kantine iets minder lekker...), Natalia (ik heb bewondering hoe snel je Nederlands hebt geleerd), Erik (Tanchini) en Aryan erbij. Didier was always standing by to help during our runs at the ESRF beamline ID03. Cheers! Ter voorbereiding aan zo'n run is het belangrijk om de opstelling tiptop in orde te hebben. Hiervoor komt de handigheid en grondige voorbereiding van Wiesiek zeer van pas wat z'n vruchten afwerpt tijdens een run.
Ookal zijn alle computers op de afdeling van Windows voorzien (op die ene van Hugo na natuurlijk) moet ik 'in verband met allerlei redenen' toegeven, dat LaTeX toch een fantastisch programma is om een proefschift mee te schrijven. Hoewel dit af en toe wat frustraties geeft met bepaalde packages weet Hugo toch altijd diep in de roots van LaTeX het probleem op te lossen.
Verder heeft Alaa ons in het Arabisch onze namen leren schrijven en Zjak was net als ik ook vaak aan het pendelen tussen de uni en industrie. Met Rene heb ik een mooie discussie over defecten en twin planes gehad (zijn het nu dislocaties of juist roosterfouten), en Jan (Smits) is altijd bereid om je kristallen met diffractie te analyseren. Alle studenten op de afdeling (te veel om allemaal op te noemen) zorgen altijd voor de nodige gezelligheid. Tot slot kan de afdeling niet zonder

een Elisabeth die altijd enthousiast maar ook altijd een beetje gehaast door de gangen loopt (wat het wel gemakkelijk maakte om te herkennen wie er aan komt).

Met de groep van Val en Leo in Delft hadden we een goed contact. We hebben veel samengewerkt door nanodraadjes te groeien die vervolgens op hun optische eigenschappen werden beoordeeld. Maarten (v. Kouwen) kon altijd erg enthousiast vertellen over de nieuwste resultaten, Nika you always had interesting special requests on various types of nanowires en met Juriaan keken we soms naar wel erg dunne shells.
Tegen het eind van mijn promotie is Erik zijn eigen nanodraden groep begonnen op de TU/e en TUdelft. Hier werden we vriendelijk ontvangen door Margriet en Paul (Koenraad). Tillman started his PhD on nanowire growth here, and can continue the nice work on nanowire growth.
Vanuit M2i heb ik tijdens mijn promotie vooral te maken gehad met de programmanagers Menno en Derk (Bol). Eigenlijk zagen we elkaar alleen tijdens de meetings samen met de Philips- en RU-groep en de cluster meetings. Dankzij de inzet van Derk hebben we een mooi artikel in het Financieel Dagblad gekregen. Daarnaast heb ik tegen het einde van mijn promotietijd veel contact met Monika gehad en heeft zij mij erg geholpen bij het zoeken naar een nieuwe baan.

Met Harm heb ik ongeveer wekelijks van alles en nog wat besproken over mijn proefschift tijdens onze wekelijkse tennis-avondjes. Dit varieerde van inhoudelijk tot layout en verder. Ook de vele uurtjes bordspellen waren erg vermakelijk en een goede afleiding tijdens soms erg drukke weken.

Mijn familie en schoonfamilie hebben mij altijd gesteund in de aflopen vier jaar. Soms was het moeilijk om precies te verwoorden wat je nu doet, maar altijd waren jullie bereid te helpen en mee te denken over allerlei onderwerpen. Daarnaast waren ook het advies voor de cover en tips voor de introductie erg handig.

Tot slot richt ik graag nog een woord aan mijn lieve vrouw Marianne. Alweer meer dan twee jaar geleden zijn wij getrouwd en al jaren langer kunnen we niet zonder elkaar. Zonder jouw steun op de moeilijkere momenten of de late avondjes was het nooit gelukt om dit alles voor elkaar te krijgen. Samen gaan we nu een nieuwe levensfase tegemoet waarin we het mooiste geschenk van nieuw leven verwachten!

Rienk

Curriculum Vitae

Rienk Ewoud Algra

05-03-1981	Geboren te Amsterdam
1993-1999	VWO; Trichter College, Maastricht
1999-2001	Chemical Technology, Eindhoven University of Technology
2001-2006	Master Chemistry, Radboud University Nijmegen
2005	Internship at Solid State Chemistry Department, Radboud University Nijmegen *'Epitaxial growth of organic crystals on organic substrates from the gas phase.' and 'An extreme case of solvent induced morphology change'(see publications)*
2006	Internship at Fuji Photo Film B.V., Tilburg *'Crystallization control of 4 liter scale precipitation of organic compounds focusing on polymorphism and size distribution, using Fuji's technology for precipitation.'*
2006-2010	PhD Student for Radboud University Nijmegen/ Philips Research Eindhoven and M2i Materials innovation institute (former NIMR; Nederlands Institute of Metal Research) under supervision of Prof. Dr. E. Vlieg and Prof. Dr. E.P.A.M. Bakkers *'Project on VLS growth of semiconducting nanowires.'*
2010-Now	Researcher at AkzoNobel Industrial Chemicals, Deventer *'Salt research group'*

List of publications

[1] R. Algra, W. Graswinckel, W. v. Enckevort, and E. Vlieg, "Alizarin crystals: An extreme case of solvent induced morphology change," *J. Cryst. Growth*, vol. 285, pp. 168–177, 2005.

[2] R. Algra, M. Verheijen, M. Borgström, L. Feiner, G. Immink, W. van Enckevort, E.Vlieg, and E. Bakkers, "Twinning superlattices in indium phosphide nanowires," *Nature*, vol. 456, pp. 369–372, 2008.

[3] R. Algra, M. Verheijen, L.-F. Feiner, G. Immink, R. Theissmann, W. van Enckevort, E. Vlieg, and E. Bakkers, "Paired Twins in GaP Nanowires," *Nano lett.*, vol. 10, pp. 2349–2356, 2010.

[4] R. Algra, V. Vonk, D. Wermeille, W. Noorduin, F. Bruele, A. Bode, E. Tancini, A. D. Jong, W. Szweryn, M. Verheijen, E. Bakkers, W. v. Enckevort, and E. Vlieg, "Pre-ordering at the liquid-solid AuIn-InP interface during nanowire growth," *submitted to Nano Lett.*, 2010.

[5] R. Algra, M. Verheijen, G. Immink, E.Vlieg, W. v. Enckevort, and E. Bakkers, "Effect of Chemical potential on GaP twinning superlattice nanowires," *submitted*, 2010.

[6] R. Algra, M. Verheijen, M. Hocevar, G. Immink, E. Vlieg, and E. Bakkers, "Template growth of Si twin superlattice nanowire tubes," *In preparation*, 2010.

[7] N. Radenovic, D. Kaminski, W. v. Enckevort, S. Graswinckel, I. Shah, M. in 't Veld, R. Algra, and E. Vlieg, "Stability of polar 111 NaCl crystal faces ," *J. Chem. Phys.*, vol. 124, p. 164706, 2006.

[8] M. Borgström, G. Immink, B. Ketelaars, R. Algra, and E. Bakkers, "Synergetic nanowire growth," *Nature Nanotechnology*, vol. 2, p. 541, 2007.

[9] M. Verheijen, R. Algra, M. Borgström, G. Immink, E. Sourty, W. van Enckevort, E. Vlieg, and E. Bakkers, "Three dimensional morphology of GaP-GaAs nanowires revealed by transmission electron microscopy tomography.," *Nano Lett.*, vol. 7, pp. 3051–3055, 2007.

[10] O. Muskens, J. Gomes-Rivas, R. Algra, E. Bakkers, and A. Lagendijk, "Design of light scattering in nanowire materials for photovoltaic applications ," *Nano Lett.*, vol. 8, pp. 2638–2642, 2008.

[11] V. Zwiller, N. Akopian, M. van Weert, M. van Kouwen, U. Perinetti, L. Kouwenhoven, R. Algra, J. Gomes-Rivas, E. Bakkers, G. Patriarche, L. Lui, J. Harmand, Y. Kobayashi, and J. Motohisa, "Optics with single nanowires," *Comptes Rendus Physica*, vol. 9, pp. 804–815, 2008.

[12] T. Bohnen, G. Yazdj, R. Yakimoya, G. van Dreumel, P. Hageman, E. Vlieg, R. Algra, M. Verheijen, and J. Edgar, "ScAlN Nanowires: a Cathodoluminescence Study," *J. Cryst. Growth*, vol. 311, pp. 3147–3151, 2009.

[13] T. Bohnen, G. van Dreumel, P. Hageman, R. Algra, W. van Enckevort, E.Vlieg, M. Verheijen, and J. Edgar, "Growth of scandium aluminum nitride nanowires on ScN(111) films on 6H-SiC substrates by HVPE," *Physica Status Solidi a*, vol. 12, pp. 1–7, 2009.

[14] S. Diedenhofen, G. Vecchi, R. Algra, A. Lagendijk, A. Hartsuiker, O. Muskens, G. Immink, E. Bakkers, W. Vos, and J. G. Rivas, "Broadband and omnidirectional antireflection coating based on semiconductor nanorods," *Advanced Materials*, vol. 21, pp. 973–978, 2009.

[15] O. Muskens, S.L.Diedenhofen, B. Kaas, R. Algra, E. Bakkers, J. Gomes-Rivas, and A. Lagendijk, "Large Photonic strength of highly tunable resonant nanowire materials," *Nano Lett*, vol. 9, pp. 930–934, 2009.

[16] M. van Weert, N. Akopian, F. Kelkensberg, U. Perinetti, M. van Kouwen, J. Gomez-Rivas, M. Borgström, R. Algra, M. Verheijen, E. A. M. Bakkers, L. Kouwenhoven, and V. Zwiller, "Orientation-Dependent Optical-Polarization Properties of Single Quantum Dots in Nanowires," *Small*, vol. 5, pp. 2134–2138, 2009.

[17] M. van Weert, N. Akopian, U. Perinetti, M. van Kouwen, R. Algra, M. Verheijen, E. Bakkers, L. Kouwenhoven, and V. Zwiller, "Selective Excitation and Detection of Spin States in a Single Nanowire Quantum Dot," *Nano Letters*, vol. 4, pp. 1989–1993, 2009.

[18] M. van Weert, A. Helman, W. van den Einden, R. Algra, M. Verheijen, M. Borgström, G. Immink, J. Kelly, L. Kouwenhoven, and E. Bakkers, "Zinc Incorporation via the Vapor-Liquid-Solid Mechanism into InP Nanowires," *Journal of the American Chemical Society*, vol. 131, pp. 4578–4579, 2009.

[19] V. Favre-Nicolin, F. Mastropietro, J. Eymery, D. Camacho, Y. Niquet, B. Borg, M. Messing, L.-E. Wernersson, R. Algra, E. Bakkers, T. Metzger, R. Harder, and I. Robinson, "Analysis of strain and stacking faults in single nanowires using Bragg coherent diffraction imaging," *New Journal of Physics*, vol. 12, p. 035013, 2010.

[20] M. van Kouwen, A. Hidma, M. Reimer, M. van Weert, R. Algra, E. Bakkers, L. Kouwenhoven, and V. Zwiller, "Single Electron Charging in Optically-Active Nanowire Quantum Dots," *Nano Lett.*, vol. 10, pp. 1817–1822, 2010.

[21] M. van Kouwen, M. van Weert, M. Reimer, N. Akopian, U. Perinetti, R. Algra, E. Bakkers, L. Kouwenhoven, and V. Zwiller, "Single quantum dot nanowire photodetectors," *Applied Physics Lett.*, vol. 97, p. 113108, 2010.

[22] J. Stiegler, A. Huber, S. Diedenhoven, J. Gomes-Rivas, R. Algra, E. Bakkers, and R. Hillenbrand, "Nanoscale free-carrier profiling of individual semiconductor nanowires," *Nano Lett*, vol. 10, pp. 1387–1392, 2010.

[23] A. Pierret, M. Hocevar, S. Diedenhofen, R. Algra, E. Vlieg, E. Timmering, M. Verschuuren, G. Immink, M. Verheijen, and E. Bakkers, "Generic nanoimprint process for fabrication of nanowire arrays," *Nanotechnology*, vol. 21, p. 065305, 2010.

[24] J. van Tilburg, R. Algra, G. Immink, M. Verheijen, E. Bakkers, and L. Kouwenhoven, "Surface passivated InAs/InP core/shell nanowires," *Sem. Sci. and Technology*, 2010.

[25] M. van Weert, M. den Heijer, M. van Kouwen, R. Algra, E. Bakkers, L. Kouwenhoven, and V. Zwiller, "Surround-gated vertical nanowire quantum dots," *Applied Physics Letters*, vol. 96, p. 233112, 2010.

List of symbols and abbreviations

Symbol	Explanation
(hkl)"A"	Terminology for group III terminated facet
(hkl)"B"	Terminology for group V terminated facet
(hkl)	Miller index for a face
<hkl>	Miller index for a set of directions
[hkl]	Miller index for a direction
$\{hkl\}$	Miller index for a set of faces
A	Constant independent of the chemical potential, however including surface energies and twin energies.
a	Geometrical constant
ANA	Software package to calculate structure factors
α	Fraction of the perimeter of the nucleus which is in contact with the vapor
b	Geometrical constant
B_0D	Kinetic constant independent of the chemical potential defining diffusion rates, reaction rates, etc.
β	Droplet contact angle with respect to the droplet-nanowire interface
C	Constant with dimension of energy
CBE	Chemical Beam Epitaxy
$CBED$	Convergent Beam Electron Diffraction
$CMOS$	Complementary Metal-Organic-Semiconductor
D	Nanowire diameter
d	Edge displacement by the evolution of the cross-sectional shape
$DEZn$	Di Ethyl Zinc
Δ	Free energy divided by k_BT or the dependence on the squared solid-liquid surface energy divided by the squared chemical potential

Symbol	Explanation
ΔE	Free energy of a III-V atom pair in a crystal structure
ΔG^*_{XY}	Free energy of formation of an edge nucleus formed
$\delta\Delta G^*$	Difference in free energy of two competing nucleation processes
$\delta\Delta G^*_0$	Difference in free energy of two competing nucleation processes at a hexagonal interface shape
$\Delta\gamma$	difference in solid-liquid step free energy between a ZB and WZ nucleus
$\Delta\mu$	Supersaturation (defined as the chemical potential per unit volume between liquid and solid)
$\delta_{AB}, \delta_{AA}, \delta_{BB}, \delta_{BA}$	Contact angle of the liquid catalyst droplet with respect to the outer nanowire facet
δ_{XY}	Contact angle of the liquid catalyst droplet with respect to the outer nanowire facet
EDX	energy-dispersive X-ray analysis
$ESRF$	European Synchrotron Radiation Facility
$f(\theta)$	Describes the area of the nucleus in contact with the nanowire edge (nucleus-vapor)
$FWHM$	Full Width Half Maximum
ϕ	Interface deformation
ϕ-phase	Stable alloy composition for Au-In
ϕ_1	Interface deformation at which the ratio of {111} and {100} nano-facets is the the ration of 2:1 creating overall
ϕ_2	Interface deformation at which the paired twin occurs
$GroupII$	Elements in the column of Zn, Cd atoms in the periodic table
$GroupIII$	Elements in the column of Ga, In atoms in the periodic table
$GroupIV$	Elements in the column of C, Si atoms in the periodic table
$GroupV$	Elements in the column of P, As atoms in the periodic table
$GroupVI$	Elements in the column of O, S atoms in the periodic table
γ_{AA}	Edge energy
γ_{AB}	Edge energy
γ_{edge}	Edge energy

Symbol	Explanation
γ_{eff}	Effective step energy which depends on the contact angle between the droplet and the external (solid-vapor) facet of the nucleus
γ_{LV}	Liquid-Vapor surface energy
γ_{nN}	Interface energy between nucleus and nanowire
γ_{SL}	Solid-Liquid surface energy
γ_{SV}	Solid-Vapor surface energy
γ_{st}	Step energy
γ_T	Interface energy associated with a twin plane
χ_X	Droplet contact angle with respect to he growth direction
λ_g	Precursor diffusion length through the gas phase
λ_s	Precursor diffusion length over the surface
h	Layer thickness
H	Nanowire height
$HAADF$	High Angle Annular Dark Field (TEM mode)
$HRTEM$	High Resolution Transmission Electron Microscopy
H_0	Nanowire height at hexagonal cross-sectional interface
$ID03$	Beamline at ESRF
K	Dependency on chemical potential and the solid-liquid and liquid-vapor surface energies
$King'sWater$	Wet chemical etchant (HCl : HNO_3 : H_2O, 3:2:3)
k_B	Boltzmann constant
LA	Laser Ablation
LED	Light Emitting Diode
l_0	Cross-sectional edge length of a hexagon
l_A	Cross-sectional edge length of an "A"-terminated facet
l_B	Cross-sectional edge length of an "B"-terminated facet
L_{inv}	Inversion length for changing the cross-sectional shape after the formation of a twin plane
L_p	Length between a twin pair
MBE	Molecular Beam Epitaxy
ML	Monolayer
MMG	Mono Methyl Gallium
$MOVPE$	Metal Organic Vapor Phase Epitaxy
NA	Numerical Aperture
NW	Nanowire

Symbol	Explanation
N_1	Number of monolayers from a hexagonal interface to ϕ_1
N_2	Number of monolayers from a hexagonal interface to ϕ_2
N_c	Critical number of monolayers
N_{inv}	Number of monolayers to complete the inversion length L_{inv}
N_p	Number of monolayers between a twin pair
N_s	Number of monolayer in a superlattice segment
$PDMS$	Poly-Di-Methyl-Siloxane
$Piranha$	(H_2SO_4 : H_2O_2 : H_2O, 5:1:1)
PL	Photoluminescence
$PMMA$	Poly-Methyl-Meth-Acrylat
P_{AA}	Probability of formation of a "A"-nucleus on a "A" facet
P_{AB}	Probability of formation of "A"-nucleus on a "B" facet
P_{Ga}	Partial pressure of the TMGa precursor
P_{XY}	Probability of formation for a type of nucleus
π	pi
R	Growth rate
RF	Radio Frequency heating
RIE	Reactive Ion Etch
ROD	Software package to fit structure factors
$SCIL$	Surface Conformal Imprint Lithography
SEM	Scanning Electron Microscopy
$STEM$	Scanning Transmission Electron Microscopy
$SXRD$	Surface X-Ray Diffraction
T	Temperature
TEM	Transmission Electron Microscopy
$TMG, TMGa$	Tri Methyl Gallium
$TMIn$	Tri Methyl Indium
TSL	Twinning SuperLattice
$Type1, 2, 2', 2", 3, 4$	Different nanowire morphologies
θ	Angle of the side facets with respect to the [111] growth direction
θA	Tilt angle of a "A" terminated facet
θB	Tilt angle of a "B" terminated facet
θy	Tilt angle of the nucleus with respect to the growth direction $\{11\bar{2}\}$ facets
VLS	Vapor-Liquid-Solid

Symbol	Explanation
VPE	Vapor Phase Epitaxy
$VQLS$	Vapor-Quasi-Liquid-Solid
VS	Vapor-Solid
WZ	Wurtzite crystal structure
ZB	Zinc-Blende crystal structure